

# Geophysical investigation of the Hugin Fracture, a soft-sediment seafloor fracture on the Utsira High, North Sea

Implications for subsurface fluid migration

---

Karin Landschulze

Thesis for the degree of Philosophiae Doctor (PhD)  
University of Bergen, Norway  
2019

UNIVERSITY OF BERGEN



**Geophysical investigation of the Hugin  
Fracture, a soft-sediment seafloor  
fracture on the Utsira High, North Sea**  
Implications for subsurface fluid migration

Karin Landschulze



Thesis for the degree of Philosophiae Doctor (PhD)  
at the University of Bergen

Date of defense: 31.05.2019

© Copyright Karin Landschulze

The material in this publication is covered by the provisions of the Copyright Act.

Year: 2019

Title: Geophysical investigation of the Hugin Fracture, a soft-sediment seafloor fracture on the Utsira High, North Sea

Name: Karin Landschulze

Print: Skipnes Kommunikasjon / University of Bergen

„Nur wenige wissen, wie viel man wissen muss, um zu wissen, wie wenig man weiß.“

–

„Only few people understand how much one must understand to understand how little one understands.“

*Werner Karl Heisenberg*

*(†1976)*





---

## Preface to the thesis

This dissertation for the degree of philosophiae doctor (PhD), entitled "Geophysical investigation of the Hugin Fracture, a soft-sediment seafloor fracture on the Utsira High, North Sea" has been submitted to the Department of Earth Science at the University of Bergen. The project was funded by a university grant dedicated to the national centre for environment-friendly research FME SUCCESS (SUbsurfaceCO<sub>2</sub> storage – Critical Elements and Superior Strategy), a centre for environmental-friendly energy research (CEER) (Aker *et al.* 2011). An integral part of this work is based on the discovery of a seafloor fracture in the North Sea during a research cruise funded by the European ECO<sub>2</sub>-project (<http://www.eco2-project.eu>) (Wallmann 2010).



The candidate enrolled in the PhD program at the Department of Earth Science at the University of Bergen, Department of Earth Science, and the work presented in this thesis was carried out at the Centre for Geobiology (CGB), one of 21 Norwegian Centres of Excellence (CoE), between September 2010 and November 2016 including two years of parental leave and one year of teaching obligations.

In 2010, this PhD-project started as a theoretical approach to CO<sub>2</sub>-leakage, with the aim to assess possible fluid flow through different suggested leakage pathways in the overburden using numerical methods. The discovery of a seafloor fracture on the Utsira High in 2011 represented an intriguing opportunity to investigate the relevance of this fracture for subsurface fluid migration, including CO<sub>2</sub>. We decided to change the topic

and objective of the PhD-project, towards qualitative assessment of the seafloor fracture, called Hugin Fracture, and to investigate its possibly ice-load related formation. The redefined PhD-work was conducted in the remaining two years of the original three-year period, focussing on efficiently establishing a good understanding of the fracture and its relevance to fluid migration.

The research was supervised by Professor Rolf Birger Pedersen (University of Bergen, CGB), and co-supervised by Dr. Jan Tveranger (University of Bergen / Uni Research CIPR), Dr. Ivar Aavatsmark (Uni Research CIPR) and Dr. Øystein Pettersen (Uni Research CIPR).

### **Note to the Readers**

The thesis follows an article-based format and is presented in three main parts. First, an introduction addressing the aims of the study, background, data and methods is provided. The main part of the thesis contains the result of the research presented as scientific papers that are either submitted to or planned submitted to peer-reviewed scientific journals. The last part is a synthesis of the study providing a summary and a brief discussion of the main results, implications, conclusions and perspectives for further work. An appendix includes details on data interpretation.

---

## Acknowledgements

Firstly, I would like to thank my main supervisor, Rolf Birger Pedersen, for your support and guidance during these years. Thanks for initiating the project and entrusting me with tasks that seemed just out of reach for me, like your oral presentation at the AGU Fall meeting in 2013 that I gave in your place. Your enthusiasm about my language abilities at our first meeting in 2010 has since been shared by many other people. I thank Jan Tveranger for helping me navigate in the world of geology and for countless rigorous feedback on manuscript drafts. You helped me see the wondrous surprises of fractures, faults and river systems. Thanks to Øystein Pettersen for your valuable experience in reservoir modelling, you helped me to avoid the most serious simulation pitfalls. I also wish to thank Ivar Aavatsmark for your insight in thermodynamics. Your mathematical insight in governing equations for subsurface fluid flow was inspiring, even though my research went in another direction than first imagined.

Thanks to all the wonderful people I met during my time at the CGB. Some of them deserve special mentioning:

Andreas who just happened to knock on my door one day and turned out to be a good guy to grab a coffee with. I will never forget you as my professional driver during our field course in Finnmark: Thank you, and your wonderful family, for your friendship ever since! Many thanks to Kristin who not only shared my office but a lot of my joys and temporary frustrations. My former colleagues Tamara and Laila I want to thank for their work enthusiasm and many encouraging social happenings for the colleagues. CGB relay at Bergen City Marathon in 2014! Thanks to Ingeborg, Irene, Elinor and Anita for lunch discussions and coffee breaks. Leif-Erik challenged me to teach geology, in Norwegian (!); thank you for your inspiring leadership of our assistant teacher group in GEOL101/102. Thanks to Johnny Hesthammer and Henk Keers for teaching me a great deal about guiding students on their way towards understanding seismic interpretation and numerical modelling of geophysical problems. Through Henk I became friends with Andrea: thank you for your friendship during the past 4

years and good luck for your own work. Many thanks to my office mate William for discussing both science-related and teaching-related topics: You helped me realize just how much teaching means to me.

Thanks to all my friends outside university who never were quite sure what I was doing in my working hours and what a “disputas” really is about, but who inspired and helped me to cultivate an understandable language for my research. To my colleagues at the NLA University College over the past one and a half years I want to express my gratitude for the warm welcome, enlightening insights and inspiring discussions about teacher education and children’s learning. You helped me keep up my motivation during the final efforts of finishing this thesis.

Finally, I am very much indebted to my marvellous family, for their sublime patience and steady support during my studies. My beloved husband Marcus and our amazing children Lucius, Cornelius and Aurelia: You cheered me up, gave me strength and endless love. Whatever seemingly insurmountable obstacle or challenge I encountered during the past eight years – you enabled me to overcome it. Thank you!

Karin Landschulze

July 5<sup>th</sup>, 2018

---

## Abstract

The 2011 discovery of the Hugin Fracture, a 3.5 km long seafloor fracture on the Utsira High, shows that large-scale, unexpected features can still be found in ostensibly well-mapped, highly industrialized offshore areas like the Norwegian North Sea. Situated on an up to 1000 m thick glaciogenic overburden, the fracture proves seabed fluid flow and a seemingly brittle behaviour of the unconsolidated Holocene-Quaternary sediments. The present thesis includes geophysical investigation of the fracture and underlying Pleistocene sediments down to the Utsira Formation and a poroelastoplastic deterministic simulation of the fracture formation.

Based on high-resolution synthetic aperture sonar data, sub-bottom profiler and 3D seismic data, the seafloor track of the fracture is connected to subvertical fractures connected to the margin of a sand body identified as an alluvial fan at 40 m below the seafloor. Interpretation of seismic attributes and well log data suggests differential compaction of the stratigraphy. Given the location and age of the sediments, burial compaction is likely to have been enhanced by glacial loading. The Hugin Fracture is proposed to represent a compaction fracture formed after deposition of fan sediments some 20-29 ka ago.

Older Pleistocene sediments below the Hugin Fracture may conceivably host similar fractures. Local absence of otherwise abundant bright spots in the underlying Pliocene succession could indicate leak-off of gas from this stratigraphic level to the seafloor through a network of channels and fractures in the overburden. A minor fault in the top 100 m of the Utsira sands was identified some 700 m below the Hugin Fracture, the 3D seismic data indicate that it has not propagated into the overlying stratigraphy. The presented observations suggest that the seal properties of the Pleistocene overburden of the Utsira Fm. are compromised at the Hugin Fracture location.

A 2D geomechanical model has been constructed from an interpreted 3D seismic section over the Hugin Fracture to test the fracture formation hypothesis of ice-load induced differential compaction. Layer properties were chosen from literature values for sand and stiff clay and a six-layered background model with nine channels/tunnel

valleys at different depths was constructed. The poroelastoplastic simulation uses a ramp function representing an up to 80 m thick ice sheet with a growth and decay rate of 0.8 MPa/ka in a single loading/unloading cycle.

Simulation results show isotropic stress and strain distribution in the horizontally layered, isotropic part of the model totally covered by the ice. In the central, channelized part of the model a composite stress and strain pattern develops with sub-vertical focus areas tangential to channel edges. The low stress, strain and deformation values under total load increase drastically soon after the load starts to decrease, resulting in development of high plastic strain accumulations in the focussed zones. Surface deformation such as formation of compaction ridges above stiff clay filled channels and depressions associated with plastic deformation is observed. A fracture and associated surface deformation develop above the shallowest sand-filled channel, resembling the observed geometry at the Hugin Fracture.

The simulation supports the formation hypothesis for the Hugin Fracture as a compaction fracture. The resulting stress-strain pattern suggests that thin ice sheets may induce differential compaction and plastic strain accumulation tangential to channel edges to a depth of several hundred meters. Repeated glaciations of the study area should have produced distinct stress-strain patterns in the Quaternary sediments and below according to the ice load, its geometry and the stratigraphic heterogeneity. We consider it likely that similar compaction fractures like the Hugin Fracture may be encountered in a wider area, and at larger depths. Other areas with similar glaciation history should therefore hold similar fractures.

The results of this study should be of interest for subsea fluid migration and overburden sealing quality for e.g. geological storage of carbon dioxide that has been suggested for a larger part of the Utsira Formation.

---

## List of publications and authorship statement

### **Paper 1: Discovery of seabed fluid flow along a 3 km long fracture in the Central North Sea**

*Manuscript draft.*

Pedersen R.B., Landschulze K., Blomberg, A., Gracias, N., Baumberger, T., Økland, I., Mørkved, P.T., Reigstad, L., Denny, A., Thorseth, I.H.

### **Paper 2: Seismic investigation of the Hugin Fracture, a seafloor fracture on the Utsira High, Central North Sea**

*Submitted to Geophysical Prospecting.*

Landschulze, K., Tveranger, J., Pedersen, R.B

### **Paper 3: Fracture formation due to differential compaction under glacial load: a poro-elastoplastic simulation of the Hugin Fracture**

*Submitted to Near Surface Geophysics.*

Landschulze, K., Landschulze, M.



**Table 1:** Authorship contributions

<i>Task</i>	<i>Paper 1</i>	<i>Paper 2</i>	<i>Paper 3</i>
<i>Acquisition of field data</i>	All authors, except Landschulze, K.	Pedersen	-
<i>Data acquisition (2D and 3D seismic, well logs, etc.)</i>	Landschulze, K. and Pedersen	Landschulze, K.	Landschulze, K.
<i>Seismic Data processing</i>	Landschulze, K. and Blomberg	Landschulze, K.	Landschulze, K.
<i>HiSAS data processing</i>	Blomberg	-	-
<i>Seismic data interpretation</i>	Landschulze, K.	Landschulze, K.	Landschulze, K.
<i>Well log interpr.</i>	-	Landschulze, K.	Landschulze, K.
<i>Simulation data processing</i>	-	-	Landschulze, M.
<i>Model Design and parametrization</i>	-	-	Landschulze, K.
<i>Simulation set-up and robustness tests</i>	-	-	All authors
<i>Text</i>	Each author in their respective field, lead author synthesis	Landschulze, K.	Landschulze, K.
<i>Figures</i>	Each author of their respective data	Landschulze, K.	All authors
<i>Manuscript discussion and review</i>	All authors, K. Landschulze did final reviews on the complete draft	All authors	All authors

# Contents

<b>Preface to the thesis</b> .....	<b>iii</b>
<b>Acknowledgements</b> .....	<b>v</b>
<b>Abstract</b> .....	<b>vii</b>
<b>List of publications and authorship statement</b> .....	<b>ix</b>
<b>Contents</b> .....	<b>11</b>
<b>1. Introduction</b> .....	<b>13</b>
1.1 <i>Evolution of the North Sea sediments and influence of glacial tectonics</i> .....	13
1.2 <i>Study area and initial discovery</i> .....	17
1.3 <i>Research questions</i> .....	21
1.4 <i>Data and methods</i> .....	23
1.5 <i>Contributions at scientific meetings</i> .....	31
1.6 <i>Contributions to other publications</i> .....	33
<b>2. Manuscript compilation</b> .....	<b>35</b>
<b>Paper I:</b> .....	<b>37</b>
<b>Discovery of seabed fluid flow along a 3 km long fracture in the Central North Sea</b> .....	<b>37</b>
<b>Paper II:</b> .....	<b>67</b>
<b>Seismic Investigation of the Hugin Fracture, a seafloor fracture on the Utsira High, Central North Sea</b> .....	<b>67</b>
<b>Paper III:</b> .....	<b>125</b>
<b>Fracture Formation due to Differential Compaction under Glacial Load: a Poroelastoplastic Simulation of the Hugin Fracture</b> .....	<b>125</b>
<b>3. Synthesis</b> .....	<b>177</b>
3.1 <i>Synthesis of main findings and key implications</i> .....	177
3.2 <i>Concluding remarks</i> .....	187
3.3 <i>Future perspectives</i> .....	187
<b>4. References cited in Introduction and Synthesis</b> .....	<b>189</b>
<b>5. Appendix</b> .....	<b>197</b>
5.1 <i>Seismic interpretation workflow and results</i> .....	<i>I</i>

---

5.2 <i>Geomechanical model</i> .....	<i>XIV</i>
<b>Errata</b> .....	<b>1</b>

# 1. Introduction

## 1.1 Evolution of the North Sea sediments and influence of glacial tectonics

The North Sea basin was formed during Jurassic crustal extension associated with the opening of the Viking Graben to the east of the Utsira High; the latter formed one of several intra-basin highs (Eidvin, Riis and Rasmussen 2014). During the Plio-Pleistocene the North Sea basin subsided and was filled in by up to 1000 m of sediments derived from the British Isles and the rising Norwegian mainland bordering the basin (Ottesen *et al.*, 2014 and references therein).

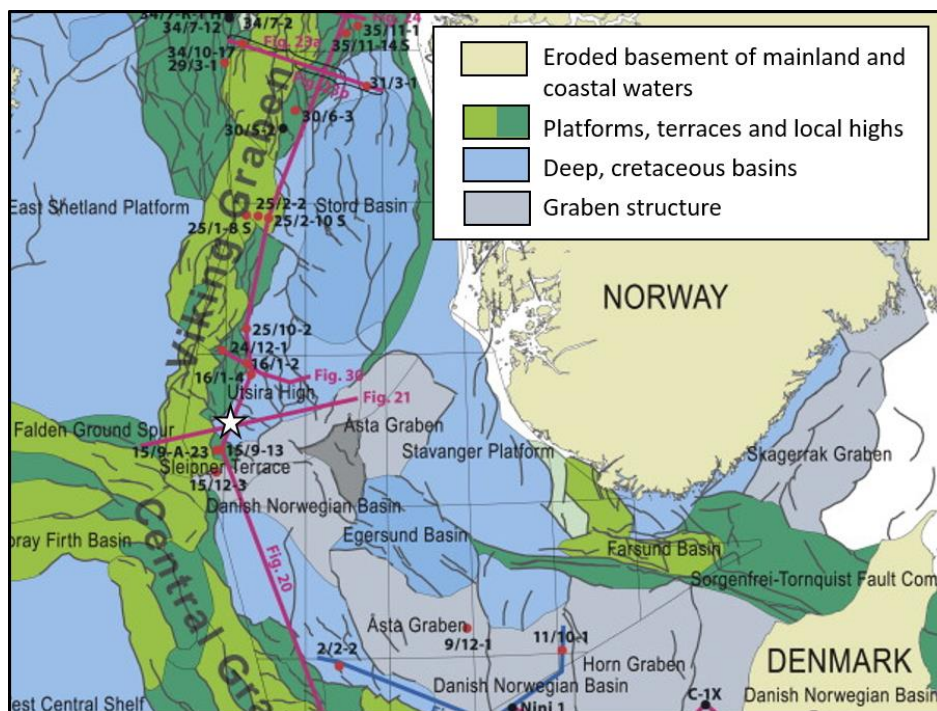


Figure 1: Structural map of North Sea Basin (changed from figure 15 from Eidvin *et al.* 2014, figure references refer to figures in their work). White star indicates location of the Hugin Fracture study area.

In general, the uppermost 1000 m of sediment in the North Sea are considered to consist of unconsolidated to soft sediments as they have not been buried deep enough to experience considerable consolidation or to be lithified (Bjørlykke and Hoeg 1997). The strongest compaction force besides gravitation originates from glaciers or ice sheets present onshore or periodically covering the study area (Grollmund and Zoback 2003, Bjørlykke 2006, Graham *et al.* 2011, Reinardy *et al.* 2017).

During the Pleistocene, the North Sea experienced several glaciation events with varying ice sheet extents and geometries which in sum have produced a very complex geologic record (e.g. Graham *et al.* 2011, Stewart and Lonergan 2011). Relative sea-level falls during glaciations exposed large areas of the seafloor to fluvial and glaci-fluvial erosion, reworking and deposition (Sejrup, Aarseth and Haflidason 1991). These processes are evidenced by the presence of sub-glacially formed tunnel valleys and fluvial incisions filled with younger sediments in the Nordland Group (Huuse and Lykke-Andersen 2000, Kristensen *et al.* 2008). The number and extent of glaciations in the North Sea Basin is a current field of investigation (e.g. Sejrup, Clark and Hjelstuen 2016, Bradwell *et al.* 2008, Graham *et al.* 2011). The interpretation of cross-cutting buried tunnel valleys as either originating from different glaciation events or as a result of changing ice sheet geometry during a single glaciation is still debated (Reinardy *et al.* 2017, Stewart and Lonergan 2011, Stewart, Lonergan and Hampson 2012, Kristensen and Huuse 2012, Praeg 2003). Buried channels and subglacial tunnel valleys have also been documented in the UK sector (Lonergan, Maidment and Collier 2006, Stewart *et al.* 2012, Stewart and Lonergan 2011), and in the Southern parts of the North Sea (Kristensen *et al.* 2007) close to the Netherlands and Denmark (Kehew, Piotrowski and Jørgensen 2012).

Geotechnical investigations to find optimum locations for offshore platform foundations have frequently found buried channels of Mid to Late Pleistocene age and extensive heterogeneity attributed to glacial reworking of the sediment (e.g. Williams and Aurora 1982). Subjected to glacial load, the porosity in muddy sediments decreases considerably and the sediment turns from ductile muddy sediments to more brittle shale with implications for strain behaviour (Dehandschutter *et al.* 2005). In contrast,

---

dominantly sandy sediments hardly decrease in porosity and deform rather elastically under load (Bachrach 2011). Geotechnical properties of the top ~500 m North Sea sediments will lie somewhere in-between the values for soils and rocks, from several authors termed soft rocks (e.g. Aber 1982). The classification of soft rocks is still subject of debate (Kanji 2014).

In the North Sea, the Nordland Group (Gp.) comprises unconsolidated Pleistocene sediments, dominated by marine claystones, from seafloor downwards. In the lower part of the Nordland Gp. at 550-1100 m below main sea level, the 50-300 m thick sandy Utsira Formation (Fm.), occurs in the lower part of the group in the Viking Graben area (Gregersen and Johannessen 2007, Hermanrud *et al.* 2009). Since 1996, the formation has been target for injection and storage of supercritical CO<sub>2</sub>, separated from produced gas at the nearby Sleipner field. The industrial pilot project is monitored with various methods to ensure that the injected CO<sub>2</sub> is confined inside the Utsira Fm (e.g. Arts *et al.* 2008). Experience from this and other pilot projects has led to the development of several best practises for CO<sub>2</sub> storage in saline aquifers (e.g. Chadwick, Arts and Bernstone 2008, Baumberger *et al.* 2014).

Expanding on this successful project and the favourable reservoir rock properties, it has been proposed to utilize the full extent of the Utsira Formation sands, covering an area of approx. 24000 km<sup>2</sup>, for CO<sub>2</sub> storage (Zep Zero emissions platform 2013B, SCCS and Scottish Enterprise 2012). However, due to the shallow burial depth of the Utsira Formation, seal integrity is a concern, especially in light of the multiple glaciation/deglaciation events of the Quaternary period mentioned above (Nicoll 2012). Unlike hydrocarbon reservoirs, that have proven locally good long-term sealing quality, other geological formations, e.g. saline aquifers, may prove to be compromised at some locations. Gas escape through the seafloor is a known phenomenon in the North Sea (Hovland 1981, Hovland 2002, Hovland *et al.* 2010). Therefore, a better understanding of the processes that may have influenced sediment properties and overburden sealing quality is vital to determine storage safety.



## 1.2 Study area and initial discovery

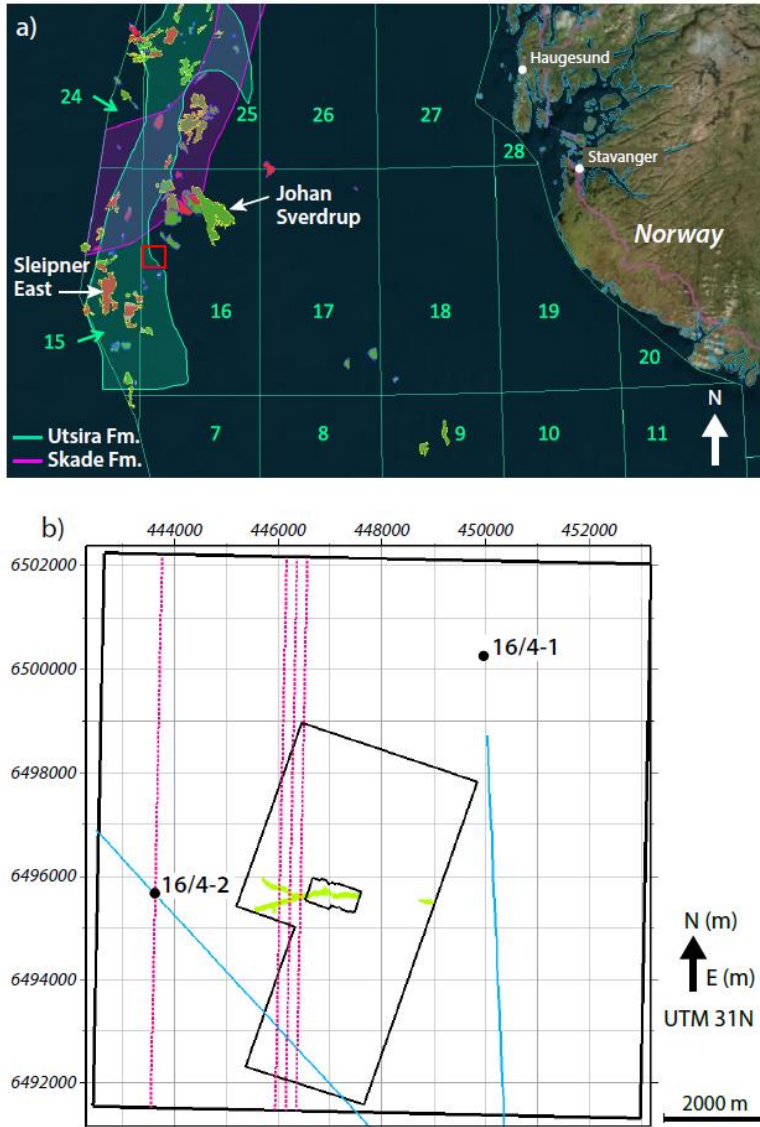


Figure 2: a) Study area with outlines from the areas of the Utsira Fm. and Skade Fm. with favourable properties for CO<sub>2</sub>-storage (NPD CO<sub>2</sub>-atlas). b) seismic datasets, outlines of HISAS data and wells used in this study. Blue lines indicate 2D seismic lines.



The study area is located on the western flank of the Utsira High in the Norwegian Sector of the central North Sea basin (Figure 2a). It is a prolific oil and gas province, with hydrocarbons found in Jurassic to Palaeocene age reservoirs at depths of more than 1900 m. Petroleum exploration and production activity has generated a substantial number of drill cores, a well-established chrono-stratigraphy and a wealth of seismic interpretations focussing on the North Sea hydrocarbon systems (e.g. Bjørlykke *et al.*, 1989; Horsrud *et al.*, 1998). For shallower depths, an extensive body of work exists for the British Sector of the central North Sea (e.g. Lonergan *et al.*, 2006; Stewart *et al.*, 2012), as well as for the Danish and the Dutch sectors of the southern North Sea (Vialle and Vanorio 2011).

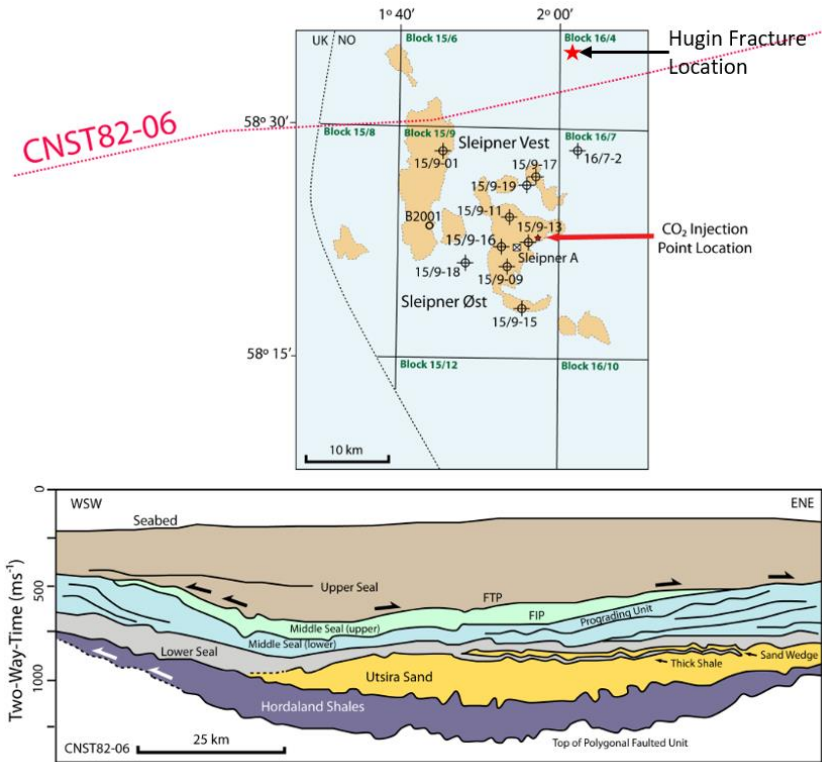
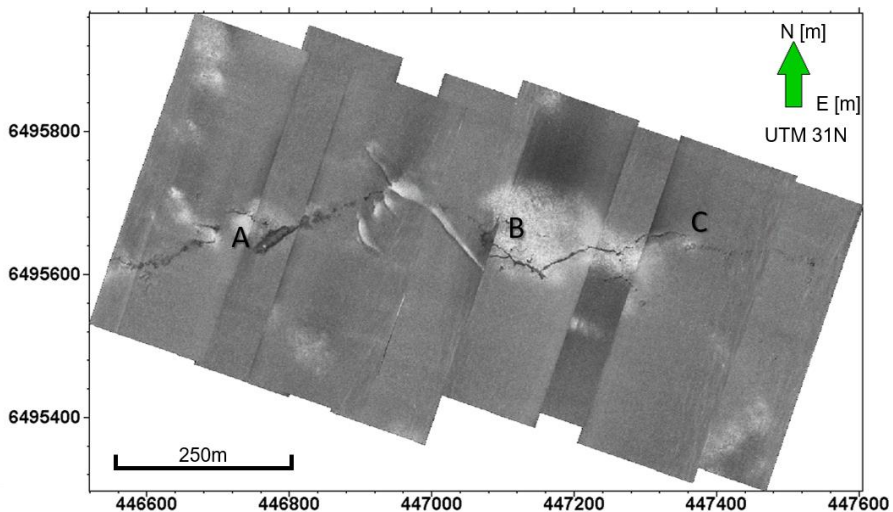


Figure 3: Sediment sequence with seismic unit layers, adapted from Nicoll (2012).

In the Norwegian Sector, a regional study of the Pleistocene succession overlying the Utsira Fm. was recently carried out by Ottesen *et al.* (2014). It covers the Norwegian

Sea and the Norwegian North Sea as well as parts of the British North Sea. In addition, there are several studies of the Utsira Fm. and its overburden (Chadwick and Holloway 2000, Kennett 2008, Gregersen and Johannessen 2007, Nicoll 2012, Karstens and Berndt 2015).

In 2011, seafloor investigations of an area on the Utsira High, in the North Sea, were carried out using the R/V GO Sars (leg no. 367, 2011-108) as part of the ECO<sub>2</sub>-project. One objective of this cruise was to test several high-resolution seafloor mapping tools for locating and mapping fluid seepage features on the seafloor that could be used to detect early signs of leakage from CO<sub>2</sub>-storage projects. During this initial cruise, the high-resolution synthetic aperture sonar (HISAS) mounted on an automated underwater vehicle (AUV) revealed an approximately 3.5 km long and 1-10 m wide sediment-filled fracture approximately 25 km northeast to the Sleipner platform (Figure 2b).



*Figure 4: Seafloor mosaic of the central part of the Hugin Fracture. Light shades indicate high backscatter from harder sediments and dark shades indicate less backscatter energy from softer sediments. The letters indicate locations for details in Figure 7: Details along the seafloor track of the Hugin Fracture, locations indicated in Figure 4. Figure 7 of the synthesis part.*

Active fluid discharge through the seafloor was confirmed by visual inspection through remotely operated vehicle (ROV) that revealed bacterial mats along the fracture on an otherwise barren, sandy seafloor (Pedersen *et al.* 2013). The location reference to the Sleipner platform reflects the perspective view from aboard the research vessel and does not indicate any connection between activities at the Sleipner fields and the seafloor fracture.

---

## 1.3 Research questions

The Hugin Fracture is the first seafloor fracture of its kind to be discovered in the poorly consolidated sediments of the central North Sea. Initial observations showed active fluid flow, that has later been confirmed by others (Pedersen *et al.* 2013, Häckel *et al.* 2013, Lichtschlag *et al.* 2018). Paper I presents the multidisciplinary results from the initial investigation of the seafloor fracture and gives an overview of the seafloor characteristics of the fracture. To characterize and understand the origin of the Hugin Fracture, the objectives of this thesis are to:

1. Establish a geological model of the Hugin Fracture and associated subsurface structures based on geophysical methods.

Pursuing the above-mentioned objective 1 includes answering the following questions:

- How deep is the Hugin Fracture?
- How is the fracture connected to other structures at depth?
- How was the fracture formed?
- Is there a network of structures that could act as fluid flow paths?

Paper II is dedicated to answer these questions and presents a geological model according to objective 1. We propose that the Hugin Fracture is a compaction fracture. Compaction fractures have been reported by e.g. Cosgrove and Hillier (1999), Dehandschutter *et al.* (2005) and Xu *et al.* (2015). Ice-load controlled tectonics and rejuvenation of a sub-salt fault in conjunction to a buried tunnel valley has been reported from the southwestern Baltic Sea (Al Hseinat and Hübscher 2014). In the study area for the present work, Zechstein salt layers are buried at larger depths and play a minor role in shallow tectonics. However, differential subsidence due to changing ice-load is likely to have been present at several times during the Pleistocene (Reinardy *et al.* 2017). In paper II, we propose that the Hugin Fracture is caused by ice-load induced differential stress on sub-horizontally layered sediments, with buried channels with fills that differ from the surrounding sediments. To strengthen or discard this hypothesis the second objective of this project aims to:

2. Test the hypothesis that the Hugin Fracture formed because of ice-load deformation by means of numerical simulation.

Pursuing objective 2 includes answering the following questions:

- Could ice load-induced deformation lead to communication between channels?
- Does fracturing more likely happen during loading or unloading?
- How little ice is needed to induce high strains in the model?

In paper III we present a deterministic, poro-elastoplastic simulation of a section through the Hugin Fracture and present answers to the questions above. The simulation results support the hypothesis and are robust over a range of parameter values.

To cope with strict regulations for pollution control applying to the hydrocarbon production activity mentioned in section 1.2, North Sea sediments are used for e.g. wastewater or CO<sub>2</sub> injection (e.g. Torp and Gale 2004, Barrio *et al.* 2015). As opposed to wastewater, liquified CO<sub>2</sub> has a positive buoyancy that will lead to upwards migration if fluid pathways are present (Celia *et al.* 2005, Caramanna, Fietzek and Maroto-Valer 2011). The well monitored Sleipner CO<sub>2</sub> project has been used to argue for large-scale injection of CO<sub>2</sub> in the sands of the Utsira Formation (Fm.) as a means of alleviating anthropogenic climate gas discharge to the atmosphere (Arts, Brevik and Eiken 2001, Chadwick *et al.* 2006, Chadwick *et al.* 2009, Alnes *et al.* 2011, Zep Zero emissions platform 2013A, Barrio *et al.* 2015). Although the Hugin Fracture area is located about 10 km northeast to the CO<sub>2</sub>-plume of 2009, the plume will spread with continued injection, and also some time after injection cut-off (Cavanagh 2013). Therefore, a minor objective of this study aims at:

3. Investigation of the sealing quality above the Utsira Formation at the Hugin Fracture location.

To this end we looked for faults or other fluid flow indications in the overburden above the top of the Utsira Formation at approximately 800 m depth. We present a minor fault in the top Utsira Fm. in paper II.

---

## 1.4 Data and methods

The Hugin Fracture is situated on the Utsira High in block 16 on the Norwegian Continental Shelf (Figure 3) and is the first soft sediment fracture discovered in the North Sea. It was discovered using the HISAS system mounted on an AUV named “Hugin” (Pedersen *et al.* 2013, paper I). To characterize the fracture seismically and to investigate the possible cause for its formation the following original datasets were acquired by a team of scientists and technicians from University of Bergen using the R/V G.O.Sars (leg 367, 2011-108 and 691, 2012-108): seafloor mosaics of backscatter HISAS data with the AUV Hugin and parametric sub-bottom profiler (SBP) data with the ship-mounted TOPAS system (Figure 5a).

Additional datasets were acquired from Norwegian Petroleum Directorate (NPD) and Lundin Norway AS, to enable linking of the seafloor fracture to geological structures at depth; namely conventional 3D seismic datasets, 2D seismic lines from a site survey for well bore 16/4-7 and gamma-ray and resistivity well logs from well 16/4-1 and 16/4-2 (Figure 2b for well locations). The following sections give details on the different datasets and respective methods.

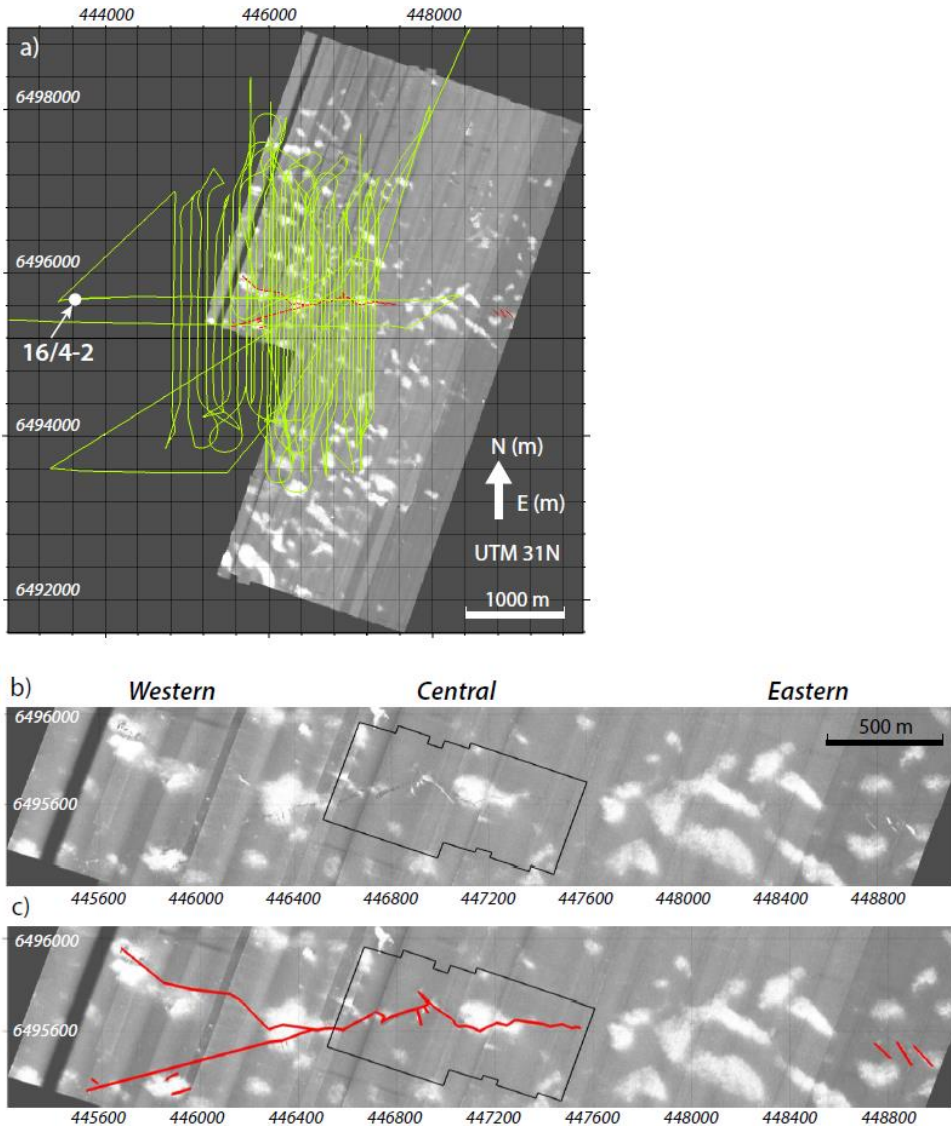


Figure 5: a) HISAS mosaic of the Hugin Fracture Area with SBP lines. b) Detail of the mosaic in a) along the Hugin Fracture. c) same as b) with overlain linear track of the Hugin Fracture. Black polygon indicates outline of mosaic in Figure 4

### 1.4.1 HISAS data

The HISAS system allows efficient high-resolution (up to 3 cm x 3 cm) mapping of the seafloor, producing detailed backscatter images (Hansen *et al.* 2011). The large number of data points result in large data files, even for seafloor areas that are small compared to 3D seismic coverage. The HISAS system can be used to map seafloor properties that effect backscatter energy, such as differences in sediment consistency. It has also been described as a method to detect and monitor bubbly seepage from the seafloor (Blomberg *et al.* 2017). The HISAS dataset was crucial in the discovery of the Hugin Fracture. Two seafloor mosaics were employed in this thesis, both are centred above the Hugin Fracture (Figure 2b and Figure 5). The larger seafloor mosaic has a resolution of 33 cm x 33 cm and covers an area of approximately 30 km<sup>2</sup>. The smaller seafloor mosaic has a resolution of 10 cm x 10 cm and covers an area of approximately 0.42 km<sup>2</sup>.

Geophysical and geological interpretation of the HISAS data was carried out based on the principle of attenuation of acoustic energy and standard description of geologic features. High-backscatter areas indicate “harder” material (like the shell hashes appearing as white clouds in Figure 5) or different angle to antenna (slight elevations as for the en-échelon fractures in the Eastern part, Figure 5b). Lower backscatter reflects “softer” sediment that may indicate different sediment properties or fluid saturation (dark patches and line elements along the fracture in Figure 5).

### 1.4.2 Sub-bottom profiler data

A dense, parametric SBP dataset was acquired over the extent of the Hugin Fracture (see Figure 5). Profile intervals vary between 50 m and 100 m. The source signal of the TOPAS system is generated by two high-frequency beams interacting in the water column producing a high-bandwidth – narrow-beam signal. A ship-mounted TOPAS PS 018 system with a 2-6 kHz (linearly frequency modulated) chirp source signal and ping intervals of 400-1000 ms was employed. The SBP had a penetration depth of up to 44 ms two-way-time (TWT) in the sandy sediments encountered in the study area, corresponding to 35 m for an assumed sediment velocity of 1600 m/s (Hamilton,



Bachman and Sandy 1982). If the actual sediment velocity was 1800 m/s, the penetration depth corresponds to 40 m.

Interpretation of SBP data included verifying fractures at HISAS locations and detecting seismic units in the top 40 m of the sediments. The vertical trace of the fracture was linked to the fracture on the HISAS seafloor mosaics (paper II). Interpretation of 3D seismic data followed standard procedures, including manual and automatic tracking of major horizons on inline and crossline sections. Different seismic attribute volumes were computed to aid in discriminating of reflections, subtle fractures and stratigraphic or lithologic changes (Chopra and K. Marfurt 2007).

Ideally, the near seafloor high-resolution data from the HISAS and SBP should be correlated to near surface 2D seismic lines with a resolution in-between the SBP system and conventional 3D seismic data. Due to technical issues, no 2D seismic lines of sufficient quality could be acquired in 2012. Nevertheless, the HISAS seafloor mosaic and the SBP data were correlated with the 3D dataset to investigate deeper structures that may be related to the Hugin Fracture. High-resolution 2D seismic lines near the Hugin Fracture (courtesy Lundin Norway AS) were used to assist in overall understanding of the geology (Figure 2b).

### **1.4.3 Conventional seismic data**

#### ***3D seismic dataset***

A high-quality, near-trace dataset comprising four distinct 3D seismic cubes with a merged areal coverage of 3000 km<sup>2</sup> was employed in this thesis. The individual seismic cubes had been acquired for hydrocarbon exploration purposes at different times during the period from 1995 to 2008 and had been reprocessed and merged into a composite near-trace dataset in 2009 on behalf of Lundin Norway AS. The Hugin Fracture lies in the central western part of the full dataset and, hence, interpretation was focused on a 118 km<sup>2</sup> rectangular subset of this dataset centred around the fracture (Figure 2). The 3D dataset has a lateral resolution of up to 25 m (bin size) and a dominant frequency from around 18 Hz at the seafloor to about 40 Hz in larger depths, yielding vertical

resolutions ( $\lambda/4$ ) of 26 m and 12 m, respectively (Cartwright and Huuse 2005 and references herein).

Even though the conventional 3D seismic dataset was reprocessed to a near-trace dataset, the Hugin Fracture and related structures represent extremely shallow features in the 3D seismic cube making them challenging to distinguish in the low resolution, composite signal near the seafloor reflection. To enhance continuity of seismic reflections and to dampen acquisition noise, a 980 km<sup>2</sup> subset of the original dataset was submitted to a noise cancellation workflow in the proprietary software GeoTeric 2013.1. Further, frequency decomposition of the 3D seismic dataset produced colour-blended data volumes with the aim of identifying sediment structures and lateral shifts in sediment composition. Over the past decade, frequency decomposition has emerged as a technique to highlight subtle details in 3D seismic data volumes (e.g. Girolodi and Alegria 2005). The process and the workflow applied to the data is further described in the Appendix.

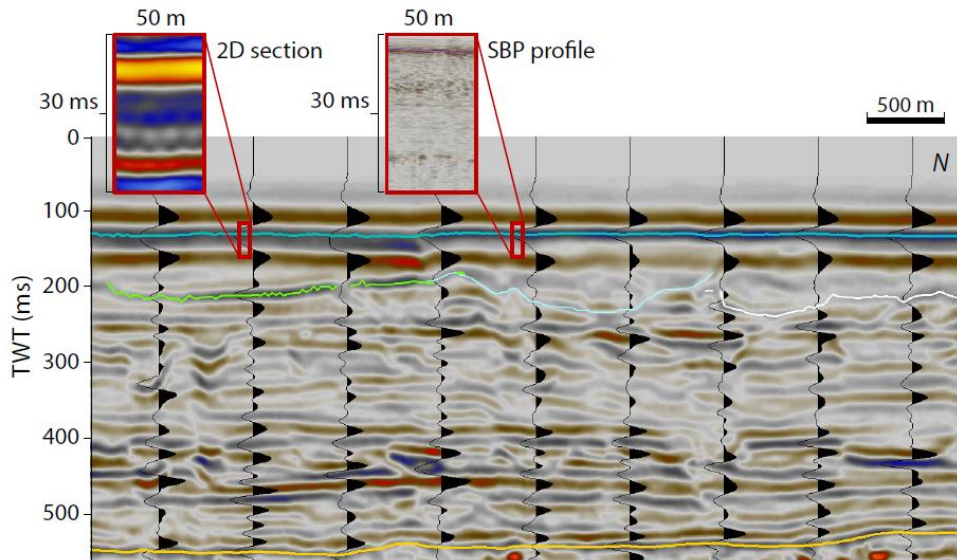


*Figure 6: Comparison of data resolution of the different seismic datasets. Large section is from 3D data, example details from 2D seismic and SBP data are shown for the main and lower sidelobe seafloor signal in the 3D seismic data.*

Interpretation of the conditioned 3D seismic data followed standard procedures, including manual and automatic tracking of major horizons on inline and crossline sections. Different seismic attribute volumes were computed to aid in discriminating of reflections, subtle fractures and stratigraphic or lithologic changes (Chopra and K. J. Marfurt 2007, Brown 2008).

In the present thesis, the target structures for the seismic interpretation occur in the first 40-100 m below seafloor, a depth that is not well imaged by conventional 3D seismic data (see Figure 6). Because the seafloor reflection represents a major upwards contrast in acoustic impedance, the seismic signal influenced by the seafloor reflection energy has a much lower resolution near the seafloor than at larger depths. In the current dataset, the zero-phased seafloor reflection is 80 ms wide, including precursor (see Figure 6). Any interpretation of near-seafloor structures will be uncertain unless it can be correlated with independent data. As the only other available data at the Hugin Fracture are limited to the seafloor (HISAS mosaic) and the top 40 m (SBP data), there is a resolution gap in the applied datasets.

### ***2D seismic dataset***

High resolution 2D seismic lines from a drilling site survey for well 16/4-7 were made available from the national petroleum database (courtesy of Lundin Norway AS), and two of the 2D sections covered parts of the study area (see Figure 2b for location). One section represents a well tie from 16/4-1 towards the drilling site in the southeast. The other section starts close to well 16/4-2 and continues southwards. The data were already processed, the processing protocols were not accessible.

#### **1.4.4 Well data**

Well logs and well reports for well 16/4-1 and 16/4-2 were available from NPD ([www.npd.no](http://www.npd.no)). Both wells penetrate the same structure, identified as fluvial fan in the 3D seismic data. For both wells gamma-ray values and resistivity values were logged from the seafloor. These log types complement each other and were used to interpret sediment type and the nature of fluid fill as described in Rider and Kennedy (2013).

---

### 1.4.5 Poroelastoplastic simulation

Numerical simulation of rock physics and fluid-rock interaction has become easier to facilitate thanks increasing computing capacity of modern computers. In addition, algorithms for elastoplastic and poroelastic models have been improved and, recently, poroelastoplasticity has become more widely accessible (Nikolinakou *et al.* 2012). Hence, modern geomechanical models can more accurately represent the field situation depending on the amount and quality of rock or soil property measurements available to constrain the model. Even though distinct geotechnical measurements were not available in the present work, the discovered structures can, nonetheless, be better understood through simulations by applying literature properties.

Based on the interpretation of the geophysical data, a poroelastoplastic 2D model from a selected section of the 3D seismic dataset was designed in COMSOL Multiphysics (COMSOL Inc. 2016, Li *et al.* 2009). Time-transient simulations applied a maximum top load of 8 MPa as a single loading/unloading cycle, using a linear growth rate of 0.8 MPa / 10 ka. Prior to building the model for the Hugin Fracture case, we tested the simulation tool by recreating the poroelastoplastic 2D model of the stress field adjacent to a spherical salt body as presented by Nikolinakou *et al.* (2012). After successful recreation of their model, a simplified 2D model of the Hugin Fracture area was constructed and poroelastoplastic simulations were carried out. Paper III comprises a description of the simulations and an interpretation of the simulation results.



---

## 1.5 Contributions at scientific meetings

### 2014

*Landschulze, Karin. (Oral presentation)*

Channel and tunnel valley systems in the top 500m of sediment rock at the Hugin Fracture area. *ECO<sub>2</sub> Young Scientist Event 2014, Lipari, Sicily*

*Landschulze, Karin; Pedersen, Rolf B.; Blomberg, Ann Elisabeth Albright; Baumberger, Tamara; Økland, Ingeborg Elisabet; Reigstad, Laila Johanne; Gracias, Nuno; Mørkved, Pål Tore; Thorseth, Ingunn Hindenes; Cevatoglu, Melis; James, Rachael; Häckel, Matthias. (Oral presentation)*

The Hugin Fracture – an overview. *ECO<sub>2</sub> Annual Meeting 2014*

*Landschulze, Karin. (Oral presentation)*

Overburden Integrity: Northern part of the Utsira Formation. *SUCCESS seminar 2014*

*Landschulze, Karin; Tveranger, Jan; Pedersen, Rolf B. (Extended abstract & oral presentation)*

Characterization of Shallow Seal Complexes for CO<sub>2</sub> Storage Sites – Example from the Greater Sleipner Area. *IN: 1st Applied Shallow Marine Geophysics Conference, Part of Near Surface Geoscience 2014. EAGE. DOI: 10.3997/2214-4609.20142142*

*Landschulze, K., J. Tveranger, R. B. Pedersen (Oral presentation, **1<sup>st</sup> prize**)*

Characterization of Shallow Seal Complexes for CO<sub>2</sub> Storage Sites – Example from the Greater Sleipner Area, *CLIMIT PhD seminar 2014*

### 2013

*Landschulze, Karin. (Oral presentation)*

Investigation of possible CO<sub>2</sub> migration pathways and mechanisms with respect to storage safety and monitoring. *Mid-term evaluation 2013*

*Landschulze, Karin. (Oral popular presentation)*

Safe CO<sub>2</sub> storage below the North Sea. *SUCCESS fall meeting 2013*

*Landschulze, Karin; Pedersen, Rolf B. (Poster presentation)*

Caprock integrity for offshore CO<sub>2</sub> storage in the Norwegian North Sea – Seismic investigation of a soft sediment seafloor fracture. *AGU Fall Meeting 2013*

*Landschulze, Karin; Pedersen, Rolf B. (Poster presentation)*

Overburden Integrity for shallow CO<sub>2</sub> Storage in the Central North Sea. *ECO2 Annual Meeting 2013*

*Landschulze, Karin; Pedersen, Rolf B.; Aavatsmark, Ivar. (Poster presentation)*

Transport of CO<sub>2</sub> along possible migration pathways - how CO<sub>2</sub> or natural gasses may reach the surface. *NGF vinterkonferanse 2013*

*Pedersen, Rolf B.; Blomberg, Ann Elisabeth Albright; Landschulze, Karin; Baumberger, Tamara; Økland, Ingeborg Elisabet; Reigstad, Laila Johanne; Gracias, Nuno; Mørkved, Pål Tore; Thorseth, Ingunn Hindenes.*

Discovery of a 3 km-long seafloor fracture system in the Central North Sea. *AGU Fall meeting 2013*

## **2012**

*Landschulze, Karin. (Oral presentation, 1<sup>st</sup> prize.)*

CO<sub>2</sub> storage - State of the art. *CLIMIT PhD-Seminar 2012*

*Landschulze, Karin; Pedersen, Rolf B.; Aavatsmark, Ivar. (Poster presentation)*

Transport of CO<sub>2</sub> along possible migration pathways - how CO<sub>2</sub> or natural gasses may reach the surface. *SUCCESS Fall meeting 2012*

## **2011**

*Landschulze, Karin. (Oral presentation)*

Investigation of CO<sub>2</sub> flow along possible leakage pathways. *SUCCESS Winter Seminar 2011*

---

## 1.6 Contributions to other publications

Monastersky, Richard (with interview of K. Landschulze during AGU Fall meeting) 2013.

Seabed scars raise questions over carbon-storage plan. *Nature*, 504(7480), 339–340. Available from: <http://www.nature.com/doi/10.1038/504339a>.

Baumberger, Tamara; Bünz, Stefan; Landschulze, Karin; Pedersen, Rolf B., Blomberg, Ann E.A.; Tasanias, Alexandros; Denny, Alden R.

ECO<sub>2</sub> WP result summary report for “Environmental best practise”. *ECO<sub>2</sub> Deliverable* 2014, pp. 32

Landschulze, Marcus; Mjelde, Rolf and Landschulze, Karin. 2014.

Systematic simulation of multicomponent receiver coupling to the seafloor using rheological models. *Geophysics*, 79(6), p.9–19.

Elenius, Maria; Skurtveit, Elin; Yarushina, Viktoriya; Baig, Irfan; Sundal, Anja; Wangen, Magnus; Landschulze, Karin; Kaufmann, Roland; Chan Choi, Jung; Hellevang, Helge; Podladchikov, Yuri; Aavatsmark, Ivar; Gasda, Sarah E. 2018

Assessment of CO<sub>2</sub> storage capacity based on sparse data: Skade Formation. *International Journal of Greenhouse Gas Control*, 79, pp. 252-271

<https://doi.org/10.1016/j.ijggc.2018.09.004>





---

## **2. Manuscript compilation**





## **Paper III:**

# **Fracture Formation due to Differential Compaction under Glacial Load: a Poro- elastoplastic Simulation of the Hugin Fracture**

Karin Landschulze\*<sup>1</sup>, Marcus Landschulze<sup>2,3</sup>

<sup>1</sup> Centre for Geobiology, Department of Earth Science, University of Bergen, Allégaten 41, 5007  
Bergen (Norway)

<sup>2</sup> Department of Earth Science, University of Bergen, Allégaten 41, 5007 Bergen (Norway)

<sup>3</sup> Think Outside, Lars Hilles gate 30, 5008 Bergen (Norway)

\* Corresponding author: [karin.landschulze@uib.no](mailto:karin.landschulze@uib.no)

Submitted to Near Surface Geophysics



---

**Abstract**

A recently discovered approximately 3.5 km long seafloor fracture in the North Sea, the Hugin Fracture, raises questions to its formation and the mechanisms behind the observed fluid flow. Seismic interpretation of the Hugin Fracture suggests a relation to a sand-filled alluvial fan and differential compaction as formation mechanism. An interpreted 3D seismic section over the Hugin Fracture is used to construct a simplified 2D geomechanical model to test the formation hypothesis.

Layer properties are chosen from literature values for sand and stiff clay constructing a six-layered background model with nine channels/tunnel valleys at different depths. The poro-elastoplastic simulation uses a ramp function representing an up to 80 m thick ice sheet and a growth and decay rate of 0.8 MPa/ka. Simulation results show isotropic stress and strain distribution in the horizontally layered, isotropic part of the model totally covered by the ice. In the central, channelized part of the model a composite stress and strain pattern develops with sub-vertical focus areas tangential to channel edges. The low stress, strain and deformation values under total load increase drastically soon after the load starts to decrease, resulting in development of fractures along the focussed zones. Surface deformation such as formation of compaction ridges above stiff-clay filled channels and depression associated with plastic deformation is observed. A fracture and associated surface deformation develops above the shallowest sand-filled channel, very much resembling the observed geometry at the Hugin Fracture.

The simulation supports the formation hypothesis for the Hugin Fracture as a compaction fracture and suggests that thin ice sheets may induce differential compaction to a depth of several hundred meters.

**Introduction**

The sediments in the top 1000 m of the North Sea basin are generally poorly lithified and consolidation depends mostly on the content of fine particles or clay (Bjørlykke 2006). Geotechnical properties of these sediments will lie somewhere in-between the

values for soils and rocks, from several authors termed soft rocks (e.g. Aber 1982). The classification of soft rocks is still subject of debate (Kanji 2014). The topmost ~400 m in the central North Sea basin have undergone extensive reworking due to late Quaternary glaciation cycles creating varying conditions from open landscape with rivers to lacustrine, shallow marine and ice-covered for different time spans (e.g. Sejrup, Clark and Hjelstuen 2016). Geotechnical investigations to find optimum locations for offshore platform foundations have frequently found buried channels of Mid to Late Pleistocene age and extensive heterogeneity attributed to glacial reworking of the sediment (e.g. Williams and Aurora 1982). Several authors describe over-consolidated clayey sediments at 15 to 25 m depth below dense silty fine sands in the central North Sea basin and argue this to be caused by glacial load rather than extensive erosion of overlying sediments (Sejrup *et al.* 1987, Williams and Aurora 1982).

In general, sediment deposition from glaciers leave poorly sorted low-porosity tills. On the other hand, hydrocarbon charged Quaternary sand depositions with ice scouring marks in the Southern North Sea demonstrate the possibility for high-porosity interglacial sediment deposition (Haavik and Landrø 2014). Glacial reworking and loading-unloading cycles due to glacial advance and retreat changes sediment properties of the overburden of proposed large-scale CO<sub>2</sub> storage formations in the North Sea, Europe (e.g. GCCSI 2015, for locations). Detailed understanding of this process and its effects on Pleistocene sediments in the North Sea Basin is so far inhibited due to insufficient core data. This will likely change in the near future as new data are acquired (e.g. Barrio *et al.* 2015). One way to evaluate glacier-related processes with a potential to weaken sealing properties of the overburden, is to employ numerical simulations.

Numerical simulation of rock physics and fluid-rock interaction has become easier to facilitate with increasing computing capacity of modern computers. In addition, algorithms for elastoplastic and poroelastic models have been improved and, recently, poro-elastoplasticity has become more widely feasible and accessible (Nikolinakou *et al.* 2012). Hence, modern geomechanical models can more accurately represent the field situation depending on the amount and quality of rock or soil property



---

measurements available to constrain the model. Where distinct measurements are absent, discovered structures can, nonetheless, be better understood through simulations by applying literature properties.

The discovery of the Hugin Fracture, named after the AUV Hugin that facilitated the discovery, represents a distinct structure with virtually none available geotechnical measurements (Pedersen *et al.* 2013, and Pedersen *et al.* 2019). Landschulze, Tveranger and Pedersen (2019) describe a seismic interpretation of the Hugin Fracture located above an extensive (glaci-)fluvial channel network in the uppermost 400-500 m sediments of the western Utsira High. In the referenced paper the authors propose that the fracture formed as a result of differential compaction due to loading and unloading by glaciers. The current paper attempts to test said hypothesis employing deterministic, transient poro-elastoplastic simulation. Our approach is an attempt to falsify the hypothesis. The idea being that the fracture formation hypothesis must be omitted if the model fails to produce robust simulation results in support for the hypothesis. If the model does produce robust simulation results in favour of the hypothesis, this will indicate that the hypothesis is still valid, but it will not prove that it is correct.

## **Method**

The simulation presented in this study has been designed and computed with COMSOL Multiphysics (previously known as FEMLAB). Multiphysics is a software platform of advanced numerical methods designed to investigate a wide variety of physical problems and questions (COMSOL Inc. 2016, Li *et al.* 2009). We employed this platform in order to investigate the response of a compositely layered, heterogeneous geologic model subjected to vertical load.

Natural materials, soils especially, have usually a positive porosity and exhibit elastic as well as plastic behaviour when strained. Good simplified simulation results have been obtained through careful approximation of the real materials to be either poroelastic (sand) or elastoplastic (clay). Fluid filled porous media can be described by

Darcy's law and elastoplastic media by solid mechanics (e.g. Wood 1990). Better results are expected by including plasticity and porosity for all materials as it is possible in the emerging poro-elastoplastic models (e.g. Lee *et al.* 2015).

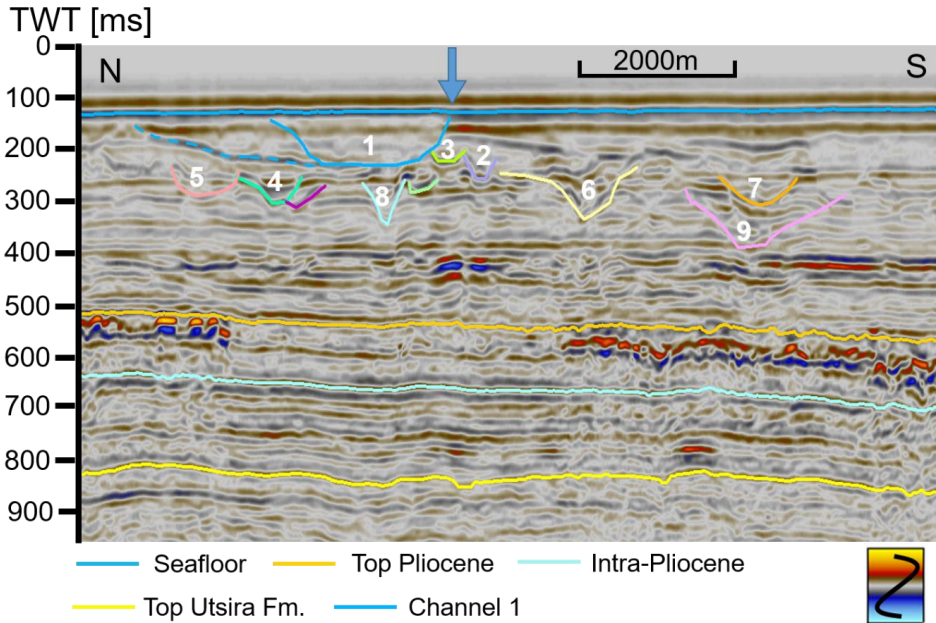


Figure 1: Interpreted seismic section as geometry input (for details on seismic interpretation see Landschulze, Tveranger and Pedersen 2019). Channels are indicated with coloured lines and white numbers, the Hugin Fracture location is indicated with an arrow. Some major horizons are indicated, vertical exaggeration is 5 times.

There are many choices to consider when designing geomechanical simulations, one of them concerns whether to consider the gravity force. For our model, we assume sediment parameters for normally consolidated sediments, i.e. gravity and sediment accumulation. By employing such values for e.g. porosity, permeability and density, we implicitly include the constant gravity force. We focus on the dynamic change of the ice load rather than the total load (weight of ice and gravity).

Prior to setting up the model for testing the fracture formation hypothesis for the Hugin Fracture, a benchmarking of the software was carried out, namely replicating the poro-elastoplastic model of a spherical salt body as described in Nikolinakou *et al.* (2012).

After confirming that the proprietary software did produce similar results as those reported by Nikolinakou *et al.* (2012), a poro-elastoplastic 2D model from a seismic section over the Hugin Fracture was constructed. In the following section we will give an overview of the workflow and important mathematical relations for the model.

### *Mathematical model*

The mathematic models presented in this section correspond in essence to the work flow in Multiphysics (COMSOL Inc. 2016). The governing principles incorporated in the proprietary simulation tool are based on the work of Terzaghi 1943, Biot 1941, Tang, Hededal and Cardiff 2015 and others. An interface couples two physical models, one poroelastic and one elastoplastic, to jointly compute a poro-elastoplastic simulation. We start by describing the poroelastic part of the model.

The poroelastic model, based on a combination of Terzaghi's and Biot's theory of consolidation couples the porous soil and Darcian fluid flow in the soil skeleton (Biot 1941, Terzaghi 1943). Fluid flow in a porous medium due to the hydraulic potential field is described by Darcy's law, with neglected gravity commonly written as:

$$\mathbf{q} = -\frac{\kappa}{\mu} \nabla p, \quad (1)$$

where  $\kappa$  is the permeability,  $\mu$  the fluid dynamic viscosity,  $p$  the fluid pressure,  $\mathbf{q}$  the Darcy velocity and  $\nabla$  the nabla operator. Formulated with the poroelastic interface equation (1) becomes

$$\frac{\partial \rho \varphi}{\partial t} + \nabla \rho \left[ -\frac{\kappa}{\mu} \nabla p \right] = Q_m, \quad (2)$$

$Q_m$  is the mass source term,  $\varphi$  the porosity and  $\rho$  the fluid density. In order to combine the solid mechanics with the Darcy flow, the storage coefficient  $S_t$  needs to be introduced. The storage coefficient can be defined as:

$$S_t = \varphi \chi + \frac{\partial \varphi}{\partial p}; \quad \chi = \frac{1}{\rho} \frac{\partial \rho}{\partial p} \quad (3)$$

$\chi$  is the fluid compressibility. The poroelastic equation (2) can be substituted by the equations in (3) to:

$$\rho S_t \frac{\partial p}{\partial t} + \nabla \rho \left[ -\frac{\kappa}{\mu} \nabla p \right] = Q_m. \quad (4)$$

The linear solid mechanics theory describes that the deformations are proportional to stress and reversible. This assumption is well known as generalised Hooke's law:

$$\boldsymbol{\varepsilon} = \frac{\boldsymbol{\sigma}}{3K} = \frac{\tau_{ij}}{G_{ij}}, \quad (5)$$

In Einstein notation and with  $\boldsymbol{\sigma}$  = stress tensor,  $K$  the bulk modulus,  $\tau$  the shear stress and  $G$  the shear modulus. A poroelasticity interface was used to couple the linear solid mechanics with Darcy's law and to account for poroelastic deformation. Based on Tang, Hededal and Cardiff (2015), the interface can be mathematically summarized as:

$$\nabla \left( \left( S_t - \alpha_B (p_f - p_{ref}) \right) \mathbf{I} \right) + \frac{\partial^2 \mathbf{u}}{\partial t^2} = \nabla \boldsymbol{\sigma} \quad (6)$$

and

$$\rho_f S_t \frac{\partial p_f}{\partial t} + \nabla \rho_f \mathbf{u}_f = Q_m - \rho_f \alpha_B \frac{\partial \varepsilon_{vol}}{\partial t} \quad (7)$$

with the Biot-Willis coefficient  $\alpha_B$ , reference pressure  $p_{ref}$ , the identity matrix  $\mathbf{I}$ ,  $p_f$  and  $\rho_f$  representing the fluid pressure and  $\varepsilon_{vol}$  the fluid density strain. The Biot-Willis coefficient describes the interaction between confining stress and pore pressure.

### *Porous matrix deformation*

For the poroelastic stress tensor we consider an isotropic porous material under plain strain conditions. Equation 8 describes the norm for a 2D poroelastic (Wang 2000):

$$\begin{bmatrix} \sigma_{xx} \\ \sigma_{yy} \\ \sigma_{xy} \end{bmatrix} = \frac{E}{(1+\nu)(1+2\nu)} \begin{bmatrix} 1-\nu & \nu & 0 \\ \nu & 1-\nu & 0 \\ 0 & 0 & 1-2\nu \end{bmatrix} \begin{bmatrix} \varepsilon_{xx} \\ \varepsilon_{yy} \\ \varepsilon_{xy} \end{bmatrix} - \begin{bmatrix} \alpha_B p & 0 & 0 \\ 0 & \alpha_B p & 0 \\ 0 & 0 & \alpha_B p \end{bmatrix} \quad (8)$$

With  $E$  = Young's modulus,  $\nu$  = Poisson's ratio of the porous material for the drained case,  $\alpha_B$  = Biot-Willis coefficient and  $p$  = fluid pressure. The term  $\alpha_B \cdot p$  is often described as fluid-structure interaction. Since we added poroelasticity to our model, equation 8 contributes as a poroelasticity node in the simulation set up.

### *Elastoplastic model*

The elastoplastic model is described through linear isotropic Young's modulus  $E$ , Poisson ratio  $\nu$  and density  $\rho$ . Plasticity is assumed with small strain approximation yielding following equation for the elastoplastic model (e.g. Tang, Hededal and Cardiff 2015):

$$d\sigma_e = 2\mu(d\boldsymbol{\varepsilon} - d\boldsymbol{\varepsilon}_{ep}) + \lambda \text{trace}(d\boldsymbol{\varepsilon} - d\boldsymbol{\varepsilon}_{ep}), \quad (9)$$

with incremental strain  $d\boldsymbol{\varepsilon}$ , effective plastic incremental strain  $d\boldsymbol{\varepsilon}_{ep}$ ,  $\mu = E/2(1 + \nu)$  and  $\lambda = E \nu / ((1 + \nu)(1 - 2\nu))$ . The relationship between the strain tensor  $\boldsymbol{\varepsilon}$  and displacement  $\mathbf{u}$  is:

$$d\boldsymbol{\varepsilon} = \frac{1}{2} \{ \nabla d\mathbf{u} + (\nabla d\mathbf{u})^T \}. \quad (10)$$

The soft soil in our simulation has a Poisson ratio of almost 0.5, causing instability in volumetric change calculations. This can be illustrated by the bulk modulus that measures volumetric change and tends to infinity as the Poisson ratio approaches 0.5:

$$K = \lim_{\nu \rightarrow 0.5} \frac{E}{3(1-2\nu)} = \infty \quad (11)$$

To avoid an ill-posed numerical problem, we employed a mixed formulation where we added a dependent pressure variable to the deviatoric stress tensor  $S$  and now need to solve a nearly incompressible problem:

$$S = S_0 - \frac{\text{trace}(\mathbf{C}:\boldsymbol{\varepsilon})}{3} + p_w, \quad (12)$$

with  $\mathbf{C}$  as fourth order constitutive Cauchy stress tensor; the “:”-symbol indicates a contraction over two indices ( $\boldsymbol{\sigma} = \mathbf{C}:\boldsymbol{\varepsilon} = C_{ijkl} \cdot \varepsilon_{kl}$ ).

Poroelastic fluid flow under static conditions and without body force can be described as:

$$\nabla(\sigma_e - pI) = 0, \quad (13)$$

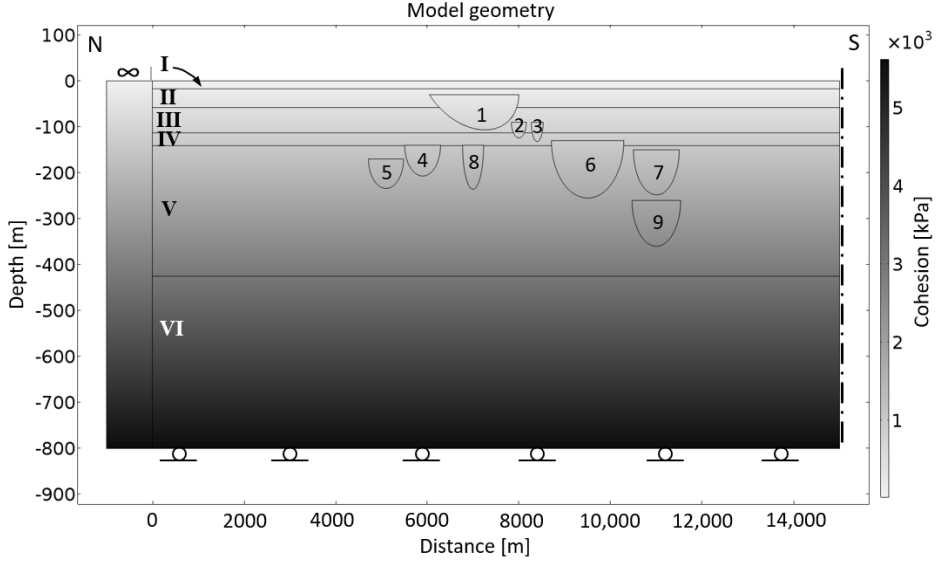


*Figure 2: Geometry inferred from interpreted seismic section in Figure 1. A total of six layers is included representing different seismic units. The numbered channels/tunnel valleys are simplified from their seismic appearance (figure 1). The grey-shaded colouring indicates increasing cohesion with depth at a linear rate of 7 kPa/m. An infinity layer is located at the northern side of the model and symmetry is defined at the southern end of the model. Vertical movement is inhibited at the lower boundary while lateral movement is allowed on a roller boundary.*

with  $\sigma_e$  the effective stress tensor and  $p$  the pore pressure. Displacement in the poroelastoplastic model can be described by inserting equations 3 and 4 in equation 1, yielding:

$$\begin{aligned} & \nabla\{\mu\nabla d\mathbf{u} + \mu\nabla(d\mathbf{u})^T + \lambda\mathbf{I} \cdot \text{trace}(\nabla d\mathbf{u})\} \\ &= \nabla\{2\mu d\boldsymbol{\varepsilon}_{ep} + \lambda\mathbf{I} \cdot \text{trace}(d\boldsymbol{\varepsilon}_{ep})\} + \nabla dp \end{aligned} \quad (14)$$

We want to simulate the geomechanical deformation sub-seafloor during a time-varying vertical load and employ the direct time-dependent solver MUMPS (Amestoy *et al.* 2001); this ensures an efficient coupling between the mathematical model and the geometric mesh. A 2D model based on seismic interpretation of the subsurface at the Hugin Fracture is employed to investigate the possibility of fracture formation due to glacial load. An unstructured triangular mesh was chosen to provide a fine mesh with acceptable computing time. Solver configuration and mesh geometry are described in more detail in appendix A.

#### *Yield criterion and hardening rule*

Linear elastic materials deform under load and relax to its original form when the load is relieved. If a certain stress level (yield stress) is exceeded in an elastoplastic material, like soft sediment, irreversible plastic deformation takes place and increases during unloading.

In our simulation we consider the original sediment ductile rather than brittle because the porous sediment skeleton will deform under tensile stress without fracturing (until it reaches the maximum yield stress). Using this assumption, the von Mises yield function is a useful approximation. Von Mises yield criterion is defined as:

$$\sigma_{mises} = \sqrt{\frac{(\sigma_1 - \sigma_2)^2 + (\sigma_2 - \sigma_3)^2 + (\sigma_3 - \sigma_1)^2}{2}}, \quad (15)$$

where  $\sigma_i$  is the main stress direction with  $i = 1, 2, 3$ . The resulting yield stress function  $F$  is then:

$$F = \sigma_{mises} - \sigma_y, \quad (16)$$

with the yield stress  $\sigma_y$ . In our simulation we also include hardening during plastic deformation and we assume linear isotropic hardening with the isotropic tangent modulus  $E_{Tiso}$ .

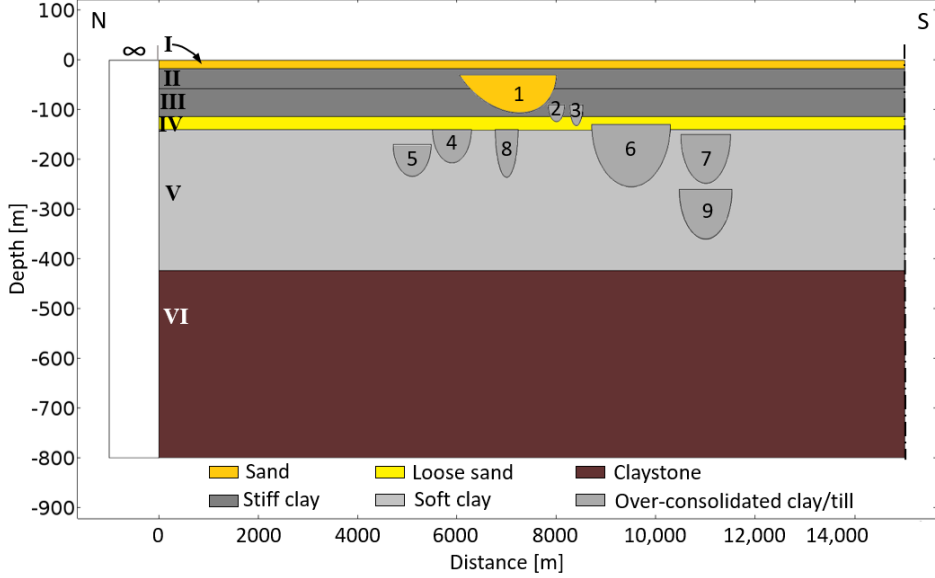


Figure 3: Parametrization sketch of the model layers. Roman numerals indicate layers and Arabic numerals indicate channels as in Figures 1 and 2. Sediment descriptions are listed in appendix B and the different parameters for each layer are found in appendix C.

The yield stress  $\sigma_y$  then is the summation of the initial yield stress  $\sigma_0$  and the hardening stress  $E_{hard}\epsilon_{ep}$  which can be expressed as:

$$\sigma_y = \sigma_0 + E_{hard} \epsilon_{ep} = \sigma_0 + \frac{E_{Tiso} E}{E - E_{Tiso}} \epsilon_{ep}. \quad (17)$$

## Model description

### Geometry and Mesh

The 2D geometry is based on an interpreted seismic section from Landschulze, Tveranger and Pedersen (2019) (Figure 1) and additional seismic data from site surveys at wells 16/4-2 and 16/4-7 (Norsk Hydro AS 1990 and Fugro Survey AS 2012, for



details see appendix B). The seismic section in Figure 1 is part of a 3D seismic dataset. It reveals mostly horizontal layers to a depth of  $\sim 400$  m, with some small-scale ( $< 2$  km) variations. Local variations in the interval thickness between the two well sites may occur, but the layer sequence is continuous throughout a much larger area. Description of sediment composition in the layers are also taken from the drilling site survey report for well 16/4-7 which was provided by the Norwegian Petroleum Directorate and the operator Lundin Norway AS ([www.npd.no](http://www.npd.no); Fugro Survey AS 2012).

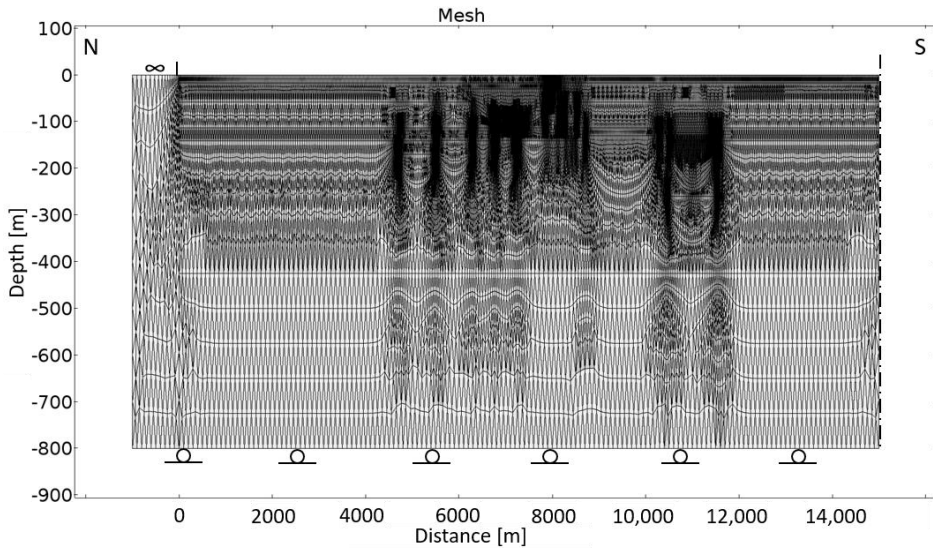


*Figure 4: Unstructured triangular mesh of the model domain shown in figure 2. Thin layers, e.g. units I and IV from Figure 2, and areas of large changes around the channels are represented by a larger number of mesh cells. The infinity layer on the northern side of the model is sufficiently represented by a lower number of mesh cells while the channels are densely populated. The southern symmetry boundary and bottom rollers are also indicated. For mesh statistics see appendix A.*

A number of channel structures have been identified, for details on the seismic interpretation the reader is referred to (Landschulze, Tveranger and Pedersen 2019). The numbered channel structures in Figure 1 are included in the 2D model.

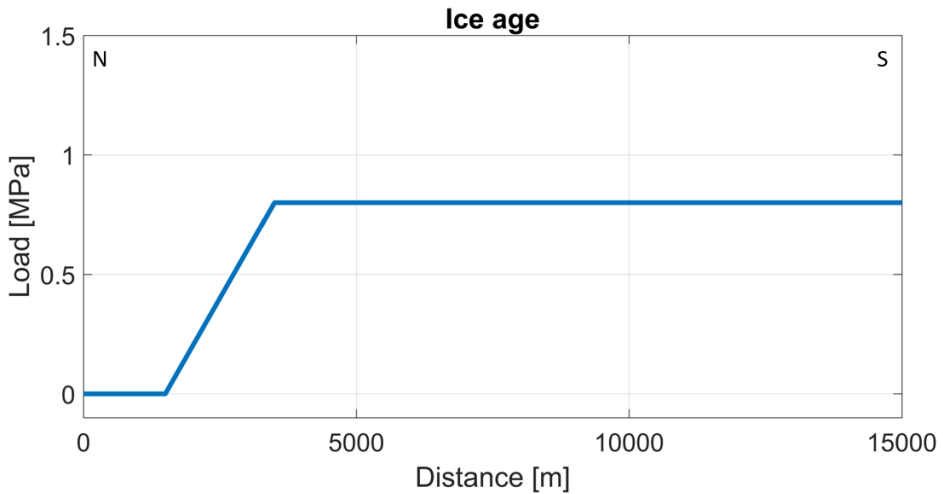


*Figure 5: Lateral load distribution of the modelled glacial load over the upper model boundary at maximum load, i.e. 10 ka simulation time. The ramp starts at 1500 m is 2000 m wide and has a maximum amplitude of 0.8 MPa. The curve grows and decays linearly over the simulation run time with 0.8 MPa / 10 ka.*

The inferred and somewhat simplified model geometry is shown in Figure 2. For simplicity, all layers are assumed to be horizontal and the channels are modelled as symmetric halve-ellipses, except for channel 1. In nature, some Pleistocene layers show locally pronounced deviation from the horizontal model due to erosion (see seismic section in appendix B). Due to lack of local or regional Pleistocene horizon maps and to avoid unnecessary complexity in the model the local variations are ignored. The channels are modelled as halve-ellipses, a simplification for the model that may result in steeper channels walls than reality. All channels are modelled symmetric axis-symmetrical. However, channel 1 is modelled asymmetric for two reasons: 1) an asymmetric channel bottom could comply with an alternative seismic interpretation than presented in Figure 1 and 2) an asymmetric channel will help to illuminate the significance of axis-symmetry and steep channel walls when compared to the other axis-symmetrical channels.

Meshing aimed at minimizing the number of elements and, hence, computing time by at the same time providing sufficient coverage in areas of rapid changes. This is achieved by high density of small elements in areas of expected large changes, i.e.

---

heterogeneities and edges, while fewer, larger elements sufficiently represent the homogeneous areas (Figure 4). The simulations were run on a 16-core cluster computer with 128 GByte RAM. An average number of 188487 degrees of freedom (DOF) plus 1092750 internal DOFs were solved and the computing time was 39 minutes on average (for mesh statistics see appendix A).

### *Boundary conditions*

The boundary on the left side of the model (Figure 2) contains an infinite element domain that virtually stretches the layer to a very large distance from the region of interest to reduce boundary effects. This part of the model will not be affected by the glacial load on the channelized part but allows for stress relieve as it naturally occurs over distance away from glacier fronts. The advantage of using an infinity layer over a lateral extension of the model is a lower number of mesh cells and, hence, computing time. The right-side boundary is set to symmetry, virtually mirroring the model conditions to provide numerical stability and reduce element numbers. Based on observation in the seismic data, a similar channelized area may be present in other areas. The bottom is set to a horizontal roller boundary to allow only for lateral movement with zero vertical displacement. The sediment in the model can compress and relax elastically, deform plastically and move laterally under loading, reflecting to a good extent the natural processes taking place below and in front of an ice sheet (e.g. Boulton and Dobbie 1993).

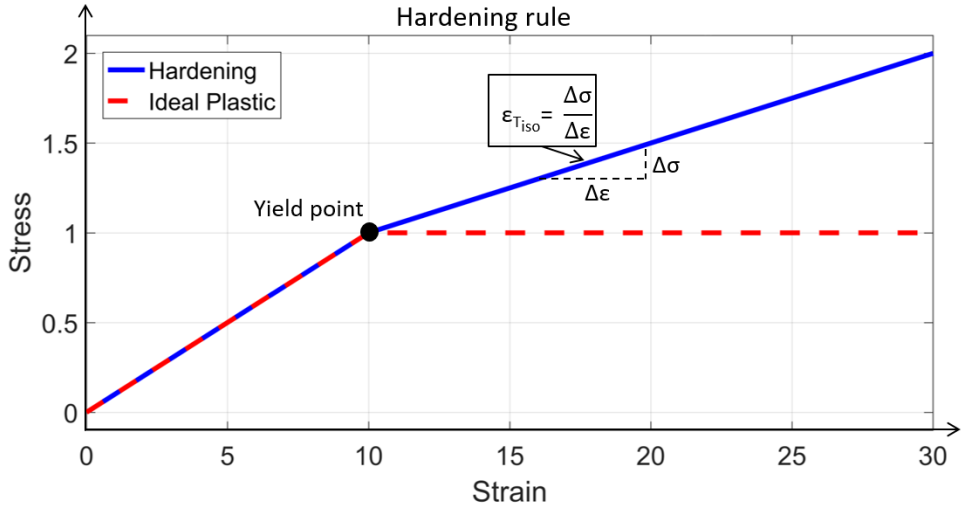


Figure 6: Plastic deformation and hardening rule according to equation 12. Compared to ideal plastic deformation (red curve), where strain accumulates at constant stress from the yield point, the simulations in this study assume hardening behaviour, i.e. higher stress is required for further strain accumulation (blue curve).  $\varepsilon_{T_{iso}}$  governs the gradient of the stress/strain curve (see also equation 16).

### Ice load

Quaternary glaciations in Northern Europe and the North Sea have long been studied to establish time lines of advancing and retreating ice shields as well as total ice coverage and thickness (see e.g. Løseth, Rauiline and Nygard 2013, Sejrup *et al.* 2000, Sejrup, Aarseth and Haflidason 1991). Recent work by Sejrup *et al.* (2016) shows that around the Hugin Fracture the ice moved northwards, similar to ice movement in the Norwegian Channel. Accordingly, the ice load in the simulation arrives from the south and propagates northwards over a time span of 10 ka before it retreats again. A ramp function was chosen to account for the slope of a natural glacier towards a plateau centre (Figure 5). The ice grows linearly with 0.8 MPa / 10 ka and melts at the same rate. Assuming a density of 0.931 kg/m<sup>3</sup> this corresponds to a growth rate of about 8 m ice per 1000 years and a maximum ice thickness of 80 m. The ice thickness is low compared to modern glaciers at e.g. Iceland (Boulton and Dobbie 1993). Model symmetry is assumed for both the sub-bottom and the ice load, this equates to a

modelled ice sheet with a total width of 27 km, twice the length as the model presented in Figure 3.

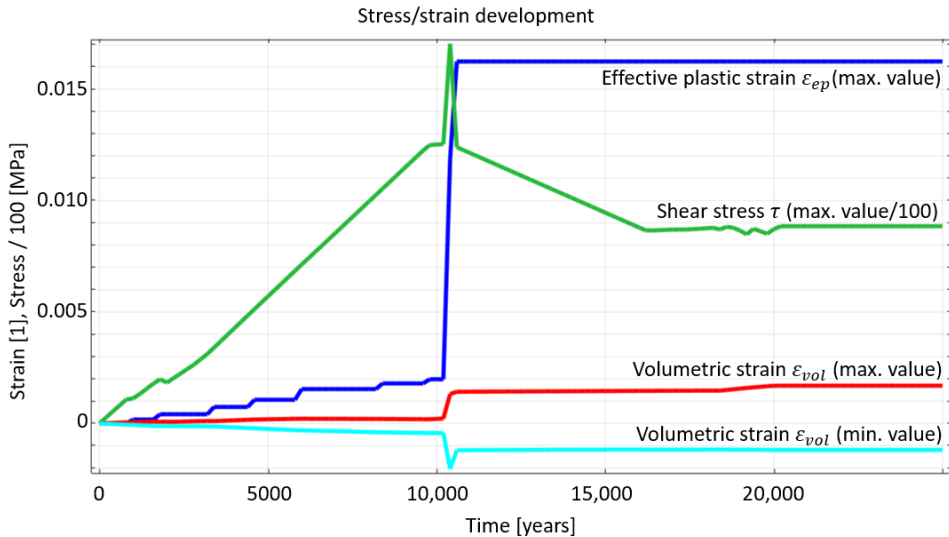


Figure 7: Temporal development in maximum values for different simulation result parameters. The top load increases over the first 10 ka and decreases for another 10 ka. The pronounced stress drop at 10,400 a simulation time is interpreted as “fracturing” and after that the model is no longer a valid representation of the natural processes. The plateau in maximum effective strain may reflect volume neutral deformation (see text for discussion).

### Hardening rule and cohesion

The simulations in this study assume strain hardening behaviour of the modelled sediments, as shown in Figure 6. Different materials and their stress/strain behaviour have been studied extensively, such as Berea sandstone (Churcher 1991) and London clay (Dewhurst, Yang and Aplin 1999). The material properties at the location of the Hugin Fracture are uncertain due to lack of core material. However, strain hardening is assumed to be the dominating stress/strain behaviour for the mostly clay-dominated sediments (Wood 1990, Sejrup *et al.* 1995). Strain hardening behaviour is related to increasing stiffness/brittleness of the sediment as the stress/strain condition passes beyond the yield point. The higher the isotropic tangent modulus ( $E_{Tiso}$ ), the larger stress is required to further increase the strain (see equation 17). Increased stiffness renders the material more prone to brittle failure, i.e. fracturing.

In addition to strain hardening, a depth-dependent cohesion is assumed (Figure 2), reflecting an increase in cohesion with depth due to increasing compaction of 7 kPa/m.

### *Material properties*

Tests and measurements on the actual sediments being absent, material properties had to be determined based on descriptions from drilling site survey reports and literature values. Sediment properties for pure sands and clays such as porosities, densities and Young's modulus are taken and derived from Hamilton (1971) (see Appendix C). In the model, the layers are assumed to be either sand-dominated or clay-dominated with some mixtures in-between as indicated by sediment descriptions from drilling site surveys (see also appendix B). For an easier adaptation of the pure end member sediment properties to assumed mixtures in the distinct layers, we defined a mixing relation to compute the needed parameters:

$$value_{layer} = value_{sand} + (value_{clay} - value_{sand}) \cdot k_{layer}, \quad (18)$$

where *value* may be any of the desired material properties, e.g. porosity, density or Young's modulus, and *k* is a layer-specific mixing value, ranging from 0 to 1.

Equation 18 defines a linear mixing relation with the end member values being pure sand and clay, respectively. In the case of pure sand, a value of  $k=0$  yields the desired value for sand. For  $k=1$ , equation (18) yields the desired value for pure clay, and for other values of  $0 < k < 1$  it yields a value in-between these end-members. End member values for pure sand and pure clay are taken from Hamilton (1971) and the sand/clay mixing parameters presented in Appendix C are derived from the sediment descriptions in the drilling site survey report from well 16/4-7 (Fugro Survey AS 2012, see appendix B). Layers described as stiff clay were assigned a *k*-value close to 1 and layers described as sandy were assigned a *k* value close to 0. The Aberdeen Ground Witch formation is described as soft clay with several sand layers and embedded boulders. Therefore, it was assigned a *k*-value of 0.2, which is closer to sand than to clay.

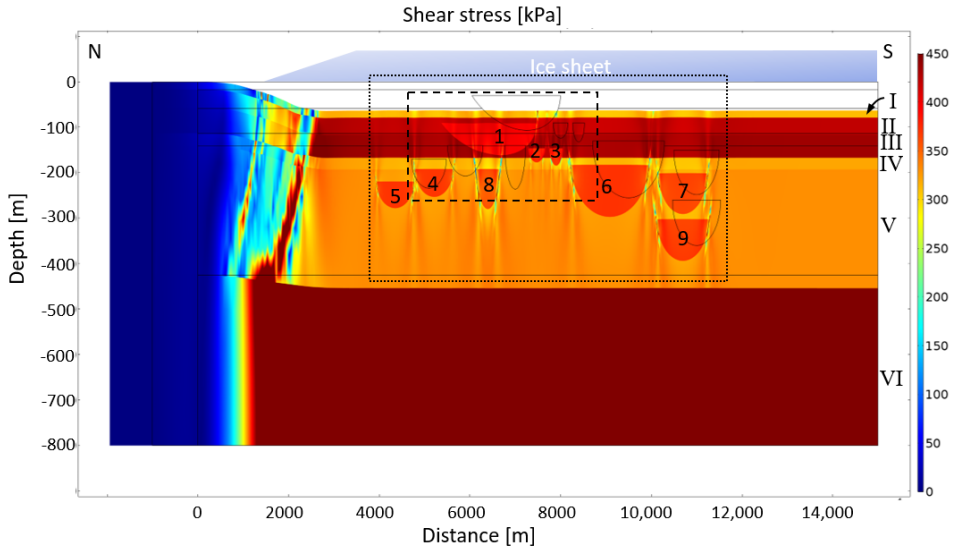


*Figure 8: Shear stress distribution at 10.4 ka. Between 500 m and 2500 m the ice load induces a flexure with a large-scale stress pattern in front and below the rising ice sheet starting at 1500 m. Later figure extent is indicated by black rectangles; dotted line for Figures 8, 11 and 14, dashed for Figures 9, 12 and 15. Original model geometry indicated by black lines. The Arabic numerals indicate displaced channels, Roman numerals point to displaced layers, the Vertical displacement exaggeration is 50.*

The deeper channels have clay properties similar to layer IV (Fisher Fm.), hereby neglecting the sand fill at the base of the channels that is reported in most studies on tunnel valley fills in Northern Europe (e.g. Kehew, Piotrowski and Jørgensen 2012). The shallow channel 1 was given the properties of pure sand, that slightly exaggerates the fill interpretation based on gamma-ray and resistivity logs from wells 16/4-2 and 16/4-1 (Landschulze, Tveranger and Pedersen 2019). These simplifications should not change the qualitative results of the simulations and they are motivated by maintaining a manageable model complexity. A detailed list of material properties can be found in appendix C.

## Results

The simulations were stable throughout the 20 ka load/unload cycle with a peak in maximum stress after 10.4 ka (Figure 7). The curves in Figure 7 represent the maximum value over the entire model domain for each time step and parameter and is, thus, not necessarily the same point in space. Stress values are scaled to 1/100 of original value. Note the stress peak (green curve) with associated large step in plastic strain. Fracturing is the most likely cause for the observed stress drop towards the next time step, rendering interpretation of the remainder of the simulation unreliable. Consequently, only simulation results from 10.4 ka simulation time are discussed and subsequent figures show results from this time step. At 10.4 ka the total glacial load has reduced for 400 years at a rate of 0.8 MPa / 10 ka, i.e. at that time the maximum load of 8 MPa has been reduced by 32 kPa. However, this slight decrease in glacial load results in a dramatic increase in plastic deformation and (likely) fracturing towards the next time step (Figure 7). Less pronounced steps and peak/trough are observed in the maximum and minimum volumetric strains.

The plateau in plastic and volumetric strains could be interpreted as volume neutral deformation after fracturing (Figure 7). However, the model was not defined with any kind of fracture-behaviour, so that the part of the simulation after fracturing occurred is disregarded in the remainder of this paper.



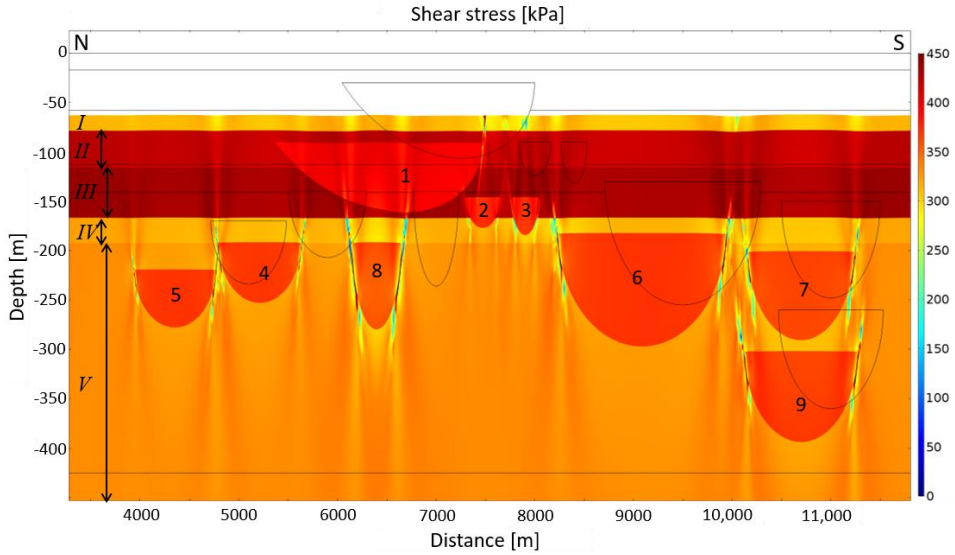


Figure 9: Shear stress distribution in the heterogeneous channelized central part of the model. Original model geometry indicated by black lines and Arabic numbers; italic Roman numbers indicate displaced layers. Vertical displacement exaggeration is 50.

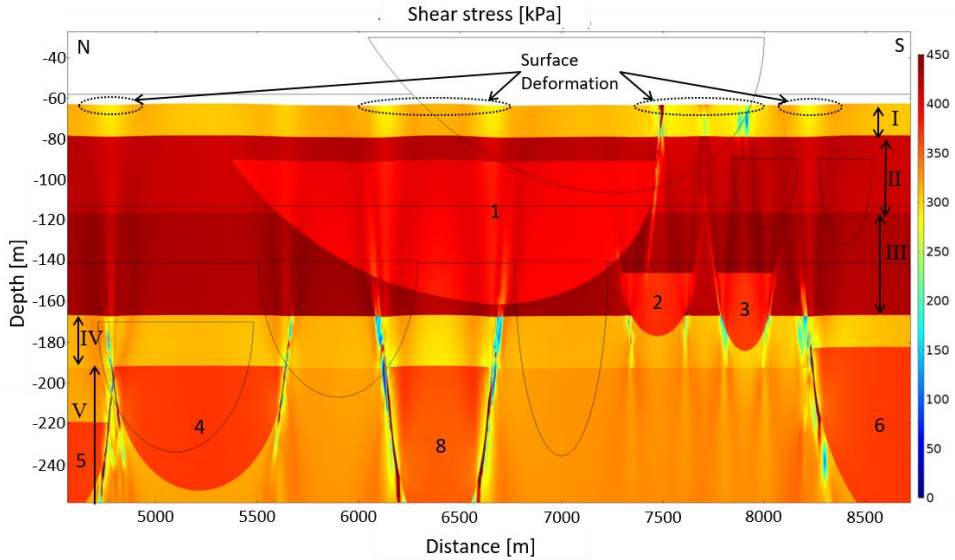
### Load-induced shear stress

Figure 8 shows the final shear stress distribution for the whole model domain. As expected, at the infinity boundary (N) no stresses accumulate because the load influence is absent and stresses can dissipate. On the southern side of the model, stresses accumulate uniformly inside the distinct layers according to the respective geomechanical parameters. The coloured layers appear clearly displaced and somewhat compressed compared to the original layer position in the wire line model (black lines). The vertical displacement is 50 times exaggerated to make it easily visible in the figures; the layers are vertically displaced by 1.2 m.

On the southern isotropic part (right side in Figure 8) no differential stress is induced during loading and unloading. On the northern end of the model (left side in Figure 8) the influence of the ice sheet is absent in the infinity layer. In the transition area, where the influence of the glacial load starts and grows southwards to its maximum thickness, strong changes in stress accumulation associated with a prominent surface flexure are observed (Figure 8). The top Pliocene unit (layer VI) shows the response of a

homogeneous half-space to the ramp-form defined ice load with high shear stress below the ice sheet and no shear stress in front of the ice sheet. The transition from ice sheet to free surface is marked with a gradual decrease in shear stress in layer 6 (Top Pliocene). The largest stresses are found in units II and III, two over-consolidated clay layers (Swatchway and Coal Pit Fm., Fisher Fm.), reflecting their increased ability to withstand shear stresses. The sandier layers, i.e. units I, IV and V can partly adjust to the stress (compaction due to grain rearrangement and pore deformation) resulting in lower shear stress values. In the heterogeneous channelized central part of the model, stress accumulation is uniformly distributed in each layer and channel. All channels show similar large shear stress, although channel 1 contains loose sand and the others stiff clay. In addition, focussed sub-vertical stress accumulations are evident at most channel edges. This pattern of differential stress zones in units I through V, seemingly connected to the heterogeneities represented by the channels, developed under a uniform ice load (see Figure 9 and 10 for more detail). Very high stresses in close vicinity to the lowest stresses are present in focussed zones tangential to the channel edges indicating differential compaction and rebound around these heterogeneities. Layer 6 seems unaffected by these differential stress lenses. Subsequent figures focus on the heterogeneous central part of the model.

A closer look at the shear stress distribution in Figure 9 reveals that the focussed stress accumulations consistently coincide with the channel edges, except for the northern edge of channel 1. Strong changes in stress amplitude over short distances (meter scale, see Figure 10) from around 400 kPa to around 150 kPa and less appear inside the focus areas. Stress shadows with lower stress values are evident below most channels, especially below channel 8. Note that the channels are displaced down and northwards from their original location as indicated by the black lines and numbers. Some surface deformation such as gentle elevations and small depressions are barely recognised in Figure 9; they are easier to see in Figure 10.



*Figure 10: Detail from Figure 9 of the shallowest channel 1 with sand fill and asymmetric shape. Focussed tangential stress zones are clearly visible at all channel edges, except for the northern part of channel 1. Also visible is the emerging topography due to differential compaction (ellipses). Original model geometry indicated by black lines, Arabic numerals indicate displaced channels, Roman numerals indicate displaced layers. Vertical displacement exaggeration is 50.*

Channel 1 appears to experience higher shear stress levels than layers I, IV and V, although channel 1 has material properties according to pure sand whereas the layers represent different kinds of sand-clay mixtures. This is a direct result of the model geometry and the properties of layers II and III that surround channel 1. Layers II and III represent stiff clay properties and, hence, they can withstand higher shear stress than the sandier layers I, IV and V that respond with porosity reduction. In the poro-elastoplastic model, the pore pressure build-up in channel 1 is influenced by the compaction of the surrounding low-porosity layers II and III. In addition, the layers are hydraulically open to the north and south, while the channel is closed. This affects directly the embedded channel structure, that is forced to undergo similar shear stress as the surrounding stiff clay layers. The pore pressure cannot dissipate through the low porous layers II and III and, hence, the resulting, effective shear stress in channel 1 is lower than the surrounding layers but higher than for comparable sandy layers.

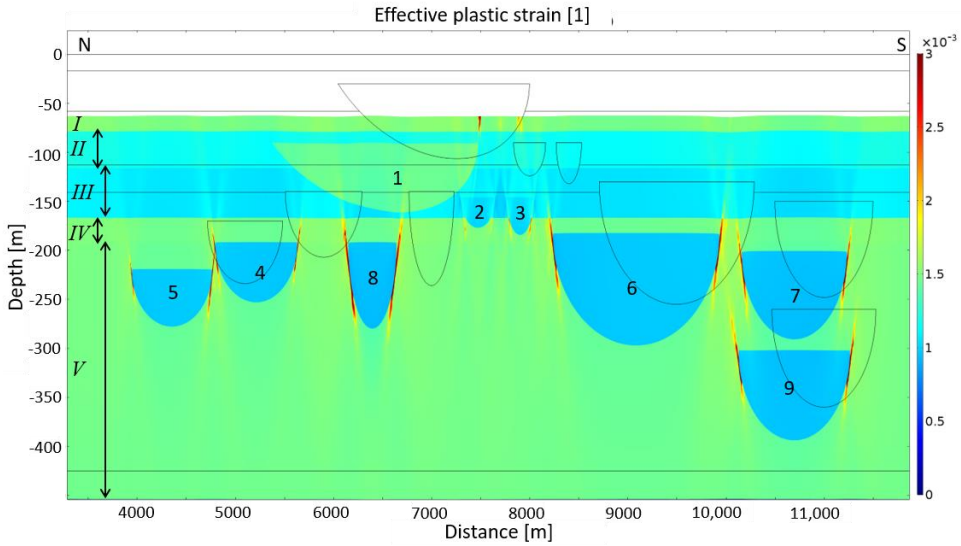


Figure 11: Effective plastic strain display of a model with isotropic hardening of  $\varepsilon_{T_{iso}} = 100 \text{ MPa}$  (compare Figure 7). Original model geometry indicated by black lines and Arabic numbers; italic Roman numbers indicate displaced layers. Vertical displacement exaggeration is 50.

Figure 10 shows the stress distribution around channels 1 in more detail. Note that the channels are displaced down- and northwards compared to the original model geometry as indicated by the black lines. The stress magnitude is governed by material properties as can be seen at the transition from the sandier unit IV (yellow-orange) to the more clayey (red) layer III and at the transition from the clayey layer II (red) to the sandy (orange) layer I near the top of the model (80 m depth). Note the maximum stress values in the topmost sub-vertical part of the stress zone connected to the channel 1's southern edge, interpreted to represent a failure area like the Hugin Fracture. Inside channel 1, the shear stress distribution shows stress variations nucleating at the underlying channel 8 that continue through channel 1 (Figure 10). Similar subtle stress variation from channel 4 is barely recognized to continue inside channel 1 but can be identified by slightly less stress near the surface above the southern edge of the displaced channel 4. The northern edge of channel 2 is also origin of a tangential stress pattern that seems to cross inside channel 1. However, the stress variation inside channel 1 seems to disappear towards the surface.

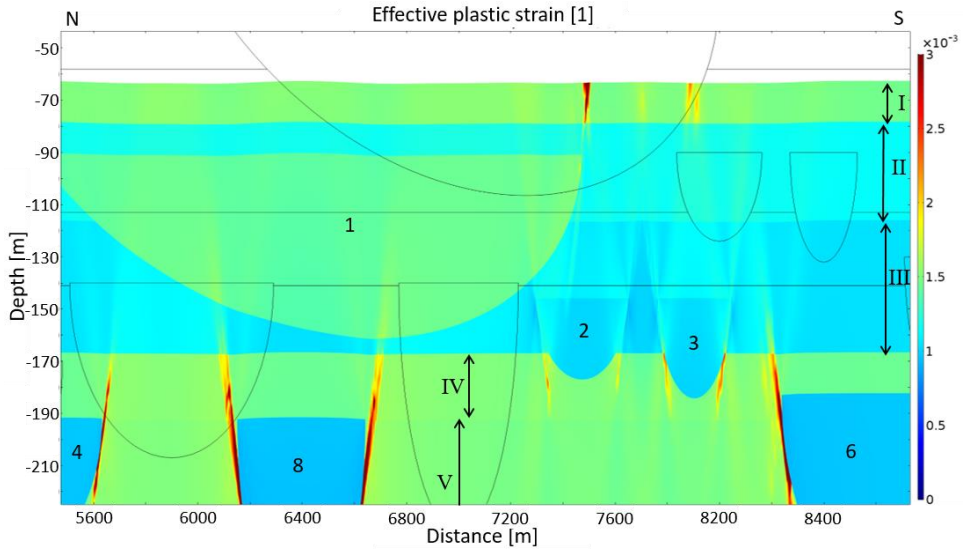


Figure 12: Detail from Figure 11 around channel 1. Note the strong plastic deformation in the topmost layer above the southern edge of channel 1. This correlates with the stress distribution in figures 7-9 and is similar to the observed Hugin Fracture. Original model geometry indicated by black lines and Arabic numbers; italic Roman numbers indicate displaced layers. Vertical displacement exaggeration is 50.

In addition, Figure 10 shows stress shadows, i.e. less stress compared to adjacent areas, below channels 3, 7, 8 and 9. These stress shadows result from the heterogeneities in the layers, i.e. channel bodies, that accumulate more stress than if they were filled with the same material (homogeneous case). This leads to the observed stress relieve in the surrounding layer(s).

#### *Plastic deformation and volumetric strain*

Surface deformation is most obvious in the area just above channel 8 (between 6000 m and 7000 m in the model); the slight elevation does continue at depth, it is also present in the layer boundaries towards layers II and IV, as well as the top boundaries of channel 1 and 8. In layer IV it coincides with the area of the stress shadow, showing smaller shear stress values just above channel 8 than in the rest of the layer. The surface elevation is identified as a compaction ridge. Both elevation and the other surface deformations increase in the further course of the simulation beyond time step 10.4 ka.

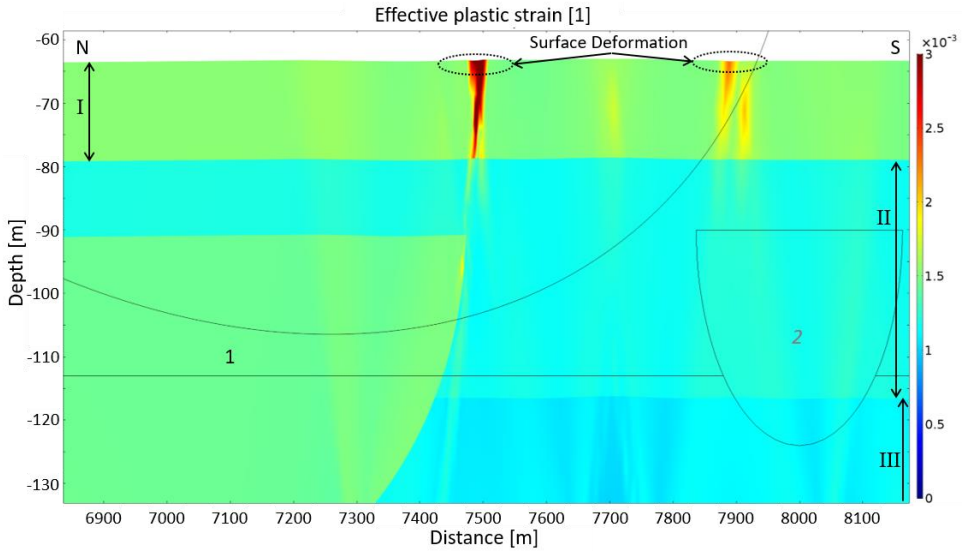


Figure 13: Enlarged section from Figure 11 displaying the developing fracture above channel 1. Original model geometry indicated by black lines. Arabic numbers indicate the channel locations, black for displaced, grey for original location. Roman numerals indicate displaced layers. Slight elevation enclosing a central depression is seen on top of a zone of large plastic deformation areas (black ellipses).

Like Lewis, Hall and Couples (2009) we use effective plastic strain and volumetric strain to predict opening of fractures. Von Mises effective plastic strain distribution in the model at 10.4 ka is shown in Figures 10-12 and the total volumetric deformation is shown in Figures 13-15. In general, plastic and volumetric deformation is largest for unconsolidated sand layers I and IV, reflecting volumetric adjustments to stress accumulation. The clay or till-filled channels show lower plastic deformation, but higher stress accumulation. Plastic deformation accumulates in focussed areas tangential to the channel edges, except for the northern edge of channel 1. As plastic deformation increases brittleness of the sediment, fracturing is most likely to nucleate in the focussed areas along the edges of the channels. Plastic and volumetric deformation occurs in the same focussed sub-vertical areas tangential to the channel edges as seen in the stress distribution (Figures 7-9). Different layers exhibit different amounts of plastic deformation, the softer layers (I and IV comprising loose sand while V comprises soft clay) experiencing more deformation than layers II and III comprising

stiff clay (see Figure 3 for layer parametrization). Accordingly, the only sand-filled channel (channel 1) displays larger plastic deformation values than the other channels that are filled with stiff clay (Figure 11). Since all the other channels are assigned properties of stiff and, hence, already strained clay, little (additional) plastic deformation is expected.

A closer look at the plastic deformation around channel 1 (Figure 13) reveals large values in focussed areas tangential to channels 4, 8 and 6 inside the sandy layer IV (Ling Bank Fm.) and the soft clay layer V (Aberdeen Ground Fm.). The amount of plastic deformation inside the focussed areas changes abruptly at the boundary to the shallower layer III (Fisher Fm) comprising stiff clay. At channels 2 and 3 the plastic deformation inside layer IV (Ling Bank Fm.) is 0.002 – 0.0025 dropping to only around 0.0012 inside layer IV (Fisher Fm.). The same sudden drop is observed at the southern edge of channel 1 (Figure 12 and Figure 13); strong plastic deformation of about 0.003 in layer I (Witch Ground Fm.) decreases to below 0.002 in layer II (Swatchway and Coal Pit Fm.). The described changes in plastic strain occur over layer boundaries between sediments of different stiffness, suggesting a dependence on the necessary yield stress.

In Figure 13, the vertical displacement is 100 times exaggerated to reveal fracture zone related surface deformation. A slight surface deformation related to the strong plastic deformation above channel 1 can be seen (black ellipses). The depression is about 0.2 cm deep (100 times exaggerated displacement) and the plastically deformed zone is located some ten meters south of the channel edge. At the end of the simulation the depression is about 1 cm deep. The surface deformation will continue to grow during continued unloading. The Hugin Fracture shows an elevation with a central depression on the order of 10 cm, and the Hugin Fracture is located up to 260 m south of the edge of an alluvial fan (Landschulze, Tveranger and Pedersen 2019).

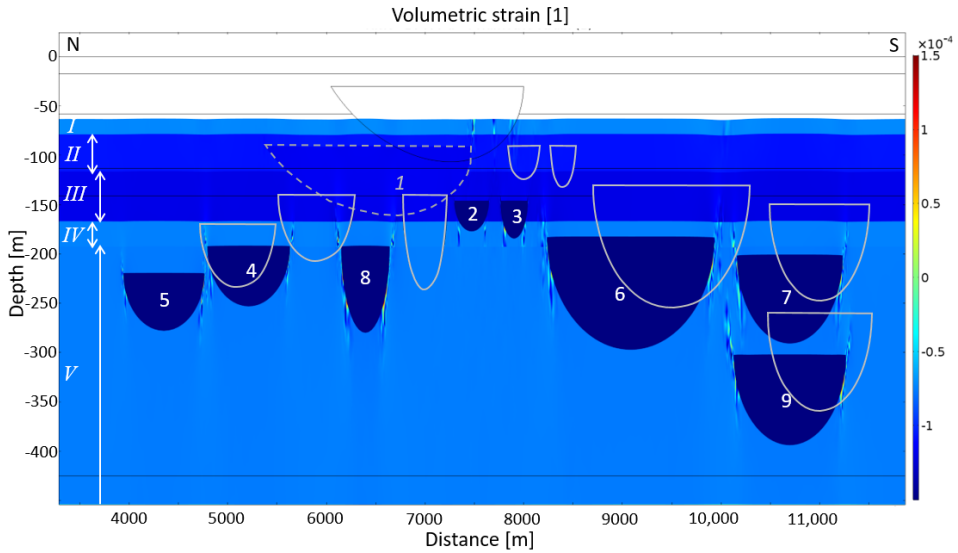


*Figure 14: Volumetric strain display with hot colours for dilation and cool colours for compaction. Original model geometry indicated by black lines; Arabic numerals indicate displaced channel locations and Roman numerals indicate displaced layers. Vertical displacement scale is 50 times exaggerated.*

The volumetric strain displays, equivalent to the effective plastic strain displays, are shown in Figure 14 to Figure 16. The overall volumetric strain is negative at 10.4 ka, reflecting elastic rebound due to decreasing ice load. The overview Figure 14 shows volumetric strain accumulation zones tangential to channel edges consistent with stress and plastic strain accumulations (figures 7-12). Dark blue coloured layers exhibit largest dilation representing elastic rebound after partial unloading. The sand-dominated layers show less dilation (blue, volumetric strain around 0.5) while channel 1 (sand-filled) shows about the same volumetric dilation of about -0.8 as the host layers consisting of stiff clay. Channels 2 through 8 experience strongly negative volumetric strain, channel 1 and the surrounding layers experience medium negative volumetric strain and the sandier layers I and IV (Witch Ground Fm. and Ling Bank Fm.) as well as the soft clay layer V (Aberdeen Ground Fm.) experience less strain. The strain pattern reflects more elastic rebound in the stiffer clay layers and channel fills, inflicting additional stress to the surrounding material. The areas of focussed stress and strain along the channel edges manifest in focussed strain areas, revealing in detail the



form of volumetric strain they experienced. Note that there are small areas of positive volumetric strain (compaction) inside predominantly negative strain (dilation) areas, best observed below channels 8 and 9 (southern edge) but also present below the southern edges of channels 6 and 7.

Figure 15 shows the same sudden drops in volumetric strain over layer boundaries as for the plastic strain. Note that the change appears also at the boundary between layers IV and V (see below channels 2 and 3 in Figure 15) which is less evident in the plastic deformation (Figure 12). Apart from the focussed strain area at channel 1, additional focussed strain areas are visible further to the south. The first one, located above the gap between channels 2 and 3, appears to be a superposition of stresses and associated strains from the same channels that are best distinguished in the shear stress display in Figure 10. Figure 12 shows plastic strain tangents from the channel edges throughout layer III while the volumetric strain display fails to highlight the subtle strain values with the chosen colour scale.

#### *Strain and deformation patterns and surface deformation*

The upper boundary of layer I displays subtle topography due to differential compaction and remaining ice load (e.g. Figure 12). The topography becomes increasingly pronounced during unloading (ice retreat). In the following, the strain and deformation patterns are described in more detail.

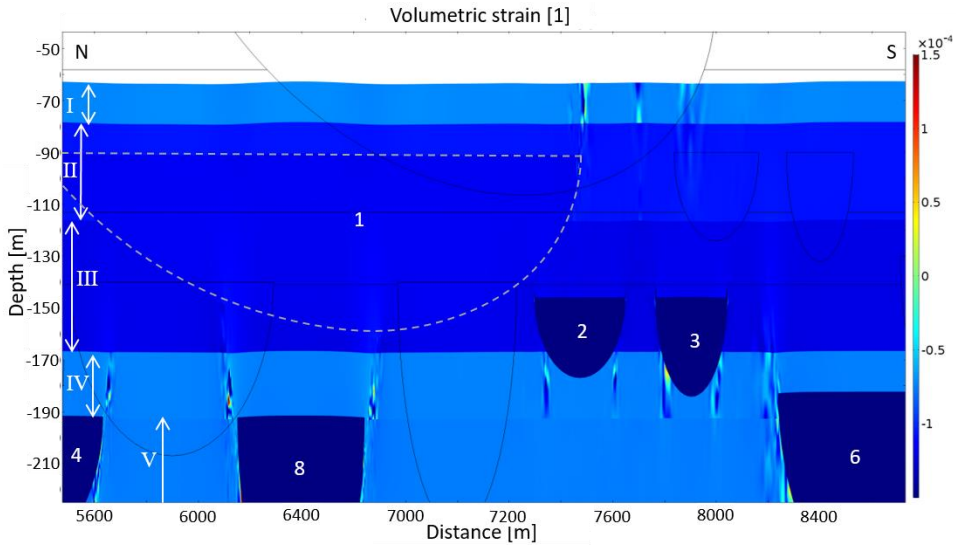
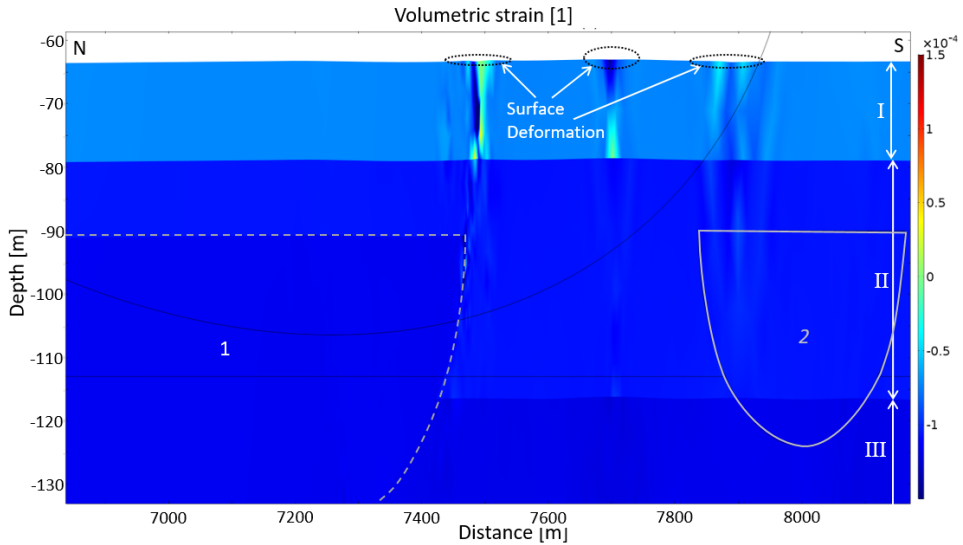


Figure 15: Details in volumetric strain around channel 1. Original model geometry indicated by black lines; Arabic and Roman numerals indicate displaced channels and layers, respectively. Vertical displacement scale is 50 times exaggerated. Note the small areas of dilation above channels 1, 8 and 4 and below channels 2 and 3. Material properties affect volumetric strain accumulation as is evidenced at layer boundaries above channels 8 and 4 and below channels 2 and 3.

A complex strain pattern is observed near the surface above channel 3 that cannot be easily linked to a single channel edge. In effective plastic strain and stress distribution the same complex pattern appears near the surface (see Figure 10 and Figure 12). It seems to represent a superposition of stresses and strains originating at channels 3, 6 and possibly 2 that is not easily recognised in either display.

A detailed look at the southern edge of channel 1 (Figure 16) shows strong negative volumetric strain amplitude, representing dilation, in the top layer (Witch Ground Fm.) accompanied by slightly positive amplitude, representing compaction. In the deeper layer II (Swatchway and Coal Pit Fm.) the amplitude decreases but the pattern of negative and positive values continues. The depression in surface deformation above the edge of channel 1 coincides with the strongly negative volumetric strain amplitude and the neighbouring elevations with the positive amplitude values. Applied to the Hugin Fracture the model results suggest that the elevated seafloor is associated with

compaction of the underlying sediments while the depression is associated with dilation, hence fracture opening.



*Figure 16: Enlarged area around the channel 1 fracture (Hugin Fracture). Both dilational and compressional volumetric strain is present in vertical elongated zones, suggesting the opening of a fracture. Original model geometry indicated by black lines, except for channel 2. Arabic and Roman numerals indicate displaced channels and layers; vertical displacement is 100 times exaggerated.*

The volumetric strain accumulation near the surface above channels 2 and 3 shows another pattern; it resembles an hourglass shape with negative values (relaxation/volume expansion) in the upper part and positive values (volume decrease/compaction) in the lower part. Some very subtle surface deformation seems to be associated with the hour-glass shaped and the southernmost strain accumulation. The expected deformation should be on the order of some ten centimetres. The sub-bottom profiler data acquired for studying the Hugin Fracture covers only a very local area around the seafloor fracture and the analysis was focussed on fracture indications (Landschulze, Tveranger and Pedersen 2019). More widespread high-resolution backscatter data (HISAS) are available and might reveal additional subtle seafloor topography.

The vertical displacement field is presented in Figure 17 and shows a general decrease in vertical displacement from around 120 cm at the surface to around 50 cm at the bottom of the figure. Given the vertical no-displacement roller boundary this decrease in vertical displacement is to be expected. It also reflects the increasing strength of the deeper rocks in contrast to the little consolidated shallow sediments. The upper model boundary shows slight topography, and, in some places, the tangential focus areas can be perceived as slightly elevated vertical displacement values, e.g. Figure 17 between the contours of channels 4 and 8.

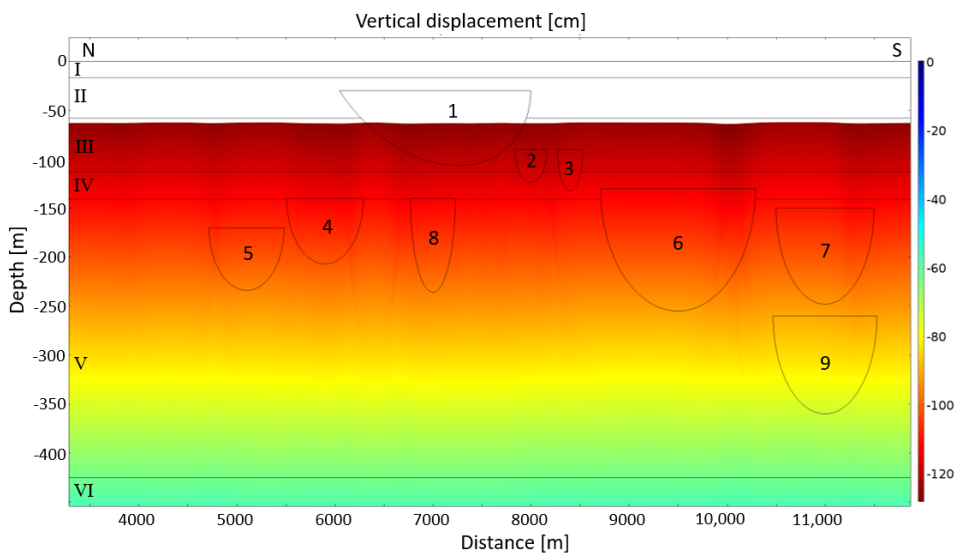


Figure 17: Vertical displacement at 10,400 years simulation time after loading with a 0.8 MPa top load and following unloading by 32 kPa at a rate of 0.08 MPa/ka. Notice the subtle surface topography due to differential compaction and slight differences in displacement due to heterogeneities (channels). Original geometry is indicated by black lines and Arabic numerals. Vertical displacement display is 50 times exaggerated, colour scale shows true displacement values in cm.

## Discussion

The motivation for the presented model and simulation results was to test and falsify the hypothesis of fracture formation for the Hugin Fracture as proposed by Landschulze, Tveranger and Pedersen (2019). However, the presented simulation results are robust and stable in a  $\pm 15\%$  range around the end member and layer values

---

presented in appendix C. As such, the model results support the hypothesis of the Hugin Fracture being a compaction fracture, but it does not prove this hypothesis to be true. Acquisition of geomechanical data from the Hugin Fracture are needed to confirm and constrain model parameters. The influence of channel geometry on the stress pattern should also be investigated and could shed light on the lateral changes of the surface appearance of the Hugin Fracture (Landschulze, Tveranger and Pedersen 2019).

The symmetric channels in the model produce symmetric zones of deformation and strain, tangential to the channel edges. At channel 1, however, only the steep southern wall develops a deformation zone to the surface, the gentler northern wall shows no sign of stress accumulation and, correspondingly, no strain or deformation. Differences in host layer properties only impact the amplitude of the accumulated stress, not the geometry (compare channels 2 and 3 to channels below in Figure 9). The same is true for the channel thickness, as stresses at channels 2 and 3 inside layer IV (Ling Bank Fm.) are below 400 MPa. Properties of channel fill do not change the geometry for stress accumulation zones as seen from the southern edge of channel 1 (sand-filled) that is similar to the other clay-filled channels. However, the gentle wedge-shaped northern edge of channel 1 seems to prevent stress accumulation. From this, we conclude that steepness of the channel walls as well as symmetry play an important role in the formation and location of stress accumulation zones.

The high-resolution backscatter and sub-bottom profiler data acquired at the Hugin Fracture cover only a very local area at and around the Hugin Fracture. More specifically, the northern edge of the interpreted alluvial fan (Landschulze, Tveranger and Pedersen 2019) is located beyond the data coverage of the sub-bottom profiler data and the 10 cm x 10 cm HISAS seafloor mosaic. On the part of the 33 cm x 33 cm seafloor mosaic (HISAS), no fracture indications like the Hugin Fracture were observed. In Landschulze, Tveranger and Pedersen (2019) the alluvial fan is interpreted slightly asymmetrical with a steep wall at the Hugin Fracture location and gentler slope towards the northern border (see solid blue line on figure 1). Therefore, less stress and hence deformation is expected to have taken place over the northern part of the alluvial fan, most likely not enough to produce any critical strain. The present paper applies a

slightly different geometry, where the northern wall is even gentler than the result from seismic interpretation. This choice is motivated by the idea to test the effect of the wall slope, and the presented results indicate that a steep channel wall has a major influence. As argued above, a symmetric sand body results in symmetric strain accumulation and, in the case of the Hugin Fracture, an additional fracture above and north of the northern edge of the alluvial fan. Unfortunately, time did not allow for additional geometries to be tested. Further investigation of the effect of wall steepness on strain accumulation and fracturing will be necessary.

Grollimund and Zoback (2000) employed step-load functions in their simulations after applying a pre-consolidation phase of about one million years. With a focus on large-scale (300 km) lithospheric response to thick (>200 m) ice shields this seems a reasonable solution. They also chose to ignore the poorly consolidated top 1000 m North Sea sediments. Our study concerns smaller scale deformation, namely the response of heterogeneous sediments; hence, we assume a pre-consolidated model and use a ramp load function to avoid numerical problems and account for a glacier slope. The ramp load function grows upwards rather than lateral; this may be counter-intuitive to modern glacial movement in rapid ice flows. There are two reasons for this approach, the first being the idea of permafrost conditions prior to glacier growth supporting a gradual load increase over a larger area, rather than the lateral advance of a glacier (load) front. The second reason lies in the fact that strain is accumulated in areas of high shear stress, i.e. the glacier front, rather than under isotropic load such as below a thick ice-sheet. The geographic area of the Viking Graben and Utsira High is still under investigation as to the ice conditions that prevailed during the Quaternary glaciations (e.g. Graham *et al.* 2011). Ice evolution, thickness, movement and base-conditions are not yet fully understood, but we argue that our approach is viable, at least due to the shear stress conditions required for strain accumulation and, ultimately, fracture development.

The maximum ice load in the simulation corresponds to a little over 80 m ice, assuming a density of  $0.931\text{kg/m}^3$ . Considering the absence of horizontal stress in the model this should be understood as a minimum ice thickness. For a simple isotropic case, the

weight of the sediment column above a given point subsurface results in a vertical stress and a horizontal stress of half the vertical stress. The horizontal stress increases with depth, counteracting additional vertical load (ice), and would allow for larger load before plastic deformation occurs. In addition, our assumption of present day compaction, i.e. stiff clays as a result of earlier glacial override or deposition, might lead to an underestimation of the actual ice load or load duration needed to compact soft clay to its stiff and brittle configuration that eventually facilitates fractures. We did also not account for glacial erosion and sedimentation that might alter the local stress field.

Sejrup, Hafliðason and Aarseth (1994) found an over 10 m thick over-consolidated till with low water content (around 30%) and a carbon-age of about 32,750 years before present in a depth below 4.5 m in the B2001 Sleipner core. Peacock (1995) proved drastic palaeo-environmental changes in the Viking Bank area spanning from glaciomarine to shallow marine and periodical dry land at the Viking Bank. Local stress variations due to (glaci)-fluvial erosion and sediment accumulations (fluvial fan) may contribute to local failure but the dominating cause remains focussed strain accumulation due to differential compaction.

Boulton, Caban and Hulton (1999) discuss various subglacial failure geometries down to 150 m subsurface to a Scandinavian ice sheet and how they change with rock properties (sand vs. granite). They also discuss the effect of a permafrost shield in front of the glacier on failure such as shear failure and hydraulic fracturing. Shear failure is suggested to occur in depths of at least 100-200 m, in unlithified rocks they may occur to depths in excess of 1000 m. Considering the generally poorly lithified rocks in the North Sea Basin (about 900 m thick), their work suggests that shear fracturing can take place in the entire interval. If this is the case, the shear fractures should be on a scale below present seismic data resolution. Boulton *et al.* (1999) find also that hydraulic fracturing is restricted to depths of up to 150 m with vertical fractures occurring at shallow depths (1-10 m), low angle up-glacier dipping subglacial fractures in intermediate depth, and horizontal fractures in the ice marginal zone at 150 m. The vertical hydraulic fractures can be filled with injected rock masses, sand or till in their

examples, according to the potential gradient and layering (Boulton *et al.* 1999). For our study, this could mean that the Hugin Fracture might be a hydraulic fracture, in a till layer, where sandier (more permeable) sediment from the top layer has been injected (see also Figure 13 and Figure 16). As there are no samples from the sediments in the Hugin Fracture this is mere speculation. Our simulations include plastic and elastic deformation of porous unconsolidated rocks (soil) with highly heterogeneous geometry, whereas simulations by Boulton *et al.* (1999) focus on elastic lithosphere with sand and intact granite, respectively, homogeneously distributed on complicated basin topography. Another difference is that our simulation is restricted to undrained conditions for the chosen physics model in the simulation software, whereas the study from Boulton *et al.* (1999) deals with glacier-induced water flow and represents an essentially drained model.

The parameters employed in our model have varying degrees of uncertainty, because there were no local geomechanical measurements available for our study. Instead we employed literature values for several parameters such as the Young's modulus  $E$ , the cohesion, the angle of internal friction, the Biot-Willis coefficient, porosity and permeability (Hamilton 1971, Sejrup *et al.* 1987, Koliji 2013, Bolton, Maltman and Fisher 2000, see appendix C for details). The model values of these parameters were determined from sediment description in a drilling site survey report from well 16/4-7, based on end member values for pure sand and pure clay (Fugro Survey AS 2012, see appendix B for details). For an easier handling in simulation design, we introduced a mixing constant  $k$  with a distinct value for each layer (see model description in the method section). Equation 18 describes how the mixing constant was applied to derive each layer's parameter. The mixing value allows for easily adjustment of the geotechnical parameters for each layer by adjusting a single value,  $k_{\text{layer}}$ . The presented results are robust in a range of  $\pm 15\%$  of the layers'  $k$ -value, i.e. the model did not have to be fine-tuned to produce the results. A variation of a layer's  $k$ -value is equivalent to a joint variation of the respective layers geomechanical parameters. We argue that this is a better approach in our case of uncertain and interdependent geomechanical properties than the usual change of a single parameter at a time (Ferretti, Saltelli and



---

Tarantola 2016). The results obtained with layer parameters in a  $\pm 15\%$  range of the figures presented in appendix C were all similar. In all cases, similar stress patterns with focus areas tangential to channel edges formed and a stress drop occurred at some point during the simulation run (see Figure 7). However, the stress and deformation pattern did vary slightly in magnitude and angle, as well as the time when the stress drop would occur.

We did, however, notice that small changes in the end member values for both the cohesion and the angle of internal friction did affect the simulation results and the strength of the pattern. There are relatively few published studies of these closely interrelated parameters and they include large variations (e.g. Mondol *et al.* 2007, Marcussen *et al.* 2009, Hampton 2002). Changing end member values for the Young's moduli  $E$  also has an effect, but this parameter has less variation in literature and seems to be better constrained. The Poisson ratio shows only minor effects for realistic values close to 0.5 for the presented model of fully saturated sediments. The remaining parameters showed negligible effects for small changes in end member values.

The simulation results show surface deformation similar to and on the same magnitude as the observed centimetre-scale seafloor elevations at the Hugin Fracture location (Pedersen *et al.* 2019). High-resolution sonar data from an AUV show a similar pattern of micro-bathymetry of the same magnitude at the Hugin Fracture as predicted by the model (see Figure 13 and 15). In addition, the simulation results predict gentle surface deformation above channel 8, that could be confirmed by high-resolution backscatter sonar data. Unfortunately, the acquired backscatter data do not cover the area above channel 8. Nevertheless, the good agreement between the modelled elevation caused by differential compaction and the actual elevation in the micro-bathymetry strengthens the model results.

Based on the modelling and the assessed parameter variability, it is unlikely that the Hugin Fracture is a unique feature. The simulation results show that a complex pattern of focused strain accumulation is produced by this simplified model. The simulation results are robust over a range of realistic parameter combinations and for a realistic

ice load. In other words, the simulation predicts that fractures like the Hugin Fracture should occur rather widespread and have previously not been discovered.

A reason for this is the small area with high-resolution data coverage of the seafloor. Only the extremely high resolution of the HISAS tool revealed the Hugin Fracture at the seafloor. The fracture signal is confirmed on subbottom profiler sections but could have been missed due to different survey design and larger line spacing. The HISAS data was crucial in the discovery of the Hugin Fracture and the subsequent subbottom profiler survey design and data interpretation. With more areas to be investigated by high-resolution synthetic aperture sonar (HISAS), it seems very likely that similar fractures will be found in the future.

### **Conclusion**

Shallow horizontally layered, isotropic sediments subjected to ice sheet load develop isotropic stress and strain distributions according to the respective layer properties. Heterogeneities such as channels/tunnel valleys introduce disturbances in the developing stress field. Channelized Pleistocene sediments, that are rampant in the Central North Sea, experience differential compaction when subjected to ice load from glaciers according to the presented poro-elastoplastic simulations. The induced shear stress shows focussed zones of stress accumulation and equivalent strain build-up tangential to channel edges. Symmetric zones of high strain develop at steep walls of symmetric channels irrespective of sediment fill properties, if they differ from the host layer properties. Heterogeneities to a depth of about 200 m are shown to develop strong deformation accumulations along tangential channel edge areas, suggesting that even thin ice sheets (<100 m), given favourable geometry, may induce fractures in surprisingly large depths.

The vast bulk of stress and strain accumulates during glacier retreat and beginning sediment rebound, resulting in fractures along some of the focus zones, e.g. above the shallowest sand-filled channel. The simulation could reproduce a strain pattern interpreted to resemble fracture opening connected to the edge of this channel with associated surface deformation similar to the Hugin Fracture. Hence, the formation

---

hypothesis for the Hugin Fracture (Landschulze, Tveranger and Pedersen 2019, Pedersen *et al.* 2019), being a compaction fracture, is supported by the simulation results. Application of standard literature values indicate that similar fractures should be expected at other places with favourable geometry. The influence of the geometry on the simulation results, as well as the geomechanical parameters, should be further investigated.

### **Acknowledgement**

We thank Jan Erik Lie and colleagues at Lundin Norway AS for generously providing drilling site surveys and permission to employ and cite the content. The work was funded by the Norwegian SUCCESS Centre and, partly, by the European project ECO<sub>2</sub>.

## References

- Aber, J.S. 1982. Model for glaciotectonism. *Bulletin of the Geological Society of Denmark*, 30, 79–90.
- Amestoy, P.R., Duff, I.S., L'Excellent, J.-Y. and Koster, J. 2001. MUMPS: A General Purpose Distributed Memory Sparse Solver. *IN: T. Sorevik, F. Manne, A. H. Gebremedhin, and R. Moe (eds.) Applied Parallel Computing. New Paradigms for HPC in Industry and Academia: 5th International Workshop, PARA 2000 Bergen, Norway, June 18–20, 2000 Proceedings*. Berlin, Heidelberg: Springer Berlin Heidelberg, pp. 121–130.
- Barrio, M., Stewart, H.A., Akhurst, M., Aagaard, P., Alcalde, J. and Bauer, A. 2015. GlaciStore: Understanding Late Cenozoic Glaciation and Basin Processes for the Development of Secure Large Scale Offshore CO<sub>2</sub> Storage (North Sea). *IN: 8th Trondheim Conference on CO<sub>2</sub> Capture, Transport and Storage, Trondheim, Norway, 16-18 June 2015*. Trondheim, pp. 1–2.
- Biot, M.A. 1941. General theory of three-dimensional consolidation. *Journal of Applied Physics*, 12(2), 155–164.
- Bjørlykke, K. 2006. Effects of compaction processes on stresses, faults, and fluid flow in sedimentary basins: examples from the Norwegian margin. *Geological Society, London, Special Publications*, 253(1), 359–379.
- Bolton, A.J., Maltman, A.J. and Fisher, Q. 2000. Anisotropic permeability and bimodal pore-size distributions of fine-grained marine sediments. *Marine and Petroleum Geology*, 17(6), 657–672.
- Boulton, G.S., Caban, P. and Hulton, N. 1999. *Simulations of the Scandinavian ice sheet and its subsurface conditions*. SKB Report
- Boulton, G.S. and Dobbie, K.E. 1993. Consolidation of sediments by glaciers: relations between sediment geotechnics, soft-bed glacier dynamics and subglacial ground-water flow. *Journal of Glaciology*, 39(131).
- Churcher, P.L. 1991. Rock Properties of Berea Sandstone, Baker Dolomite, and Indiana Limestone. *SPE International Symposium on Oilfield Chemistry*, 431–466.
- COMSOL Inc. 2016. *Comsol*. Available from: <https://www.comsol.com/comsol-multiphysics> [Accessed October 15, 2016].
- Dewhurst, D.N., Yang, Y. and Aplin, A. C. 1999. Permeability and fluid flow in natural mudstones. *Geological Society, London, Special Publications*, 158(1), 23–43.
- Ferretti, F., Saltelli, A. and Tarantola, S. 2016. Trends in sensitivity analysis practice in the last decade. *Science of The Total Environment*, 568, 666–670.
- Fugro Survey AS 2012. *Site survey at planned well location 16/4-X final, LN11302, PL544*. Lysaker, Norway.
- GCCSI 2015. *The global status of CCS 2015*. Available from: <https://www.globalccsinstitute.com/publications/global-status-ccs-2015-summary-report>.
- Graham, A.G.C., Stoker, M.S., Lonergan, L., Bradwell, T. and Stewart, M.A. 2011. The Pleistocene Glaciations of the North Sea Basin. *IN: J. Ehlers and P. Gibbard (eds.) Quaternary Glaciations - Extent and Chronology*. pp. 261–278.

- Grollmund, B. and Zoback, M.D. 2000. Post glacial lithospheric flexure and induced stresses and pore pressure changes in the northern North Sea. *Tectonophysics*, 327, 61–81.
- Haavik, K.E. and Landrø, M. 2014. Iceberg ploughmarks illuminated by shallow gas in the central North Sea. *Quaternary Science Reviews*, 103, 34–50.
- Hamilton, E.L. 1971. Elastic Properties of Marine Sediments. *Journal of Geophysical Research*, 76(2), 579-.
- Hampton, M.A. 2002. Gravitational failure of sea cliffs in weakly lithified sediment. *Environmental and Engineering Geoscience*, 8(3), 175–191.
- Ikari, M.J. and Kopf, A.J. 2011. Cohesive strength of clay-rich sediment. *Geophysical Research Letters*, 38(16), 1–5.
- Kanji, M.A. 2014. Critical issues in soft rocks. *Journal of Rock Mechanics and Geotechnical Engineering*, 6(3), 186–195.
- KeheW, A.E., Piotrowski, J.A. and Jørgensen, F. 2012. Tunnel valleys: Concepts and controversies — A review. *Earth-Science Reviews*, 113(1–2), 33–58.
- Koliji, A. 2013. *Soil friction angle*. Available from: <http://www.geotechdata.info/parameter/angle-of-friction.html> [Accessed July 16, 2016].
- Landschulze, K., Tveranger, J. and Pedersen, R.B. 2019. Seismic investigation of the Hugin Fracture, a seafloor fracture on the Utsira High, Central North Sea. *IN: Landschulze, K., Geophysical Investigation of the Hugin Fracture, a soft-sediment fracture on the Utsira High, North Sea*. PhD thesis, University of Bergen
- Lee, D., Cardiff, P., Bryant, E.C., Manchanda, R., Wang, H. and Sharma, M.M. 2015. A Fully 3-Dimensional Model for Hydraulic Fracture Growth in Unconsolidated Sands with Plasticity and Coupled Leak-off. *SPE Annual Technical Conference and Exhibition*.
- Lewis, H., Hall, S.A. and Couples, G.D. 2009. Geomechanical simulation to predict open subsurface fractures. *Geophysical Prospecting*, 57(2), 285–299.
- Li, Q., Ito, K., Wu, Z., Lowry, C.S. and Loheide II, S.P. 2009. COMSOL Multiphysics: A Novel Approach to Ground Water Modeling. *Ground Water*, 47(4), 480–487.
- Loneragan, L., Maidment, S.C.R. and Collier, J.S. 2006. Pleistocene subglacial tunnel valleys in the central North Sea basin: 3-D morphology and evolution. *Journal of Quaternary Science*, 21(8), 891–903.
- Løseth, H., Raulline, B. and Nygard, A. 2013. Late Cenozoic geological evolution of the northern North Sea: development of a Miocene unconformity reshaped by large-scale Pleistocene sand intrusion. *Journal of the Geological Society*, 170(1), 133–145.
- Marcussen, Ø., Bjørlykke, K., Jahren, J. and Faleide, J.I. 2009. *Compaction of siliceous sediments. Implications for basin modeling and seismic interpretation.*, PhD thesis, University of Bergen
- Mondol, N.H., Bjørlykke, K., Jahren, J. and Høeg, K. 2007. Experimental mechanical compaction of clay mineral aggregates-Changes in physical properties of mudstones during burial. *Marine and Petroleum Geology*, 24(5), 289–311.

- Nermoen, A., Korsnes, R.I., Christensen, H.F., Trads, N., Hiorth, A. and Madland, M.V. 2013. Measuring the Biot Stress Coefficient and Its Implications on the Effective Stress Estimate. *IN: ARMA*. San Francisco, CA, pp. 1–9.
- Nikolinakou, M.A., Luo, G., Hudec, M.R. and Flemings, P.B. 2012. Geomechanical modeling of stresses adjacent to salt bodies: Part 2—Poroelastoplasticity and coupled overpressures. *AAPG Bulletin*, 96(1), 65–85.
- Norsk Hydro AS 1990. *Final well Report 16/4-2 Licence 087 (Completion Report)*. Oslo, Norway. Available from: <http://factpages.npd.no/factpages/Default.aspx?culture=no>.
- Peacock, J.D. 1995. Late Devensian to early holocene palaeoenvironmental changes in the Viking Bank area, northern North Sea. *Quaternary Science Reviews*, 14(10), 1029–1042.
- Pedersen, R., Blomberg, A.E.A., Landschulze, K., Baumberger, T., Økland, I.E., Reigstad, L.J., Gracias, N., Mørkved, P.T., Thorseth, I.H., Stensland, A., Lilley, M.D. and Thorseth, I.H. 2013. Discovery of a 3 km long seafloor fracture system in the Central North Sea. *IN: Abstract #OS11E-03 presented at 2013 AGU Fall Meeting*. San Francisco, CA: AGU, p. Abstract #OS11E-03 presented at 2013 AGU Fall Meet.
- Pedersen, R., Landschulze, K., Blomberg, A.E.A., Gracias, N., Baumberger, T., Økland, I.E., Mørkved, P.T., Reigstad, L.J., Denny, A.R. and Thorseth, I.H. 2019. Discovery of seabed fluid flow along a 3 km long fracture in the Central North Sea. *IN: Landschulze, K., Geophysical Investigation of the Hugin Fracture, a soft-sediment seafloor fracture on the Utsira High, North Sea*. PhD thesis, University in Bergen.
- Pierrot, D. and Millero, F.J. 2000. The Apparent Molal Volume and Compressibility of Seawater Fit to the Pitzer Equations. *Journal of Solution Chemistry*, 29(8), 719–742.
- Sejrup, H., Aarseth, I., Ellingsen, K.L., Reither, E., Jansen, E., Løvlie, R., Bent, A., Brigham-Grette, J., Larsen, E. and Stoker, M. 1987. Quaternary stratigraphy of the Fladen area, central North Sea: a multidisciplinary study. *Journal of Quaternary Science*, 2(1), 35–58.
- Sejrup, H., Hafliðason, H. and Aarseth, I. 1994. Late Weichselian glaciation history of the northern North Sea. *Boreas*, 23(1991), 1–13.
- Sejrup, H., Larsen, E., Landvik, J., King, E.L., Hafliðason, H. and Nesje, A. 2000. Quaternary glaciations in southern Fennoscandia: evidence from southwestern Norway and the northern North Sea region. *Quaternary Science Reviews*, 19, 667–685.
- Sejrup, H.P., Aarseth, I. and Hafliðason, H. 1991. The Quaternary succession in the northern North Sea. *Marine Geology*, 101(1–4), 103–111.
- Sejrup, H.P., Aarseth, I., Hafliðason, H., Løvlie, R., Tien, Å.S.E.B.R.A., Tjøstheim, G., Forsberg, C.F. and Ellingsen, K.L. 1995. Quaternary of the Norwegian Channel: glaciation history and palaeoceanography. *Norsk Geologisk Tidsskrift*, 75, 64–87.
- Sejrup, H.P., Clark, C.D. and Hjelstuen, B.O. 2016. Rapid ice sheet retreat triggered by ice stream debuitressing: Evidence from the North Sea. *Geology*, 44(5), 355–358.
- Sharqawy, M.H., Lienhard, J.H. and Zubair, S.M. 2010. Thermophysical properties of seawater: a review of existing correlations and data. *Desalination and Water Treatment*, 16(1–3), 354–380.
- Tang, T., Hededal, O. and Cardiff, P. 2015. On finite volume method implementation of poro-elastoplasticity soil model. *International Journal for Numerical and Analytical Methods in Geomechanics*, 39(13), 1410–1430.

---

Terzaghi, K. 1943. *Theoretical Soil Mechanics*. Wiley.

Wang, H.F. 2000. *Theory of linear poroelasticity - with application to geomechanics and hydrogeology*. Princeton and Oxford: Princeton University Press.

Williams, J.P. and Aurora, R.P. 1982. Case Study of an Integrated Geophysical and Geotechnical Site Investigation Program for a North Sea Platform. IN: *Offshore Technology Conference. Offshore Technology Conference*.

Wood, D.M. 1990. *Soil behaviour and critical states soil mechanics*. Cambridge University Press, United Kingdom and New York.

## Appendix A

The mesh settings are summarized in table A1 and the resulting mesh statistics are listed in table A2.

<b>Mesh Settings</b>	
<b>Description</b>	<b>Value</b>
Maximum element size:	100
Minimum element size:	1
Curvature factor:	0.25
Maximum element growth rate:	1.15
Predefined size:	Extra fine
Custom element size:	Custom

*Table A1: Settings to specify the automatic meshing algorithm.*

<b>Resulting Mesh Statistics</b>	
<b>Description</b>	<b>Value</b>
Minimum element quality:	0.1457
Average element quality:	0.9399
Nr. of triangular elements:	36425
Nr. of edge elements:	4767
Nr. of vertex elements:	66

*Table A2: Mesh statistics for the simulation.*



## Appendix B

Landschulze, Tveranger and Pedersen (2019) employed industrial 3D seismic data for seismic interpretation of the Hugin Fracture. However, low resolution precluded detailed mapping of Quaternary layers in the top 500 m or so. Interpreted horizons and units are available from final well report for 16/4-2 accessible from the NPD fact pages (Norsk Hydro AS 1990). The quality and resolution of the 2D seismic lines is comparable to the 3D seismic used in Landschulze, Tveranger and Pedersen (2019) but significantly lower than modern high-resolution 2D seismic employed in recent drilling site surveys, e.g. prior drilling well 16/4-7 (Fugro Survey AS, 2012). A comparison with interpreted horizons from seismic drilling site survey for well 16/4-7, about 10 km to the southeast, showed minor differences (m-scale) in inferred layer thickness. Therefore, interpreted horizons for well 16/4-7 (Figure B-1) along with the description of the sediment content (Table B.1) were taken as a basis for model construction.

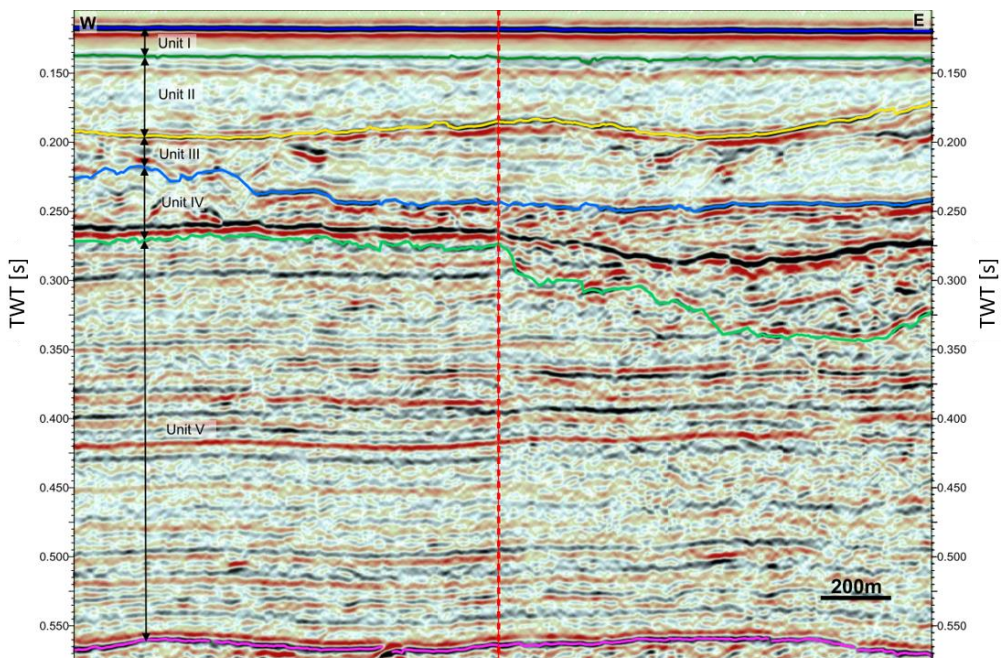


Figure B1: Interpreted Quaternary sequence on a 2D seismic line from drilling site survey report for well 16/4-7 (modified from figure 4.1 in the report (Fugro Survey AS, 2012). The units correspond to the layers in the geomechanical model and the thicknesses are taken from the designated drilling site (red stippled line). For a description of the units see table B.1.

<b>Layer definition</b>			
<b>Unit / Layer name</b>	<b>Formation name</b>	<b>Depth and modelled thickness (MSL)</b>	<b>Lithology (thickness at well position)</b>
Unit / Layer I	Witch Ground Fm.	118 m (17 m)	SAND, medium dense to very dense with possible thin layers of clayey gravel and soft, sandy clay.
Unit / Layer II	Swatchway and Coal Pit Fm.	135 m (41 m)	CLAY, stiff to very stiff, with pockets and thin layers of sand and silt.
Unit / Layer III	Fisher Fm.	176 m (55 m)	CLAY, stiff to very stiff, with sand interbeds expected down to 192 m $\pm$ 5 m (232 ms). Fine to medium, loose SAND from 192 m $\pm$ 5 m (232 ms) down to the base of the unit. Scattered boulders may occur.
Unit / Layer IV	Ling Bank Fm.	231 m (28 m)	SAND, fine to medium, loose with possible thin layers of soft clay. Boulders may occur throughout the unit with an enhanced probability within a $\sim$ 4 m thick interval starting at 209 m $\pm$ 6 m (251 ms).
Unit / Layer V	Aberdeen Ground Fm.	259 m (284 m)	CLAY, soft with shell fragments and thin layers of sandy clay. Thin sand layers may occur at 385 m $\pm$ 13 m (435 ms), 501 m $\pm$ 18 m (551 ms) and 505 m $\pm$ 18 m (555 ms). Scattered boulders may occur
Unit / Layer VI	Pliocene (undifferentiated)	Below 543 m	CLAYSTONE, soft becoming firm towards the base with thin layers of sandy clay.

*Table B1: Definition of units and layers modified from tables 4.4 and 4.5 in the drilling site survey report (Fugro Survey AS, 2012). Depths and thicknesses are taken from the well position for implementation in the model.*

## Appendix C

Simulation parameters and sediment properties used in the model are specified in the following tables. Unfortunately, there are no geotechnical measurements available through the Pleistocene unit in the Norwegian North Sea. The shallow overburden on the Norwegian Continental Shelf has not yet been investigated in large detail. Research sampling resulted mostly in cores of only a few meters below seafloor and petroleum industry has traditionally focussed only on reservoir rocks and the caprock immediately above. A number of wells penetrate the Quaternary and well logs, typically resistivity and gamma-ray, are available, that can at least give some indication of the sand or clay content along the well path. The interpretation of a sandy alluvial fan was based on resistivity and gamma-ray logs from well 16/4-2 (see Landschulze, Tveranger and Pedersen 2019). Lacking precise values from measurements, the model parameters were chosen from literature. Poisson ratio, porosities and (grain) densities are taken from (Hamilton 1971); Young's modulus has been derived from bulk and shear modulus in the same source employing following relationship:

$$E = \frac{9 \cdot \kappa \cdot G}{3 \cdot \kappa + G} \quad (\text{A-1})$$

Ikari and Kopf (2011) studied the influence of cohesion on clay-rich sediments with laboratory experiments. They found cohesion values in the range 9-70 kPa for clay-rich unsheared, i.e. nearly uncompacted, sediments and in the range 15-133 kPa for clay-rich sheared (compacted by 0.9-2 MPa shear force) clays, while (Sejrup and Aarseth 1987) reports a shear strength of 200 MPa for the shallow till unit in B2001, near the Hugin Fracture. We therefore assume a value of 200 MPa for pure stiff clay in our model and assign a small, apparent cohesion to pure sand to avoid numerical instability.

The angle of internal friction is taken from a website for geotechnical information (Koliji 2013). Permeability values are taken from (Bolton *et al.* 2000) and values for dynamic viscosity and compressibility of water are taken from Stanley and Button in (Sharqawy, Lienhard and Zubair 2010, Pierrot and Millero 2000) respectively. Ice thickness is based on values from Boulton and Dobbie (1993) who inferred ice sheet

thickness from over-consolidation measurements in tills and clays in the Netherlands and adjacent North Sea. Values for the Biot-Willis coefficient have been assigned in accordance with non-linear relationships between the coefficient and porosity (Wang 2000). Tests with different values for the Biot-Willis coefficient showed negligible impact on simulation results, this is in agreement with a discussion in Nerموen *et al.* (2013). Table C1 lists the parameters used in the layered background model and Tables C2 and C3 lists the applied parameters for channel 1 and 2-9, respectively.

Following pages:

*Table C1: Parameters for the presented simulation. Layer VI (Pliocene) is not explicitly defined - only incorporated through the background cohesion function of 7kPa/m.*

<b>Parameters</b>			
<b>Name</b>	<b>Expression</b>	<b>Value</b>	<b>Description</b>
load	0.8 [MPa]	8E5 Pa	Ice load (total)
load_time	10 [ka]	10000 a	Time to total load
load_rate	load / load_time	80 Pa/a	Growth/Decay rate
defscale	50	50	Displacement scaling
c_main	19 [kPa]	19000 Pa	Start value cohesion at surface
dc_main	7 [kPa/m]	7000 N/m <sup>3</sup>	Increase in cohesion with depth
k_WG	0.1	0.1	k-value Witch Ground Fm
k_SCP	0.7	0.7	k-value Swatchway & Coal Pit Fm
k_F	0.8	0.8	k-value Fisher Fm
k_LB	0.15	0.15	k-value Ling Bank Fm
k_AG	0.2	0.2	k-value Aberdeen Ground Fm
E_clay	0.39 [GPa]	3.9E8 Pa	Young's modulus clay
E_sand	1 [GPa]	1E9 Pa	Young's modulus sand
E_WG	$E_{sand} + (E_{clay} - E_{sand}) \cdot k_{WG}$	9.39E8 Pa	
E_SCP	$E_{sand} + (E_{clay} - E_{sand}) \cdot k_{SCP}$	5.73E8 Pa	
E_F	$E_{sand} + (E_{clay} - E_{sand}) \cdot k_F$	5.12E8 Pa	
E_LB	$E_{sand} + (E_{clay} - E_{sand}) \cdot k_{LB}$	9.085E8 Pa	
E_AG	$E_{sand} + (E_{clay} - E_{sand}) \cdot k_{AG}$	8.78E8 Pa	
c_clay	292 [kPa]	2.92E5 Pa	Cohesion clay
c_sand	100 [kPa]	1E5 Pa	Apparent cohesion sand
c_WG	$c_{sand} + (c_{clay} - c_{sand}) \cdot k_{WG}$	1.192E5 Pa	
c_SCP	$c_{sand} + (c_{clay} - c_{sand}) \cdot k_{SCP}$	2.344E5 Pa	
c_F	$c_{sand} + (c_{clay} - c_{sand}) \cdot k_F$	2.536E5 Pa	
c_LB	$c_{sand} + (c_{clay} - c_{sand}) \cdot k_{LB}$	1.288E5 Pa	

c_AG	$c_{sand} + (c_{clay} - c_{sand}) \cdot k_{AG}$	1.384E5 Pa	
aif_clay	22 [deg]	0.38397 rad	angle of internal friction clay
aif_sand	66 [deg]	1.1519 rad	angle of internal friction sand
aif_WG	$aif_{sand} + (aif_{clay} - aif_{sand}) \cdot k_{WG}$	1.0751 rad	
aif_SCP	$aif_{sand} + (aif_{clay} - aif_{sand}) \cdot k_{SCP}$	0.61436 rad	
aif_F	$aif_{sand} + (aif_{clay} - aif_{sand}) \cdot k_F$	0.53756 rad	
aif_LB	$aif_{sand} + (aif_{clay} - aif_{sand}) \cdot k_{LB}$	1.0367 rad	
aif_AG	$aif_{sand} + (aif_{clay} - aif_{sand}) \cdot k_{AG}$	0.99833 rad	
alphaB_clay	0.8	0.5	Biot-Willis coefficient clay
alphaB_sand	0.45	0.05	Biot-Willis coefficient sand
alphaB_WG	$\alpha_{sand} + (\alpha_{clay} - \alpha_{sand}) \cdot k_{WG}$	0.095	
alphaB_SCP	$\alpha_{sand} + (\alpha_{clay} - \alpha_{sand}) \cdot k_{SCP}$	0.365	
alphaB_F	$\alpha_{sand} + (\alpha_{clay} - \alpha_{sand}) \cdot k_F$	0.41	
alphaB_LB	$\alpha_{sand} + (\alpha_{clay} - \alpha_{sand}) \cdot k_{LB}$	0.1175	
alphaB_AG	$\alpha_{sand} + (\alpha_{clay} - \alpha_{sand}) \cdot k_{AG}$	0.14	
eps_clay	0.75	0.75	Porosity clay
eps_sand	0.4	0.4	Porosity sand
eps_WG	$eps_{sand} + (eps_{clay} - eps_{sand}) \cdot k_{WG}$	0.435	
eps_SCP	$eps_{sand} + (eps_{clay} - eps_{sand}) \cdot k_{SCP}$	0.645	
eps_F	$eps_{sand} + (eps_{clay} - eps_{sand}) \cdot k_F$	0.68	
eps_LB	$eps_{sand} + (eps_{clay} - eps_{sand}) \cdot k_{LB}$	0.4525	
eps_AG	$eps_{sand} + (eps_{clay} - eps_{sand}) \cdot k_{AG}$	0.47	
kap_clay	$11 \cdot 10^{-10} [\text{cm}^2]$	1.1E-13 m <sup>2</sup>	Permeability clay

kap_sand	$4 \cdot 10^{-9} [\text{cm}^2]$	$4\text{E}-13 \text{ m}^2$	Permeability sand
kap_WG	$kap_{sand} + (kap_{clay} - kap_{sand}) \cdot k_{WG}$	$3.71\text{E}-13 \text{ m}^2$	
kap_SCP	$kap_{sand} + (kap_{clay} - kap_{sand}) \cdot k_{SCP}$	$1.97\text{E}-13 \text{ m}^2$	
kap_F	$kap_{sand} + (kap_{clay} - kap_{sand}) \cdot k_F$	$1.68\text{E}-13 \text{ m}^2$	
kap_LB	$kap_{sand} + (kap_{clay} - kap_{sand}) \cdot k_{LB}$	$3.565\text{E}-13 \text{ m}^2$	
kap_AG	$kap_{sand} + (kap_{clay} - kap_{sand}) \cdot k_{AG}$	$3.42\text{E}-13 \text{ m}^2$	
fm_rho	$2650 [\text{kg}/\text{m}^3]$	$2650 \text{ kg}/\text{m}^3$	Formation density
fm_nu	0.48	0.48	Formation Poisson's ratio
fm_chif	$5.1 \cdot 10^{-10} [1/\text{Pa}]$	$5.1\text{E}-10 \text{ 1}/\text{Pa}$	Compressibility of fluid
fm_mu	$1.8 [\text{cP}]$	$0.0018 \text{ Pa} \cdot \text{s}$	Dynamic viscosity

Table C1: Parameters for the presented simulation. Layer VI (Pliocene) is not explicitly defined - only incorporated through the background cohesion function of  $7\text{kPa}/\text{m}$ .

Channel 1 Parameters		
Name	Value	Simulation Unit
Young's modulus	$835 [\text{MPa}]$	Pa
Poisson's ratio	0.47	1
Density	2650	$\text{kg}/\text{m}^3$
Dynamic viscosity	$1.8 [\text{cP}]$	$\text{Pa} \cdot \text{s}$
Compressibility of fluid	$5.1 \cdot 10^{-10}$	$1/\text{Pa}$
Biot-Willis coefficient	0.45	1
Porosity	0.4	1
Permeability	$4 \cdot 10^{-9} [\text{cm}^2]$	$\text{m}^2$
Initial yield stress	$200 [\text{kPa}]$	Pa

Table C2: Parameters for channel 1, representing a section through a narrow alluvial fan comprising coarse sand.

<b>Parameters Channels 2-9</b>		
<b>Name</b>	<b>Value</b>	<b>Simulation Unit</b>
Young's modulus	390 [MPa]	Pa
Poisson's ratio	0.48	1
Density	2650	kg/m <sup>3</sup>
Dynamic viscosity	1.8 [cP]	Pa·s
Compressibility of fluid	$5.1 \cdot 10^{-10}$	1/Pa
Biot-Willis coefficient	0.8	1
Porosity	0.75	1
Permeability	$10^{-10}$ [cm <sup>2</sup> ]	m <sup>2</sup>
Initial yield stress	200 [kPa]	Pa

*Table C3: Parameters for channels 2-9 comprising stiff clay, maybe till.*



### 3. Synthesis

The present thesis focuses on the Hugin Fracture and its formation. Our research provides a geological interpretation of the shallow subsurface of the North Sea sediments on the Utsira High, underlying the seafloor fracture. It also provides hypotheses on the formation mechanism and the results of a numerical model of one of them. In the following sections we synthesize and discuss the main findings of the present study and assess their implications for ice-load induced fracturing and subsurface fluid migration.

#### 3.1 Synthesis of main findings and key implications

Our main findings from the geophysical investigations and numerical modelling can be summarized in these points:

(1) The Hugin Fracture is at least 30 m deep and (2) positioned along the southern margin of what appears to be an up to 120 m thick, alluvial fan at a deeper stratigraphic level (about 40 m depth and below). The alluvial fan exhibits a sand-dominated high-porous fill and is surrounded by clay-dominated low-porosity host sediment that shows indications of differential compaction. (3) The Hugin Fracture was likely formed by differential compaction occurring along the margin of the alluvial fan, possibly enhanced by glacial loading. (4) The available data do not allow unequivocal conclusions to be drawn as to how the Hugin Fracture connects to underlying structures. Pleistocene channels or tunnel valleys are frequently observed throughout the 3D seismic dataset, they represent heterogeneities in a normally layered sediment sequence. (5) Along such heterogeneities ice-load induced differential stresses may lead to strong deformation accumulations in focused areas tangential to steep channel edges as shown in poroelastoplastic simulations. (6) Ice-load induced differential stress can lead to topography inversion above channel fills with different geomechanical properties than their surroundings, supported by simulation results and field observations. (7) An identified fault in the top Utsira Fm. below the Hugin Fracture

location seems not to be connected to the seafloor. (8) Based on our findings, the sealing capacity of the Pleistocene overburden above the Utsira Fm. is considered compromised at the Hugin Fracture location.

### 3.1.1 Nature of the Hugin Fracture

As described in paper I, the seafloor track of the Hugin Fracture comprises 1) segments where ring-shaped structures (pockmarks) with 5-10 m diameter link together in a continuous structure (Figure 7A); 2) segments of pockmarks defining a semi-linear row; 3) fracture features that sidestep and overlap (Figure 7C); 4) linear segments that branch and define a zigzag pattern (Figure 7B). Dark patches and dark linear segments show areas with lower backscatter values than their surroundings. The lower backscatter probably reflects different sediment properties or fluid saturation and appears to highlight areas with active seepage. In paper I, we report prominent fluid flow in areas 1 and 4, less in area 2, and no observable flow in area 3. A possible reason for the lack of fluid flow in the sidestepping fractures could be sealing-off of the fracture planes by clay.

In general, the uppermost 1000 m of sediment in the North Sea are considered to consist of soft sediment as they have not been buried deep enough to experience considerable consolidation or to be lithified (Bjørlykke and Hoeg 1997). Before the discovery of the Hugin Fracture, fractures or cracks of several kilometres' length have never been observed in soft sediments. Soft sediment deformation manifest in various forms, such as ring or pipe structures, folding, crack development and faulting and is often related to tectonic activity or seismicity (e.g. Vanneste *et al.* 1999, Wattrus *et al.* 2003). Usually, the scales of cracks and faults in soft sediments are in the range of millimetres and up to several tens of meters, the dimensions depend on sediment properties and magnitude of the driving force (Brodzikowski *et al.* 1987). Soft sediments are, in general, too weak to host large scale linear fractures. Consequently, the 3.5 km long Hugin Fracture should have formed due to a unique combination of sediment properties, local sediment variation and stress (load) history (Figure 10).

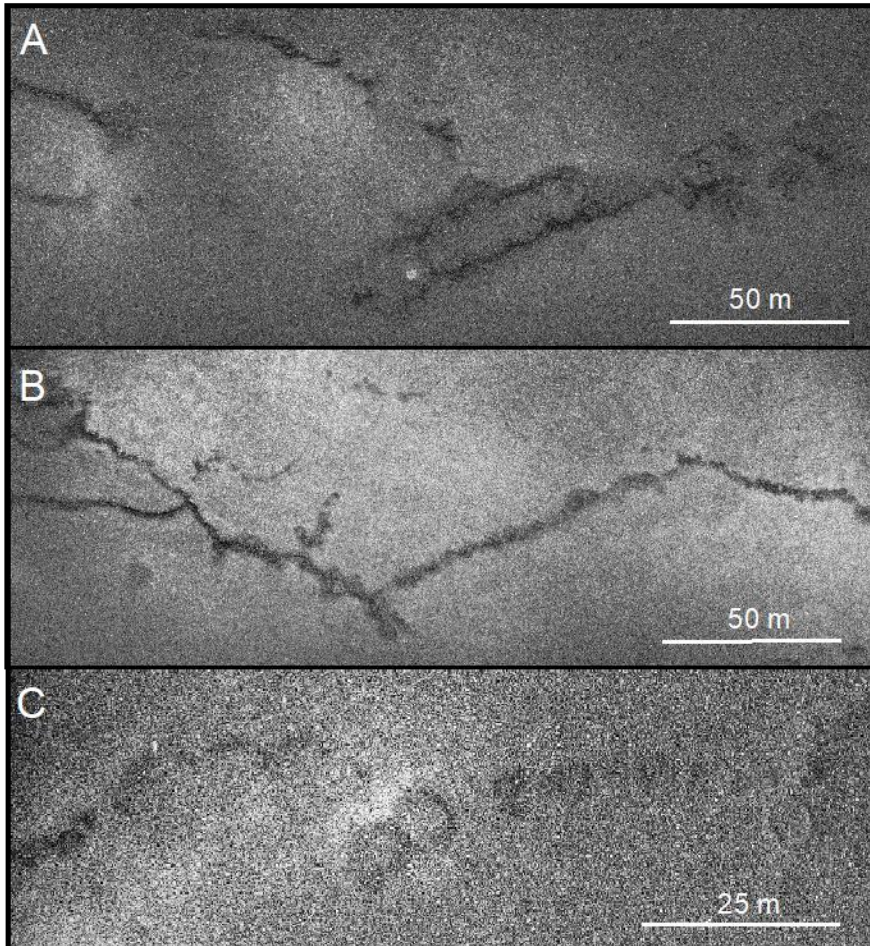


*Figure 7: Details along the seafloor track of the Hugin Fracture, locations indicated in Figure 4.*

In paper II we link the seafloor fracture to the southern margin of a buried alluvial fan, based on joint interpretation of high-resolution SBP data, conventional 3D seismic data, 2D seismic sections and well logs. The ring structures evident on the HISAS seafloor mosaic demonstrate that the seafloor comprises soft sediment, while the lateral variation of ring structures and lineation could indicate varying degree of compaction of sediments at the seafloor or below, resulting in local brittle fracturing (Figure 8). It could also indicate variations in subsurface sediment composition and associated variations in fluid pressure.

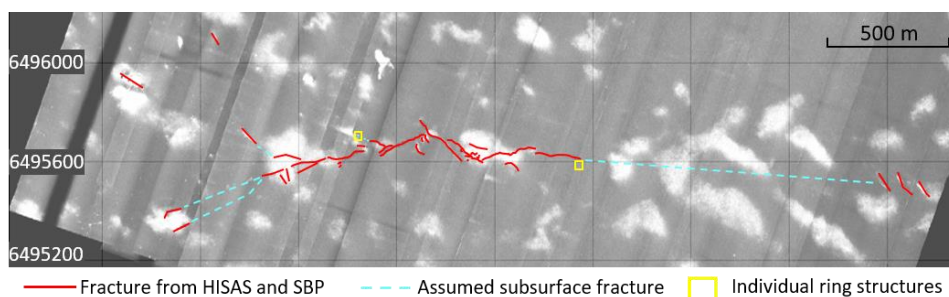


Figure 8: Interpretation of the seafloor track of the Hugin Fracture.

In her doctoral thesis, Cevatoglu (2015, p.182-185) provides a thorough interpretation of the lateral variation in layer displacement along the Hugin Fracture based on side-scan sonar, Chirp data and the same SBP data employed in this study (Figure 9 and Figure 9). She concludes that the seafloor track resembles a fault with an oblique slip in a transtensional stress regime and a present day E-W dominating stress regime in the study area, due to a combination of ice-load induced differential compaction and recent tectonics (Brudy and Kjørholt 2001, Grollimund *et al.* 2001). However, the cited studies rely on stress measurements from depths  $\geq 1500$  m, as shallower measurements are not available, and show that stresses are highly influenced by loading and unloading cycles during Quaternary glaciations (Grollimund and Zoback 2003). The top Pleistocene sediments are assumed viscoelastic, relaxing any differential stress once it is relieved. The simulation results presented in paper III predict, that while the Pleistocene layers relax, plastic deformation continues in high-strain areas. We suggest that the Hugin Fracture is formed due to ice-load induced high-strain deformation at an E-W oriented steep edge of an alluvial fan. This orientation favours fracture opening in an E-W dominating horizontal stress regime. Since the actual stress regime in the top 1000 m remains unverified by measurements, we find Cevatoglus suggestion to be reasonable with the presently available knowledge. The ring structures at the fracture tips and nearby areas could, thus, be indications of immaturity and continued growth of a fracture system (Wattrus *et al.* 2003).

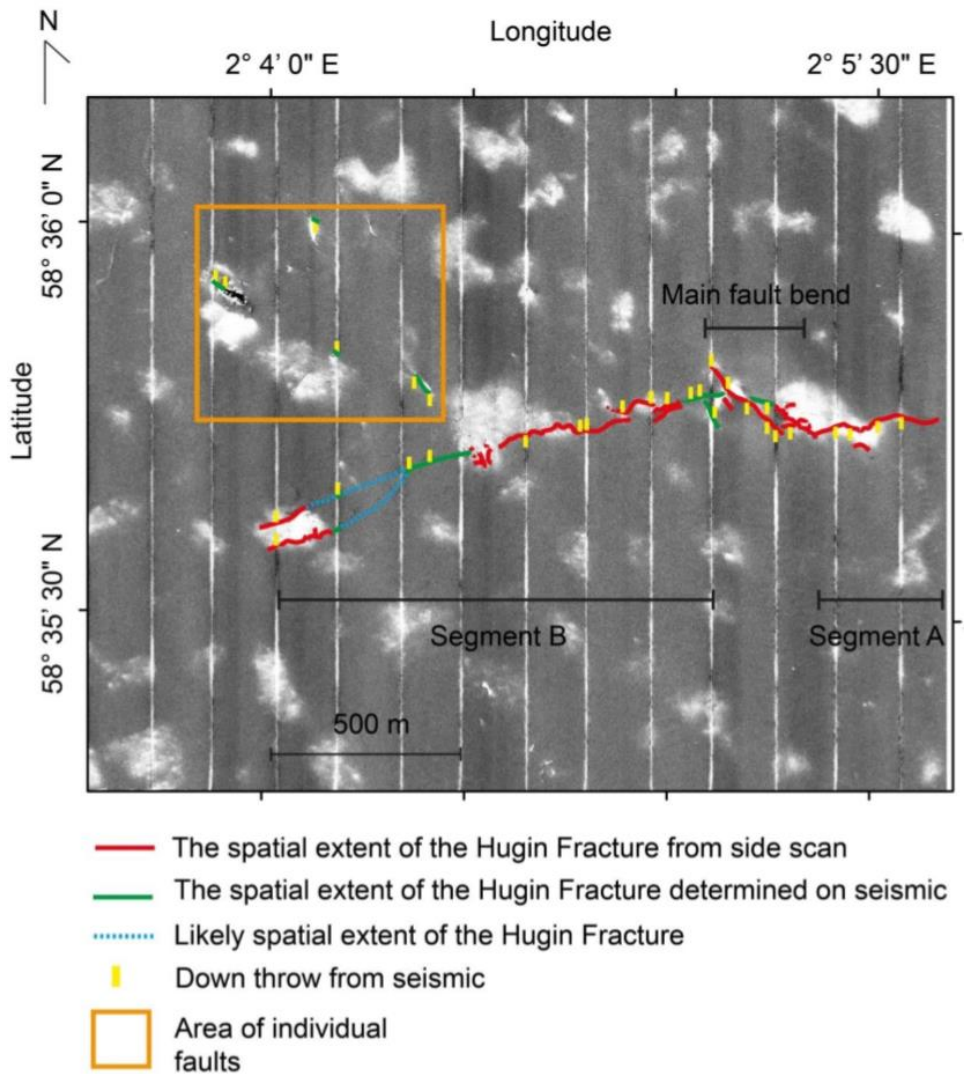


Figure 9: Partial interpretation of the central part of the Hugin Fracture as presented by Cevatoglu (2015).

An alternative explanation for holding the fracture open could be excess pore pressure caused by continued compaction of the sediments (Bjørlykke 2006). The pore pressure profile in well 16/4-2 was, however, recorded to be normal at the time of drilling, eliminating this hypothesis (Norsk Hydro AS 1990). Excess pore pressure inside the sandy alluvial fan might have contributed in opening the Hugin Fracture, but seems unlikely able to maintain an open fluid pathway, unless petroleum-related activity

keeps the pressure up (Cavanagh and Wildgust 2011, Verdon *et al.* 2013). The Hugin Fracture may also represent a hydraulic fracture with injected sand from the top sand layer, formed near the glacier toe according to a mechanism suggested by Boulton, Caban and Hulton (1999). This would also explain both the formation of the fracture and the present-day open fluid pathway along the injected sand.

### **3.1.2 Ice-load induced sediment deformation**

Paper III presents the poroelastoplastic simulation results. The vast bulk of stress and strain accumulates during glacier retreat and initial sediment rebound, resulting in fractures along some focused zones, e.g. above the shallowest sand-filled channel. The simulation could reproduce a strain pattern interpreted to resemble fracture opening connected to the edge of this channel with associated surface deformation. Field observations from the Hugin Fracture match the simulation results. The numerical model was populated with literature values for the necessary geomechanical parameters and sediment layers and the layer geometry was based on an interpreted 3D seismic section (paper I). No predefined areas for deformation accumulation or fracture formation were specified in the model, i.e. the stress and strain could develop freely for the given layer geometry. The simulation results were also found to be robust over a range of parameter values. Thus, the formation hypothesis for the Hugin Fracture in paper I, being a compaction fracture, is supported by the simulation results in paper III.

Al Hseinat and Hübscher (2014) present a conceptual model to explain an observed rejuvenating of pre-salt faults by ice load in the southwestern Baltic Sea. In their model the ice load leads to differential subsidence and the deposition of a till above the deep-rooted faults. Deglaciation and associated salt movement leads to topography inversion of subsurface layers and the renewed growth of faults at the edges of a till-filled tunnel valley. Similar faults have not yet been reported from the Norwegian North Sea, although salt tectonics has been the cause for faulting in Triassic and Cretaceous rocks (e.g. Jackson, Kane and Larsen 2010, Tvedt *et al.* 2013). A reason for this might be the larger burial depth of Cretaceous rocks below up to 1000 m thick Quaternary sediments. Aside from the fault in the lower seal above the Utsira Fm., no seismic faults

were discovered during this study (paper I). In particular, no seismic evidence of a fault connection to the Hugin Fracture was found.

Simulation studies on crustal stress changes due to glacial loading/unloading cycles in the North Sea show good agreement with well measurements at  $\geq 1500$  m depth (Grollmund and Zoback 2000, Grollmund *et al.* 2001, Grollmund and Zoback 2003). Our geomechanical model complements these earlier findings on a smaller scale and gives new insight in ice-load induced sediment deformation of the  $\sim 500$  m poorly consolidated glacially reworked sediments in the North Sea Basin. Our simulation of poroelastoplastic channelized sediments shows that ice load can induce high-strain deformation and fractures around channel heterogeneities (Figure 10). The induced shear stress appears in focused zones of stress accumulation and equivalent strain build-up tangential to steep edges of buried channels. The high strain zones develop at steep channel walls irrespective of sediment fill properties only if they differ from the host layer properties. Our simulation predicts that strong deformation accumulations develop at heterogeneities as deep as 200 m, suggesting that even thin ice sheets ( $< 100$  m) contribute to strain development at large depths (at least 400 m according to results shown in paper III).

In paper I, the age of the Hugin Fracture is considered to be  $\leq 29,000$  years which is around the time of the Last Glacial Maximum (LGM) and younger (Reinardy *et al.* 2017). There is some uncertainty as to the last time that the western Utsira High was covered by ice (see e.g. Bradwell *et al.* 2008, Graham *et al.* 2013, Sejrup *et al.* 2016). Grollmund and Zoback (2003) assume a 200 m-thick ice sheet in this area for their simulations of crustal stresses while our results in paper III indicate that less ice ( $< 100$  m) may have induced fracturing at the Hugin Fracture. Age constraints may be inferred from organic material like carbonate crusts. Microbial mats, such as those encountered at the fluid escape areas of the Hugin Fracture, often produce carbonate crusts as a product of methane-metabolization. Carbonate precipitation by microbial mats does occur under various conditions, in salt or fresh water, and is largely related to methane amounts and seepage rates, but also to water chemistry (Dupraz *et al.* 2009). At the investigated parts of the Hugin Fracture, however, no such carbonate crusts were found.

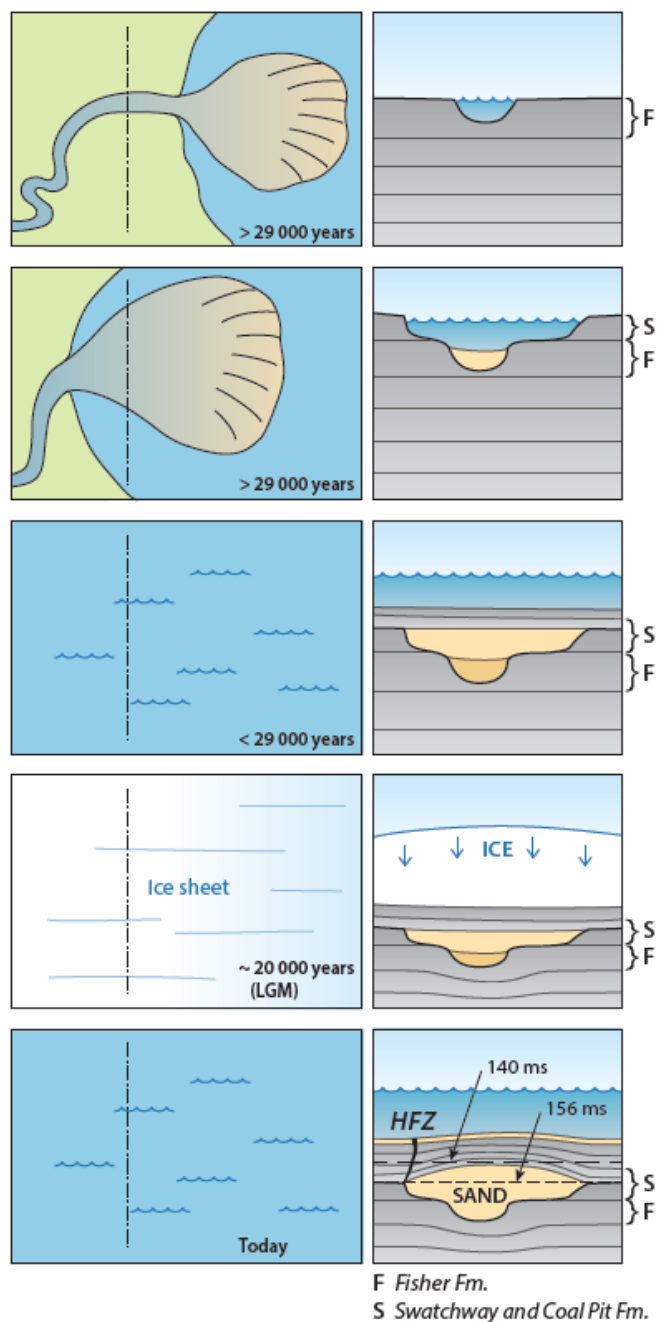


Figure 10: Geological model of ice-load induced Hugin Fracture formation.



This could indicate that the duration of hydrocarbon leakage has been too short for major carbonate crusts to develop or that the methane amounts were too small. Further investigations are necessary to determine the duration and onset of the fluid flow.

### 3.1.3 Implications for fluid migration

The buried channels or tunnel valleys likely have a composite layered fill according to earlier studies (Kristensen and Huuse 2012, Kehew *et al.* 2012). If they are connected by open compaction fractures like the Hugin Fracture they could form a complex network of vertical and lateral pathways for upwards fluid migration.

The development of the North Sea basin has been influenced by several glaciations and transgression cycles as presented by Graham *et al.* (2011), Reinardy *et al.* (2017) and others, implying that conditions for forming such fractures occurred several times during the middle-late Pleistocene. Additional compaction fractures at larger depths from earlier glaciation cycles should be expected according to simulation results presented in paper III. If connected horizontally, for example through high-porous layers in channel or tunnel valley fill, these fracture systems could act as pathways for fluid and gas migration from older formations. A fractured and channelized overburden could explain the absence of gas-rich bright spots in the Pliocene sediments just below the Hugin Fracture (central part of the Pliocene unit in Figure 11).

Buried differential compaction fractures at larger depths will likely be closed because of larger principal stresses at depth. However, if present, a change in the local stress regime, as it would occur during wastewater or CO<sub>2</sub>-injection up to some hundred km away, could reopen the fractures and reinstate a vertical-lateral fluid migration pathway as outlined before. Open compaction fractures could thus be included in the range of different fluid migration pathways in the North Sea (Mazzini *et al.* 2003, Karstens and Berndt 2015, Cartwright and Santamarina 2015). They should be of special interest to CO<sub>2</sub>-storage projects in extensional stress regimes (Rutqvist, Birkholzer and Tsang 2008, Tsang, Birkholzer and Rutqvist 2007).

The fluid escape rate at the Hugin Fracture has been reported to be approximately 50 cm/a and the expelled water is of meteoric origin, possibly meltwater, with a low

content of dissolved gas (Häckel *et al.* 2013). Most of the dissolved hydrocarbons are of biogenic origin (< 500 m depth), but low amounts of higher alkanes indicate some deeper source for a minor part of the dissolved fluids (Pedersen *et al.* 2019, Häckel *et al.* 2013, Lichtschlag *et al.* 2018).

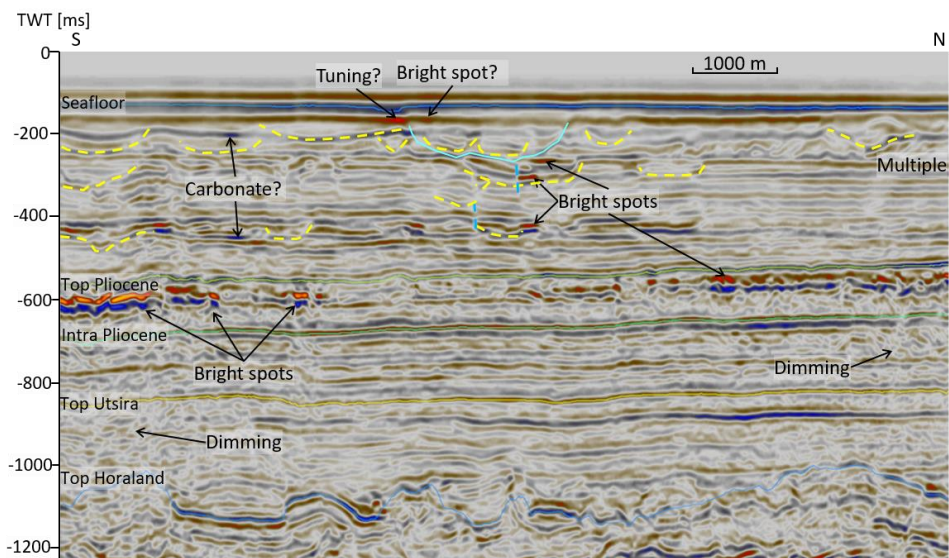


Figure 11: Interpreted 3D seismic section. Note the numerous bright spots just below the (Former) Top Pliocene horizon and the apparent absence of bright spots in the central part below the alluvial fan.

## 3.2 Concluding remarks

The conclusion will answer the research questions posed to understand the first seafloor fracture discovered in the unconsolidated sediments of the North Sea. We have established that the Hugin Fracture is approximately 30 m deep and linked to an alluvial fan with high-porosity sand fill. This glaci-fluvial fan appears to have a complex internal geometry with overall similar velocity. Further connection of this fan to abundant buried channels at larger depths were indicative in 3D data. Based on the small (< 1 m) layer offset at the fracture and the Pleistocene glaciation history of the study area, we favour ice-load induced differential compaction and associated strain accumulation as formation mechanism (Figure 10). Poroelastoplastic simulations show that the melting of thin (< 100 m) ice sheets can induce high-strain deformation and fracturing at buried channels with different sediment properties than the surrounding sediment layers. Focused high-strain accumulations in areas tangential to steep channels edges should have formed during earlier glaciation events and might be re-opened, if the pore pressure changes through e.g. wastewater or CO<sub>2</sub> injection.

A small-throw fault at a 60° angle to the orientation of the Hugin Fracture was identified in the first seal of the Utsira Fm. (at approximately 740 mbsf) but seems not to be connected to the seafloor or the Hugin Fracture. However, the heterogeneity in the Pleistocene sediments below the Hugin Fracture, the apparent drainage of Pliocene bright spots and the presence of dissolved hydrocarbons in the fluids escaping from the fracture leads to the conclusion that the overburden above the Utsira Fm. is considered compromised at the Fracture location.

## 3.3 Future perspectives

Additional high-resolution 2D seismic lines or P-cable 3D seismic data over the area of the Hugin Fracture (Plaza-Faverola, Bünz and Mienert 2011) would help to assess the fracture geometry in more detail. A future survey should extend both west- and eastwards of the mapped Hugin Fracture and include the northern margin of the identified alluvial fan. Coring of the top sediments at the fracture would help to

constrain the parameters for the numerical model and could help to assess the actual stress field. This could prove or disprove the proposed formation mechanism and help to determine if the fracture continues to grow as it is indicated by Cevatoglu (2015).

The numerical model should be updated with relevant geotechnical measurements and extended to a 3D geometry based on 3D seismic interpretation. Interesting questions include if the pattern of focused strain accumulation from the 2D model is maintained in simulations with a 3D model. The model should also be extended to include fluid flow through a defined fracture. This could aid in investigating the amount of fluid that could escape through such a narrow fracture and how much pore pressure increase would be needed to support this flow. Further simulation work may include investigation of several controlling factors such as channel geometry (wall steepness, depth and width), density and close occurrence of the channels, type and heterogeneity of sediment fill, and top depth as well as the influence of surrounding host sediments.

The presented simulation results suggest that ice load plays an important role for fracture development in unconsolidated sediments, also called soft rocks, and should be considered as additional fracturing mechanism in young sediments in glacial reworked areas. Especially heterogeneous sedimentary units like the channelized Pleistocene unit in the Central North Sea facilitate focussed stress/strain accumulations along stiffness contrasts between channel fill and host sediment at depths of up to several hundred meters. Similar fractures like the Hugin Fracture have most likely also formed during earlier glaciations and may therefore be part of a vertical-lateral fracture-channel-network that might facilitate fluid flow over larger depths and lengths. Mapping and characterizing channel structures could therefore be an important step in assessing the presence of open fractures for different stress regimes at depth (Grollmund and Zoback 2003). Another important question is related to the rate at which fluids could migrate through the suggested fracture network. For the purpose of geological CO<sub>2</sub> storage, it is important to know the leakage rate from the storage reservoir and the time needed for the CO<sub>2</sub> to move to a place outside the supercritical pressure-regime (Celia *et al.* 2005, Bachu 2008, Angeli *et al.* 2009, Cevatoglu 2015). Very low leakage rates (compared to injection rates) from the storage reservoir in

---

combination with migration times exceeding the onset of brine dissolution on the way would not affect storage plans (Gaus 2010).

Simulation results predict subtle topography, i.e. ridges, aligned above differentially compacted channels (paper III). The HISAS mosaic employed in this thesis shows large and partly linear areas of shell hashes that are exposed at the seafloor (Figure 5). Some of them appear to coincide with buried channels at larger depth. An objective of future studies could involve investigation of patterns of high backscatter energy on high-resolution seafloor maps on the Utsira High in combination with careful interpretation and attribute analysis of 3D seismic data, possibly P-cable seismic. This could reveal supporting evidence to ice-load induced differential compaction in the area. In addition, high-resolution P-cable seismic data will help to further determine in what way a fracture-channel-network could contribute in subsurface migration and drainage of water and hydrocarbons or how it could be re-opened by stress changes related to CO<sub>2</sub>-storage in deep geological formations (Plaza-Faverola *et al.* 2011).

Surface deformation and strength of topography continues during unloading, and the final deformation results in paper III show that the bottom of channel 1 is affected from the channel below. This could explain some of the bottom irregularities of large buried channels or tunnel valleys and should be investigated in future work.



## 4. References cited in Introduction and Synthesis

- Aber, J.S. 1982. Model for glaciotectonism. *Bulletin of the Geological Society of Denmark*, 30, 79–90.
- Aker, E., Bjørnarå, T., Braathen, A., Brandvoll, Ø., Dahle, H., Nordbotten, J.M., Aagaard, P., Hellevang, H., Alemu, B.L., Pham, V.T.H., Johansen, H., Wangen, M., Nøttvedt, A., Aavatsmark, I., Johannessen, T. and Durandh, D. 2011. SUCCESS: SUBsurface CO<sub>2</sub> storage–Critical elements and superior strategy. *Energy Procedia*, 4(Going), 6117–6124.
- Alnes, H., Eiken, O., Nooner, S. and Sasagawa, G. 2011. Results from Sleipner gravity monitoring: Updated density and temperature distribution of the CO<sub>2</sub> plume. *Energy Procedia*, 00.
- Andreassen, K., Nilssen, E.G. and Ødegaard, C.M. 2007. Analysis of shallow gas and fluid migration within the Plio-Pleistocene sedimentary succession of the SW Barents Sea continental margin using 3D seismic data. *Geo-Marine Letters*, 27(2–4), 155–171.
- Anell, I., Thybo, H. and Rasmussen, E. 2012. A synthesis of Cenozoic sedimentation in the North Sea. *Basin Research*, 24(2), 154–179.
- Angeli, M., Soldal, M., Skurtveit, E. and Aker, E. 2009. Experimental percolation of supercritical CO<sub>2</sub> through a caprock. *Energy Procedia*, 1(1), 3351–3358.
- Arts, R., Brevik, I. and Eiken, O. 2001. Geophysical methods for monitoring marine aquifer CO<sub>2</sub> storage–Sleipner experiences. IN: *5 th International Conference on Greenhouse Gas Control Technologies*. CSIRO Publishing.
- Arts, R., Chadwick, A., Eiken, O., Thibeau, S. and Nooner, S. 2008. Ten years' experience of monitoring CO<sub>2</sub> injection in the Utsira Sand at Sleipner, offshore Norway. *First break*, 26(January), 65–72.
- Bachrach, R. 2011. Mechanical compaction in heterogeneous elastic formations from plastic-poroelastic deformation principles: Theory and modeling results. *SEG Technical Program Expanded Abstracts 2011*, 2221–2225.
- Bachu, S. 2008. CO<sub>2</sub> storage in geological media: Role, means, status and barriers to deployment. *Progress in Energy and Combustion Science*, 34(2), 254–273.
- Barrio, M., Stewart, H.A., Akhurst, M., Aagaard, P., Alcalde, J. and Bauer, A. 2015. GlaciStore: Understanding Late Cenozoic Glaciation and Basin Processes for the Development of Secure Large Scale Offshore CO<sub>2</sub> Storage (North Sea). IN: *8th Trondheim Conference on CO<sub>2</sub> Capture, Transport and Storage, Trondheim, Norway, 16-18 June 2015*. Trondheim, pp. 1–2.
- Baumberger, T., Buenz, S., Landschulze, K., Pedersen, R.B., Blomberg, A., Tasianan, A. and Denny, A.R. 2014. *ECO<sub>2</sub> WP result summary report relevant for 'Environmental Best practise'*. ECO<sub>2</sub> Deliverable.
- Bjørlykke, K. 2006. Effects of compaction processes on stresses, faults, and fluid flow in sedimentary basins: examples from the Norwegian margin. *Geological Society, London, Special Publications*, 253(1), 359–379.
- Bjørlykke, K. 2015. Petroleum geoscience: From sedimentary environments to rock physics, second edition. *Petroleum Geoscience: From Sedimentary Environments to Rock Physics, Second Edition*, 1–662.

- Bjørlykke, K. and Hoeg, K. 1997. Effects of burial diagenesis on stresses, compaction and fluid flow in sedimentary basins. *Marine and Petroleum Geology*, 14(3), 267–276.
- Bjørlykke, K., Ramm, M. and Saigal, G.C. 1989. Sandstone diagenesis and porosity modification during basin evolution. *Geologische Rundschau*, 78(1), 243–268.
- Blomberg, A.E.A., Saebø, T.O., Hansen, R.E., Pedersen, R.B. and Austeng, A. 2017. Automatic Detection of Marine Gas Seeps Using an Interferometric Sidescan Sonar. *IEEE Journal of Oceanic Engineering*, 42(3), 590–602.
- Boulton, G.S., Caban, P. and Hulton, N. 1999. *Simulations of the Scandinavian ice sheet and its subsurface conditions*.
- Boulton, G.S. and Dobbie, K.E. 1993. Consolidation of sediments by glaciers: relations between sediment geotechnics, soft-bed glacier dynamics and subglacial ground-water flow. *Journal of Glaciology*, 39(131).
- Bradwell, T., Stoker, M.S., Golledge, N.R., Wilson, C.K., Merritt, J.W., Long, D., Everest, J.D., Hestvik, O.B., Stevenson, A.G., Hubbard, A.L., Finlayson, A.G. and Mathers, H.E. 2008. The northern sector of the last British Ice Sheet: Maximum extent and demise. *Earth-Science Reviews*, 88(3–4), 207–226.
- Brodzikowski, K., Gotowala, R., Haluszczak, A., Krzyszkowski, D. and Loon, A.J. Van 1987. Soft-sediment deformations from glaciodeltaic, glaciolacustrine and fluviolacustrine sediments in the Kleszczow Graben (central Poland). *Geological Society Special Publication*, (29), 255–267.
- Brown, A.R. 2008. Interpretation of Three-Dimensional Seismic Data. *AAPG Memoir*, 42(3), CR-Copyright &#169; 2008 Leonardo.
- Brudy, M. and Kjørholt, H. 2001. Stress orientation on the Norwegian continental shelf derived from borehole failures observed in high-resolution borehole imaging logs. *Tectonophysics*, 337(1–2), 65–84.
- Caramanna, G., Fietzek, P. and Maroto-Valer, M. 2011. Monitoring techniques of a natural analogue for sub-seabed CO<sub>2</sub> leakages. *Energy Procedia*, 4, 3262–3268.
- Cartwright, J. and Santamarina, C. 2015. Seismic characteristics of fluid escape pipes in sedimentary basins: Implications for pipe genesis. *Marine and Petroleum Geology*, 65, 126–140.
- Cavanagh, A. 2013. Benchmark Calibration and Prediction of the Sleipner CO<sub>2</sub> Plume from 2006 to 2012. *Energy Procedia*, 37, 3529–3545.
- Cavanagh, A. and Wildgust, N. 2011. Pressurization and brine displacement issues for deep saline formation CO<sub>2</sub> storage. *Energy Procedia*, 4, 4814–4821.
- Celia, M.A., Bachu, S., Nordbotten, J., Gasda, S.E. and Dahle, H.K. 2005. Quantitative estimation of CO<sub>2</sub> leakage from geological storage: Analytical models, numerical models, and data needs. *IN: Greenhouse Gas Control Technologies 7*. Elsevier, pp. 663–671.
- Cevatoglu, M. 2015. *Impact of subsurface fluid flow on sediment acoustic properties, implications for carbon capture and storage*. University of Southampton.
- Chadwick, A., Arts, R. and Bernstone, C. 2008. *Best practice for the storage of CO<sub>2</sub> in saline aquifers*. Keyworth Nottingham: BGS, NERC.
- Chadwick, A., Noy, D., Lindeberg, E. and Arts, R. 2006. Calibrating reservoir performance with



time-lapse seismic monitoring and flow simulations of the Sleipner CO<sub>2</sub> plume. *IN: GHGT-8*. Trondheim, Norway, p. 6.

Chadwick, R. and Holloway, S. 2000. The Utsira Sand, Central North Sea—an assessment of its potential for regional CO<sub>2</sub> disposal. *IN: GHGT-5*. Cairns, Australia: IEA.

Chadwick, R.A., Noy, D., Arts, R. and Eiken, O. 2009. Latest time-lapse seismic data from Sleipner yield new insights into CO<sub>2</sub> plume development. *Energy Procedia*, 1(1), 2103–2110.

Chopra, S. and Marfurt, K. 2007. Seismic curvature attributes for mapping faults/fractures, and other stratigraphic features. *CSEG Recorder*, (November), 38–42.

Chopra, S. and Marfurt, K.J. 2007. *Seismic attributes for prospect identification and reservoir characterization*. Society of Exploration Geophysicists and European Association of Geoscientists and Engineers.

COMSOL Inc. 2016. Comsol. Available from: <https://www.comsol.com/comsol-multiphysics> [Accessed October 15, 2016].

Cosgrove, J.W. and Hillier, R.D. 1999. Forced-fold development within Tertiary sediments of the Alba Field, UKCS: evidence of differential compaction and post-depositional sandstone remobilization. *Geological Society, London, Special Publications*, 169(1), 61–71.

Dehandschutter, B., Vandycke, S., Sintubin, M., Vandenberghe, N. and Wouters, L. 2005. Brittle fractures and ductile shear bands in argillaceous sediments: inferences from Oligocene Boom Clay (Belgium). *Journal of Structural Geology*, 27(6), 1095–1112.

Dupraz, C., Reid, R.P., Braissant, O., Decho, A.W., Norman, R.S. and Visscher, P.T. 2009. Processes of carbonate precipitation in modern microbial mats. *Earth-Science Reviews*, 96(3), 141–162.

Eidvin, T., Riis, F. and Rasmussen, E.S. 2014. Oligocene to Lower Pliocene deposits of the Norwegian continental shelf, Norwegian Sea, Svalbard, Denmark and their relation to the uplift of Fennoscandia: A synthesis. *Marine and Petroleum Geology*, 56, 184–221.

Fugro Survey AS 2012. *Site survey at planned well location 16/4-X final, LN11302, PL544*. Lysaker, Norway.

Gasparre, A. 2005. *Advanced Laboratory Characterization of London Clay*. Imperial College London.

Gaus, I. 2010. Role and impact of CO<sub>2</sub>–rock interactions during CO<sub>2</sub> storage in sedimentary rocks. *International Journal of Greenhouse Gas Control*, 4(1), 73–89.

Gibbard, P.L., Head, M.J. and Walker, M.J.C. 2010. Formal ratification of the Quaternary System/Period and the Pleistocene Series/Epoch with a base at 2.58 Ma. *Journal of Quaternary Science*, 25(2), 96–102.

Giroldi, L. and Alegria, F. 2005. Using spectral decomposition to identify and characterize glacial valleys and fluvial channels within the Carboniferous section in Bolivia. *The Leading Edge*, 1152–1159.

Graham, A.G.C., Stoker, M.S., Lonergan, L., Bradwell, T. and Stewart, M.A. 2013. The Pleistocene Glaciations of the North Sea basin. *Journal of Chemical Information and Modeling*, 53(9), 1689–1699.

Graham, A.G.C., Stoker, M.S., Lonergan, L., Bradwell, T. and Stewart, M.A. 2011. The Pleistocene

- Glaciations of the North Sea Basin. *IN*: J. Ehlers and P. Gibbard (eds.) *Quaternary Glaciations - Extent and Chronology*. pp. 261–278.
- Gregersen, U. and Johannessen, P.N. 2007. Distribution of the Neogene Utsira Sand and the succeeding deposits in the Viking Graben area, North Sea. *Marine and Petroleum Geology*, 24(10), 591–606.
- Gregersen, U., Michelsen, O. and Sørensen, J.C.J. 1997. Stratigraphy and facies distribution of the Utsira Formation and the Pliocene sequences in the northern North Sea. *Marine and Petroleum Geology*, 14(7), 893–914.
- Grollimund, B. and Zoback, M.D. 2003. Impact of glacially induced stress changes on fault-seal integrity offshore Norway. *AAPG Bulletin*, 87(3), 493–506.
- Grollimund, B. and Zoback, M.D. 2000. Post glacial lithospheric flexure and induced stresses and pore pressure changes in the northern North Sea. *Tectonophysics*, 327, 61–81.
- Grollimund, B., Zoback, M.D., Wiprut, D.J. and Arnesen, L. 2001. Stress orientation, pore pressure and least principal stress in the Norwegian sector of the North Sea. *Petroleum Geoscience*, 7(2), 173–180.
- Häckel, M., Wallmann, K., Schmidt, M., Liebetrau, V., Sommer, S., Schroller, D., Schoenfeld, J., Karstens, J. and Berndt, C. 2013. Fluid expulsion at a 3-km long fracture system in the Northern North Sea-geochemical constraints on the origin of gas and water. *IN: AGU Fall Meeting Abstracts*.
- Hamilton, E.L., Bachman, R.T. and Sandy, S. 1982. Sound velocity and related properties of marine sediments paper. *Journal of the Acoustic Society of America*, 72(6), 1891–1904.
- Hansen, R.E., Callow, H.J., Sabo, T.O. and Synnes, S.A.V. 2011. Challenges in seafloor imaging and mapping with synthetic aperture sonar. *IEEE Transactions on Geoscience and Remote Sensing*, 49(10 PART 1), 3677–3687.
- Harrington, J., Birchall, D., Noy, D., Cuss, R. and Graham, C. 2011. Consolidation and mass transport properties of the Nordland Shale. *IN: Geophysical Research Abstracts*. p. 12688.
- Hermanrud, C., Andresen, T., Eiken, O., Hansen, H., Janbu, A., Lippard, J., Bolås, H.N., Simmenes, T.H., Teige, G.M.G. and Østmo, S. 2009. Storage of CO<sub>2</sub> in saline aquifers—Lessons learned from 10 years of injection into the Utsira Formation in the Sleipner area. *Energy Procedia*, 1(1), 1997–2004.
- Horsrud, P., SØnsteBØ, E.F. and BØe, R. 1998. Mechanical and petrophysical properties of North Sea shales. *International Journal of Rock Mechanics and Mining Sciences*, 35(8), 1009–1020.
- Hovland, M. 1981. Characteristics of pockmarks in the Norwegian Trench. *Marine Geology*, 39(1–2), 103–117.
- Hovland, M. 2002. On the self-sealing nature of marine seeps. *Continental Shelf Research*, 22, 2387–2394.
- Hovland, M., Hegglund, R., De Vries, M.H. and Tjelta, T.I. 2010. Unit-pockmarks and their potential significance for predicting fluid flow. *Marine and Petroleum Geology*, 27(6), 1190–1199.
- Al Hseinat, M. and Hübscher, C. 2014. Ice-load induced tectonics controlled tunnel valley evolution - instances from the southwestern Baltic Sea. *Quaternary Science Reviews*, 97, 121–135.
- Huuse, M. and Lykke-Andersen, H. 2000. Overdeepened Quaternary valleys in the eastern Danish North Sea: Morphology and origin. *Quaternary Science Reviews*, 19(12), 1233–1253.

- Jackson, C. a.-L., Kane, K.E. and Larsen, E. 2010. Structural evolution of minibasins on the Utsira High, northern North Sea; implications for Jurassic sediment dispersal and reservoir distribution. *Petroleum Geoscience*, 16(2), 105–120.
- Jordt, H., Faleide, J., Bjørlykke, K. and Ibrahim, M. 1995. Cenozoic sequence stratigraphy of the central and northern North Sea Basin: tectonic development, sediment distribution and provenance areas. *Marine and Petroleum Geology*, 12(8), 845–879.
- Kanji, M.A. 2014. Critical issues in soft rocks. *Journal of Rock Mechanics and Geotechnical Engineering*, 6(3), 186–195.
- Karstens, J. and Berndt, C. 2015. Seismic chimneys in the Southern Viking Graben – Implications for palaeo fluid migration and overpressure evolution. *Earth and Planetary Science Letters*, 412, 88–100.
- Kehew, A.E., Piotrowski, J.A. and Jørgensen, F. 2012. Tunnel valleys: Concepts and controversies — A review. *Earth-Science Reviews*, 113(1–2), 33–58.
- Kennett, C. 2008. *Evaluation of internal geometries within the Miocene Utsira Formation to establish the geological concept of observed CO<sub>2</sub> responses on 4D seismic in the Sleipner area, North Sea*. PhD thesis, Imperial College London.
- Kristensen, T.B. and Huuse, M. 2012. Multistage erosion and infill of buried Pleistocene tunnel valleys and associated seismic velocity effects. *Geological Society, London, Special Publications*, 368(1), 159–172.
- Kristensen, T.B., Huuse, M., Piotrowski, J.A. and Clausen, O.R. 2007. A morphometric analysis of tunnel valleys in the eastern North Sea based on 3D seismic data. *Journal of Quaternary Science*, 22(8), 801–815.
- Kristensen, T.B., Piotrowski, J.A., Huuse, M., Clausen, O.R. and Hamberg, L. 2008. Time-transgressive tunnel valley formation indicated by infill sediment structure, North Sea – the role of glaciohydraulic supercooling. *Earth Surface Processes and Landforms*, 33(4), 546–559.
- Li, Q., Ito, K., Wu, Z., Lowry, C.S. and Loheide II, S.P. 2009. COMSOL Multiphysics: A Novel Approach to Ground Water Modeling. *Ground Water*, 47(4), 480–487.
- Lichtschlag, A., Cevatoglu, M., Connelly, D.P., James, R.H. and Bull, J.M. 2018. Increased Fluid Flow Activity in Shallow Sediments at the 3 km Long Hugin Fracture in the Central North Sea. *Geochemistry, Geophysics, Geosystems*, 2–20.
- Lonergan, L., Maidment, S.C.R. and Collier, J.S. 2006. Pleistocene subglacial tunnel valleys in the central North Sea basin: 3-D morphology and evolution. *Journal of Quaternary Science*, 21(8), 891–903.
- Løseth, H., Raulline, B. and Nygard, A. 2013. Late Cenozoic geological evolution of the northern North Sea: development of a Miocene unconformity reshaped by large-scale Pleistocene sand intrusion. *Journal of the Geological Society*, 170(1), 133–145.
- Mazzini, A., Jonk, R., Duranti, D., Parnell, J., Cronin, B. and Hurst, A. 2003. Fluid escape from reservoirs: implications from cold seeps, fractures and injected sands Part I. The fluid flow system. *Journal of Geochemical Exploration*, 78–79, 293–296.
- Mondol, N.H., Bjørlykke, K., Jahren, J. and Høeg, K. 2007. Experimental mechanical compaction of clay mineral aggregates-Changes in physical properties of mudstones during burial. *Marine and Petroleum Geology*, 24(5), 289–311.

- Nicoll, G. 2012. *Evaluation of the Nordland Group overburden as an effective seal for the Sleipner CO<sub>2</sub> storage site (offshore Norway) using analytical and stochastic modelling techniques*. PhD thesis, University of Edinburgh.
- Nikolinakou, M.A., Luo, G., Hudec, M.R. and Flemings, P.B. 2012. Geomechanical modeling of stresses adjacent to salt bodies: Part 2—Poroelastoplasticity and coupled overpressures. *AAPG Bulletin*, 96(1), 65–85.
- Nooner, S.L., Eiken, O., Hermanrud, C., Sasagawa, G.S., Stenvold, T. and Zumberge, M. a. 2007. Constraints on the in situ density of CO<sub>2</sub> within the Utsira formation from time-lapse seafloor gravity measurements. *International Journal of Greenhouse Gas Control*, 1(2), 198–214.
- Norsk Hydro AS 1990. *Final well Report 16/4-2 Licence 087 (Completion Report)*. Oslo, Norway. Available from: <http://factpages.npd.no/factpages/Default.aspx?culture=no>.
- Ottesen, D., Dowdeswell, J. a., Rise, L. and Bugge, T. 2012. Large-scale development of the mid-Norwegian shelf over the last three million years and potential for hydrocarbon reservoirs in glacial sediments. *Geological Society, London, Special Publications*, 53–73.
- Ottesen, D., Dowdeswell, J.A. and Bugge, T. 2014. Morphology, sedimentary infill and depositional environments of the Early Quaternary North Sea Basin (56° to 62°N). *Marine and Petroleum Geology*, 56, 123–146.
- Pedersen, R.B., Blomberg, A.E.A., Landschulze, K., Baumberger, T., Økland, I.E., Reigstad, L.J., Gracias, N., Mørkved, P.T., Thorseth, I.H., Stensland, A., Lilley, M.D. and Thorseth, I.H. 2013. Discovery of a 3 km long seafloor fracture system in the Central North Sea. *IN: Abstract #OS11E-03 presented at 2013 AGU Fall Meeting*. San Francisco, CA: AGU, p. Abstract #OS11E-03 presented at 2013 AGU Fall Meet.
- Pedersen, R.B., Landschulze, K., Blomberg, A.E.A., Gracias, N., Baumberger, T., Økland, I.E., Mørkved, P.T., Reigstad, L.J., Denny, A.R. and Thorseth, I.H. 2019. Discovery of seabed fluid flow along a 3 km long fracture in the Central North Sea. *In: Landschulze, K., Geophysical Investigation of the Hugin Fracture, a soft-sediment fracture on the Utsira High, North Sea*. PhD thesis, University of Bergen.
- Pillitteri, A., Cerasi, P., Stavrum, J., Zweigel, P. and Bøe, R. 2003. *Rock mechanical tests of shale samples from the cap rock of the Utsira Sand in well 15/9-A11 - A contribution to the Saline Aquifer CO<sub>2</sub> Storage (SACS) project*. Trondheim, Norway.
- Plaza-Faverola, A., Bünz, S. and Mienert, J. 2011. Repeated fluid expulsion through sub-seabed chimneys offshore Norway in response to glacial cycles. *Earth and Planetary Science Letters*, 305(3–4), 297–308.
- Praeg, D. 2003. Seismic imaging of mid-Pleistocene tunnel-valleys in the North Sea Basin—high resolution from low frequencies. *Journal of Applied Geophysics*, 53(4), 273–298.
- Reinardy, B.T.I., Hjelstuen, B.O., Sejrup, H.P., Augedal, H. and Jørstad, A. 2017. Late Pliocene-Pleistocene environments and glacial history of the northern North Sea. *Quaternary Science Reviews*, 158, 107–126.
- Rider, M. and Kennedy, M. 2013. *The Geological Interpretation of Well Logs*. 3rd ed. Rider-French Consulting Ltd.
- Rutqvist, J., Birkholzer, J.T. and Tsang, C.F. 2008. Coupled reservoir-geomechanical analysis of the potential for tensile and shear failure associated with CO<sub>2</sub> injection in multilayered reservoir-caprock

systems. *International Journal of Rock Mechanics and Mining Sciences*, 45(2), 132–143.

SCCS and Scottish Enterprise 2012. *CNS VALUE A D D*. Edinburgh, Scotland. Available from: <http://www.sccs.org.uk/expertise/cns/>.

Sejrup, H., Aarseth, I., Ellingsen, K.L., Reither, E., Jansen, E., Løvlie, R., Bent, A., Brigham-Grette, J., Larsen, E. and Stoker, M. 1987. Quaternary stratigraphy of the Fladen area, central North Sea: a multidisciplinary study. *Journal of Quaternary Science*, 2(1), 35–58.

Sejrup, H., Hafliðason, H. and Aarseth, I. 1994. Late Weichselian glaciation history of the northern North Sea. *Boreas*, 23(1991), 1–13.

Sejrup, H.P., Aarseth, I. and Hafliðason, H. 1991. The Quaternary succession in the northern North Sea. *Marine Geology*, 101(1–4), 103–111.

Sejrup, H.P., Clark, C.D. and Hjelstuen, B.O. 2016. Rapid ice sheet retreat triggered by ice stream debudding: Evidence from the North Sea. *Geology*, 44(5), 355–358.

Stewart, M. a. and Lonergan, L. 2011. Seven glacial cycles in the middle-late Pleistocene of northwest Europe: Geomorphic evidence from buried tunnel valleys. *Geology*, 39(3), 283–286.

Stewart, M., Lonergan, L. and Hampson, G. 2012. 3D seismic analysis of buried tunnel valleys in the Central North Sea: tunnel valley fill sedimentary architecture. *Geological Society, London, Special Publications*, 368(1), 173–184.

Storvoll, V., Bjørlykke, K., Karlsen, D. and Saigal, G. 2002. Porosity preservation in reservoir sandstones due to grain-coating illite: A study of the Jurassic Garn Formation from the Kristin and Lavrans fields, offshore Mid-Norway. *Marine and Petroleum Geology*, 19(6), 767–781.

Torp, T.A. and Gale, J. 2004. Demonstrating storage of CO<sub>2</sub> in geological reservoirs: The Sleipner and SACS projects. *Energy*, 29(9–10), 1361–1369.

Tsang, C.-F., Birkholzer, J. and Rutqvist, J. 2007. A comparative review of hydrologic issues involved in geologic storage of CO<sub>2</sub> and injection disposal of liquid waste. *Environmental Geology*, 54(8), 1723–1737.

Tvedt, A.B.M., Rotevatn, A., Jackson, C.A.-L., Fossen, H. and Gawthorpe, R.L. 2013. Growth of normal faults in multilayer sequences: A 3D seismic case study from the Egersund Basin, Norwegian North Sea. *Journal of Structural Geology*, 55, 1–20.

Vanneste, K., Meghraoui, M. and Camelbeeck, T. 1999. Late Quaternary earthquake-related soft-sediment deformation along the Belgian portion of the Feldbiss Fault, Lower Rhine Graben system. *Tectonophysics*, 309(1–4), 57–79.

Verdon, J.P., Kendall, J.-M., Stork, A.L., Chadwick, R.A., White, D.J. and Bissell, R.C. 2013. Comparison of geomechanical deformation induced by megatonne-scale CO<sub>2</sub> storage at Sleipner, Weyburn, and In Salah. *Proceedings of the National Academy of Sciences of the United States of America*, 110(30), E2762-71.

Vialle, S. and Vanorio, T. 2011. Laboratory measurements of elastic properties of carbonate rocks during injection of reactive CO<sub>2</sub>-saturated water. *Geophysical Research Letters*, 38(1), n/a-n/a.

Wallmann, K. 2010. Sub-seabed CO<sub>2</sub> Storage: Impact on Marine Ecosystems (ECO<sub>2</sub>). *AGU Fall Meeting Abstracts*, 111.

Wattrus, N.J., Rausch, D.E. and Cartwright, J. 2003. Soft-sediment deformation in Lake Superior:

evidence for an immature Polygonal Fault System? *Subsurface Sediment Mobilization*, 216, 323–334.

Williams, J.P. and Aurora, R.P. 1982. Case Study of an Integrated Geophysical and Geotechnical Site Investigation Program for a North Sea Platform. *IN: Offshore Technology Conference*. Offshore Technology Conference.

Wood, D.M. 1990. *Soil behaviour and critical states soil mechanics*. Cambridge University Press, United Kingdom and New York.

Xu, S., Hao, F., Xu, C., Wang, Y., Zou, H. and Gong, C. 2015. Differential compaction faults and their implications for fluid expulsion in the northern Bozhong Subbasin, Bohai Bay Basin, China. *Marine and Petroleum Geology*, 63, 1–16.

Zep Zero emissions platform 2013a. *Building a CO<sub>2</sub> transport infrastructure for Europe*. Available from: [www.zeroemissionsplatform.eu](http://www.zeroemissionsplatform.eu).

Zep Zero emissions platform 2013b. *CO<sub>2</sub> Capture and Storage (CCS) in energy-intensive industries*. Available from: [www.zeroemissionsplatform.eu](http://www.zeroemissionsplatform.eu).

Zweigel, P., Arts, R., Lothe, A.E. and Lindeberg, E.B.G. 2004. Reservoir geology of the Utsira Formation at the first industrial-scale underground CO<sub>2</sub> storage site (Sleipner area, North Sea). *Geological Society, London, Special Publications*, 233(1), 165–180.

---

## 5. Appendix





## 5.1 Seismic interpretation workflow and results

This appendix includes an excerpt of an internal interpretation report and is supported to give a deeper understanding of the interpretation work.

The 3D seismic dataset available for this study is a merge of several seismic cubes and covers an area of c. 3000 km<sup>2</sup> with ED50-UTM31 as Coordinate Reference System (CRS). The initial interpretation was performed on a c. 980km<sup>2</sup> large sub-cube (black solid rectangle in Figure 5.1 - 1).

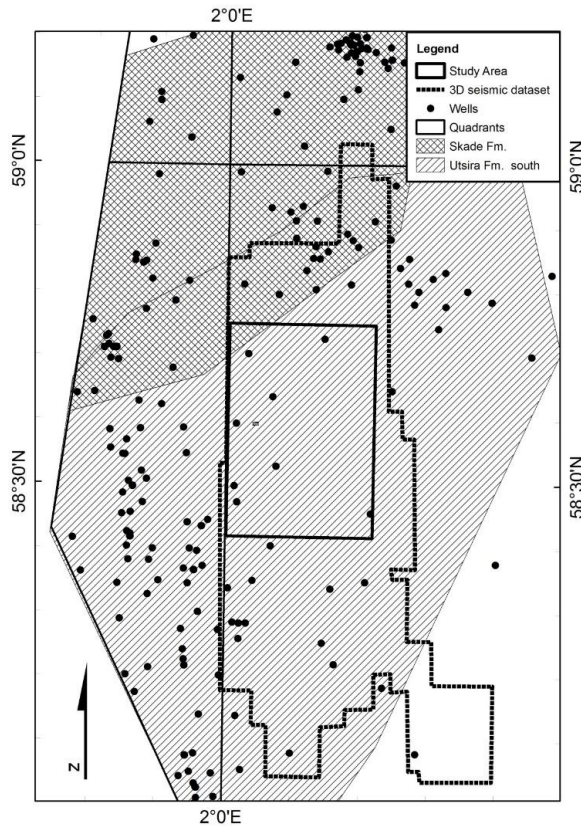


*Figure 5.1 - 1: Study area with shape of the 3D seismic mega-merge (courtesy of Lundin Norway AS) and the 980 km<sup>2</sup> subset that was interpreted for a larger geological overview.*

Initial interpretation efforts with Petrel 2012 showed relatively high noise in the near-seafloor reflections. In addition, the objective of identifying fluid migration pathways and small-scale geological structures below the Hugin Fracture called for advanced seismic attributes, such as frequency decomposition. To this end, the dataset was processed in a noise cancellation workflow in GeoTeric 2013 as means to conditioning the 3D seismic dataset for frequency decomposition. The aim was to enhance reflector continuity and maintaining vertical disturbances.

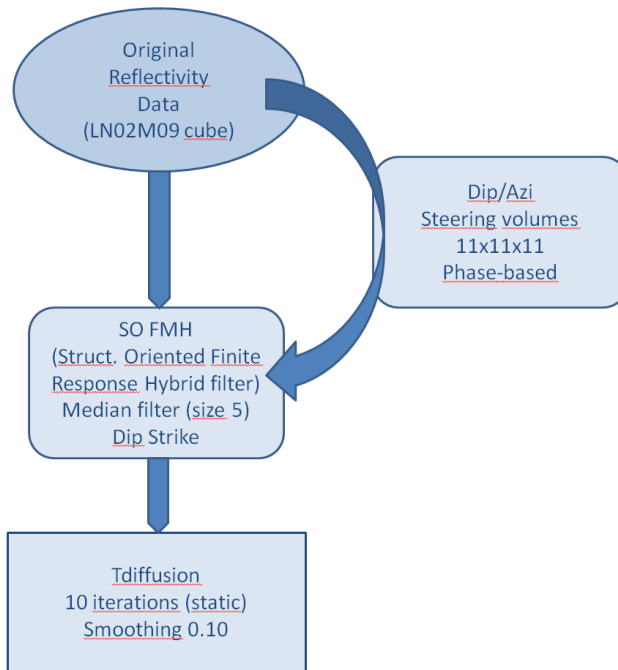


*Figure 5.1 - 2: Noise cancellation workflow using the depicted processes/algorithms and parameters in Geoteric 2013.*

The noise-cancelled cube was further interpreted using a combination of automatic and manual tracking of major horizons for establishing an overview of the local/regional geology. The interpreted layers were the seafloor, the Top Pliocene horizon, the Intra Pliocene horizon and the Top Utsira Fm. Additionally, the bottom of what appears to be a uniform seismic unit with a peculiar fan-like shaped was interpreted, manually. Nicoll (2012) points out that the Top Pliocene and the Intra Pliocen actually represent Pleistocene unconformities after a reclassification of the Gelasian stage (formerly late

Pliocene) as Pleistocene (Gibbard, Head and Walker 2010). Interpretation was carried out in accordance with earlier stratigraphic names, to conform with earlier works. In the following, the horizons initial characteristics are described.

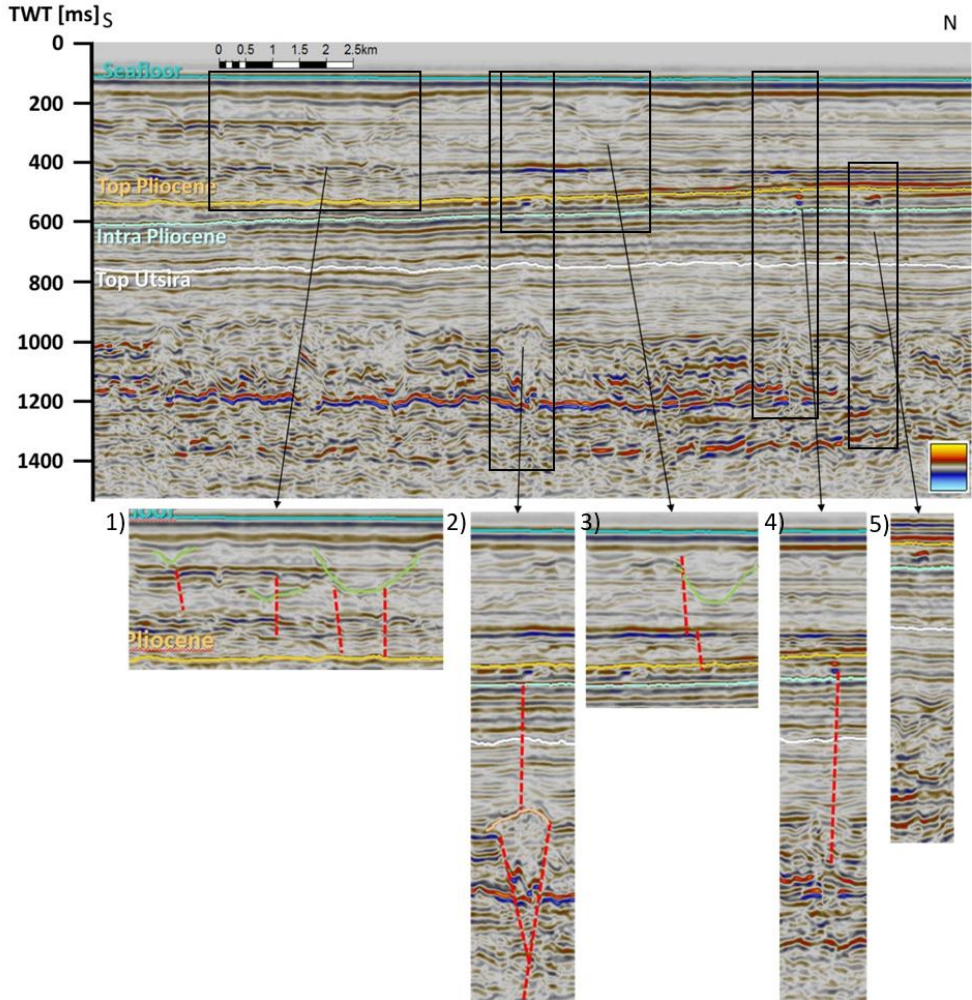


*Figure 5.1 - 3: Example section with faults or fractures close to seismic resolution. Insets from left to right: 1 shows several channels and small-scale linear features. 2: At a depth of 900-1200 ms a possible sand injectite structure with forced folding on top can be seen. 3: another shallow channel with linear features seemingly connecting to the Pliocene unit. 4: A bright spot with a linear trace down to a chaotic structure with less amplitude than right next to it. 5: A similar bright spot without linear feature.*

### *Seafloor*

The seafloor represents a major increase in acoustic impedance, when the acoustic velocity increases from 1500 m/s in seawater to almost 1900 m/s in the water-saturated sediments. In the 3D seismic dataset, the seafloor is represented by a blue trough, hence the data have SEG reverse polarity. Throughout the study area, the seafloor exhibits no major topography and is a flat horizon at about 125 ms TWT (c. 93 m with water velocity of 1500 m/s).

### *Top Utsira*

From well 16/4-2 as fact base for depths and formation tops, top Utsira is located at 778m depth at the well location. This corresponds to approximately 778 ms TWT where there is a prominent blue reflector enclosed by two relatively prominent red reflectors. All the three were traced, as it was sometimes difficult to determine which of them was correct by only tracing one red/blue.

In the southernmost part of the seismic sub-cube, the upper red reflector seems to be at the base of a prograding sequence which makes it difficult to decide which red reflection should be followed. Prograding deposits easily mislead the interpreter to follow the stronger red reflection dipping upwards. It was decided to stay as close to the blue reflection (identified as Top Utsira) as possible.

This horizon runs almost horizontal with a marginal dip to the north.

### *(Former) Top Pliocene*

Top Pliocene unconformity is characterized as a blue reflector, prominent through the presence of numerous bright spots directly below it. In fact, most of the shallow bright spots in the area are located just below Top Pliocene. This reflector is easily followed throughout the seismic cube. The Top Pliocene unconformity represents the upper boundary for the Late Pliocene Unit (LPU) and represents a gently SE-dipping (0.34 degrees), regional horizon located at 400 to 675 ms TWT depth in the study area. The unit displays numerous bright spots. In fact, the Top Pliocene horizon is in this work

---

tracked as a downward decrease in acoustic impedance (red reflection) just above the zone with frequent bright spots. This could correspond to a downward change in lithology from shale to beds with a higher proportion of sandstone which, in general, has a higher porosity and thus water/hydrocarbon content than shale. It suggests also a change from lower porosity in the Pleistocene unit to higher porosity in the LPU. The fact that a high number of sometimes large bright spots (believed to represent local accumulations of hydrocarbon) are found just below the Top Pliocene unconformity, suggests that the Pleistocene sediments act as a top seal, preventing upwards migration of hydrocarbons from the LPU.

*(Former) Intra Pliocene*

Red reflector right below a relatively good blue reflector, determining the lower boundary of most of the bright spots in the Pliocene rocks. This horizon was used to conduct geobody extraction of numerous bright spots just below the Top Pliocene. It runs sub-parallel to the Top Pliocene horizon, having almost the same dip.

*Pleistocene unit (from Former Top Pliocene to seafloor)*

The topmost seismic unit is up to 575 ms thick and confined by the seafloor as the upper boundary and the (Former) Top Pliocene unconformity as the lower boundary. Various small-scale features such as erosional channels or tunnel valleys, small bright spots and vertical disturbances are abundant in this unit, reflecting a glacially influenced depositional environment during the Pleistocene. Medium amplitude reflectors onlapping onto the lower boundary are also found in the lower part of this unit. A strong seafloor multiple at about 250 ms interferes with the channel structures at this depth. Another strong reflector at about 410 ms, above the onlapping reflectors of the lower part, matches the boundary between CSS-9 and CSS-10 in Jordt *et al.* (1995) (Figure 5.1 - 4). This reflector is strong in the southern part of our study area but fades towards the North and is difficult to track.

Previous regional studies of the upper sediments in the North Sea define between four and eight seismic units in the sediment succession from Middle Miocene age to present

(Jordt *et al.* 1995, Anell, Thybo and Rasmussen 2012, Ottesen *et al.* 2014, Gregersen, Michelsen and Sørensen 1997). We interpret only three (Figures 5.1 - 4), despite in some areas there seems to be a well-defined continuous reflector (hard) in between the seafloor and the (Former) Top Pliocene, at c.420 ms TWT.

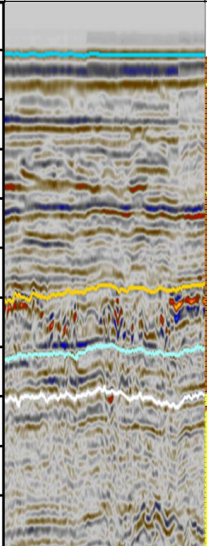
Depth (ms TWT)	3D seismic	Lit.	Age	Strat.	Seismic strat.		Comments																		
					Units	Jordt et al. (1995)																			
100			Pleistocene	Unnamed	III	CSS-10	<ul style="list-style-type: none"> <li>• Parallel reflectors of medium to strong amplitude in the upper part</li> <li>• Onlap onto lower boundary in the lower part</li> <li>• Channels/tunnel valleys</li> <li>• Small bright spots</li> <li>• Fracture indications</li> <li>• Various vertical disturbances</li> </ul>																		
200								Pliocene	Unnamed	I	CSS-8														
300					Miocene	Nordland Group						Utsira Fm	CSS-7												
400														I	CSS-8										
500																I	CSS-8								
600																		I	CSS-8						
700																				I	CSS-8				
800																						I	CSS-8		
900																								I	CSS-8
1000																									
	I	CSS-8																							
			I	CSS-8																					

Figure 5.1 - 4: Comparison of our interpretation of major horizons with the framework of Jordt *et al.* 1995. Note that the top horizon is the precursor of the seafloor.



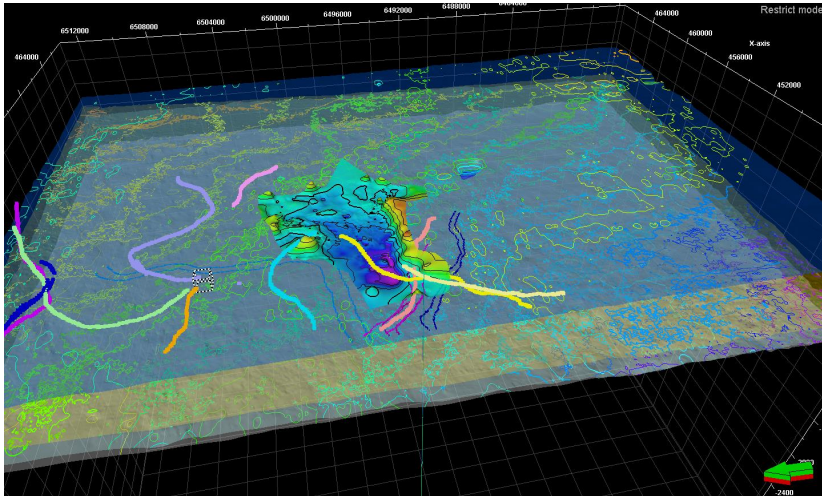
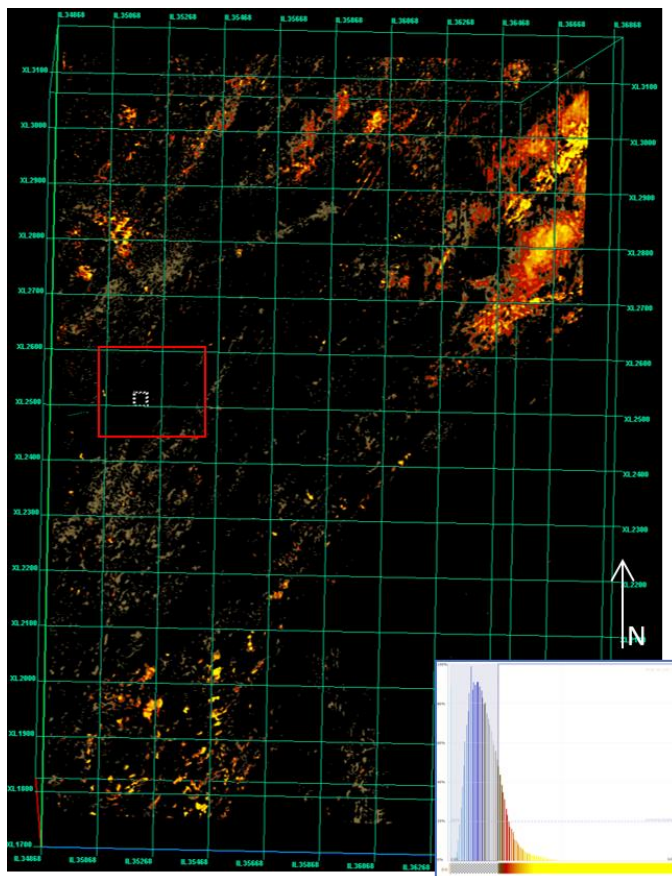


Figure 5.1 - 5: Gridded surfaces from initial 980 km<sup>2</sup> 3D seismic subset including (Former) Top Pliocene, (Former) Intra Pliocene and Top Utsira (from top to bottom). Above them the bottom of the glacial fan. Lines indicate other channel center lines.

The presence of numerous gas-indicating bright spots just below the (Former) Top Pliocene shows an apparent void below the Hugin Fracture, possibly indicative of drainage of the assumed evenly charged layers. Reverse polarity of these bright spots as compared to seafloor reflection indicates a drop in acoustic impedance and, hence, the presence of gas (Andreassen, Nilssen and Ødegaard 2007). Geobody extraction based on the Reflection Intensity attribute in the interval between (Former) Top Pliocene and (Former) Intra Pliocene was performed and revealed a clear NE-SW trend in the distribution of bright spots in the study area (Figure 5.1 - 6). The distribution of the bright spots indicates some structural control, like the dipping of the (Former) Top Pliocene horizon and possibly others.



*Figure 5.1 - 6: Bright spots from Reflection Intensity cube in the interval between Top Pliocene and Intra Pliocene. Small white square indicates Hugin Fracture location, over an apparent void in the Pliocene bright spots (red rectangle). Inset shows the opacity settings for extracting geobodies based on large Reflection intensity values.*

For a better understanding of the fan-like structure, frequency decomposition was carried out in GeoTeric 2013. Results showed that the fan-like structure was almost transparent, indicating low frequency content inside the channel compared to the surrounding. At larger depth, where channels were abundant a channel with similar low frequency is found to the north of the shallow.



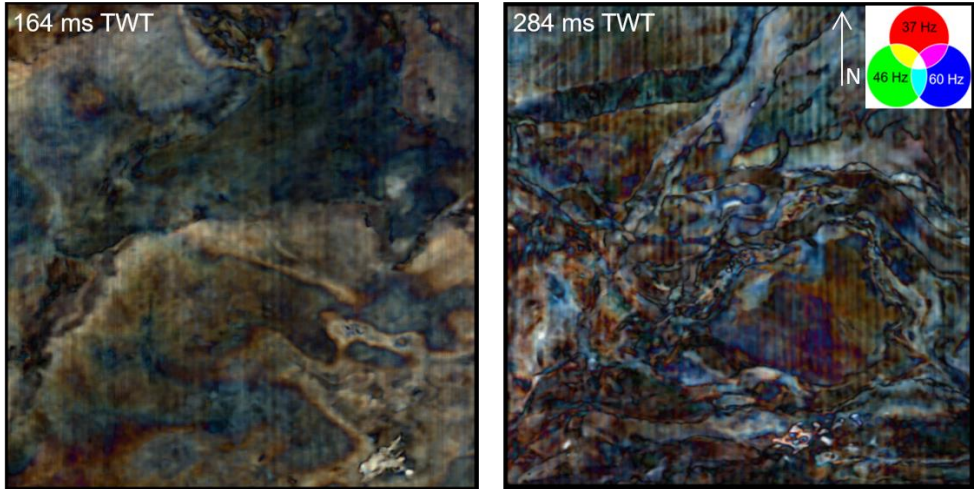


Figure 5.1 - 7: Frequency decomposition with the frequency bands around 37 Hz, 46 Hz and 60 Hz of a small subarea of the seismic dataset. Dark areas indicate absence of chosen frequency bands, light areas show presence of all frequency bands.

The seismic data show chaotic reflections and indications of fractures several (Figure 5.1 - 1).

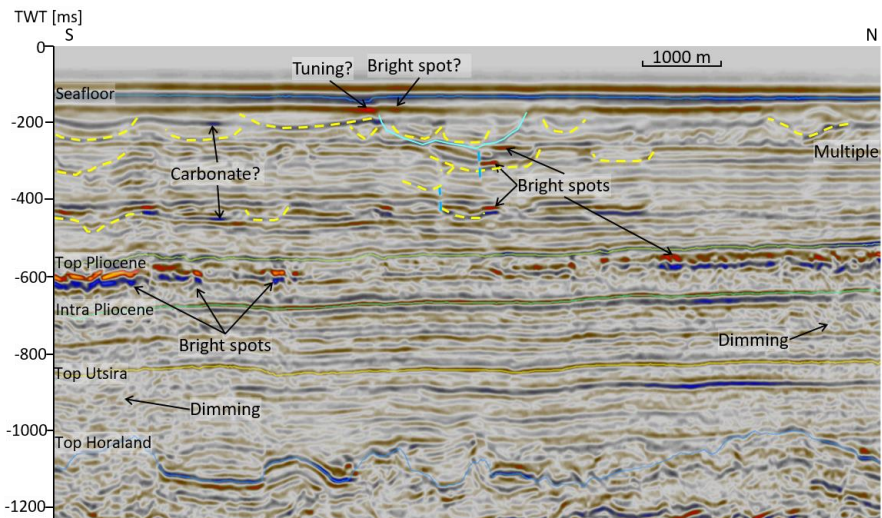
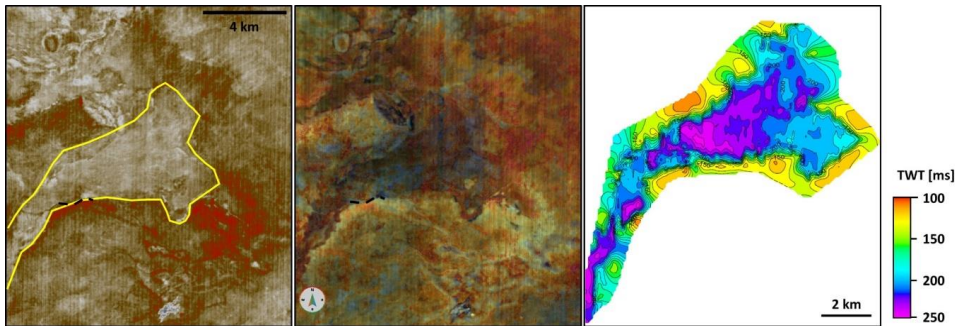


Figure 5.1 - 8: Example section from 3D seismic showing several channels, bright spots and indications of fractures.

A comparison of the seismic amplitude, frequency decomposition shows a distinct change in seismic signature over short lateral distance, indicating different lithology.



*Figure 5.1 - 9: Seismic, frequency decomposition and bottom map of the identified alluvial fan. Note different scale in the right display, compared to left and centre display.*

Bottom depth map may be used for morphological interpretation of the fan-like structure (Figure 5.1 - 9).

In the further interpretation work, we focussed on a smaller subset, c.118 km<sup>2</sup> large. Here, the Base of the Swatchway and Coal Pit Fm. was tracked in addition, based on correlation with well logs, 2D lines from ST0694 and a site survey report (Fugro Survey AS 2012). The following figures show the interpreted surfaces from the 118 km<sup>2</sup> 3D seismic cube. The seafloor reflector was tracked by 3D automatic tracking based on one seed point and shows some anomalies. In the north, a broad ridge can be seen. At the same location a channel is located at larger depth, indicating differential compaction of the sediments and subsequent topography inversion. Near the Hugin Fracture location, a local depression is seen, resulting from a bright spot (tuning effect?) just below the seafloor reflection that misguides the 3D-autotracker. The Base Swatchway and Coal Pit Fm. was difficult to interpret, as it is heavily eroded by cross-cutting buried channels (Figure 5.1 - 10). Especially in the central part (inside the shaded polygon), the interpretation is uncertain at best.

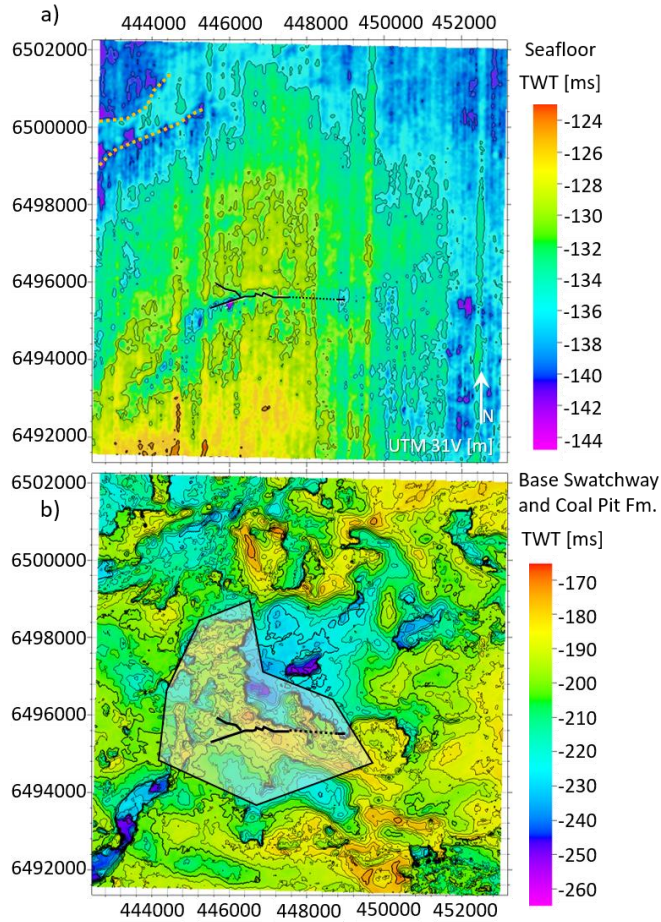


Figure 5.1 - 10: a) Seafloor and b) Base Swathway and Coal Pit Fm. surface.

As reported by others, the (Former) Pliocene surfaces are flat, sub-parallel horizons with a gentle dipping towards the SE (Anell *et al.* 2012, Ottesen *et al.* 2012) (Figure 5.1 - 11). The Top Utsira Fm. is also relatively flat with some minor topography, while the Top Hordaland shows irregular mounds that have been interpreted to represent sand injectites (e.g. Kennett 2008, Løseth, Raulline and Nygard 2013) (Figure 5.1 - 12). The Top Hordaland surface shows areas of spikes and linear interpretation errors, illustrating challenges in distinguishing the Top Hordaland in the seismic data. However, the typical irregular mounds are evident in areas of good interpretation



quality (e.g. in the southeast of the study area), as well as below the Hugin Fracture, although the interpretation is less certain.

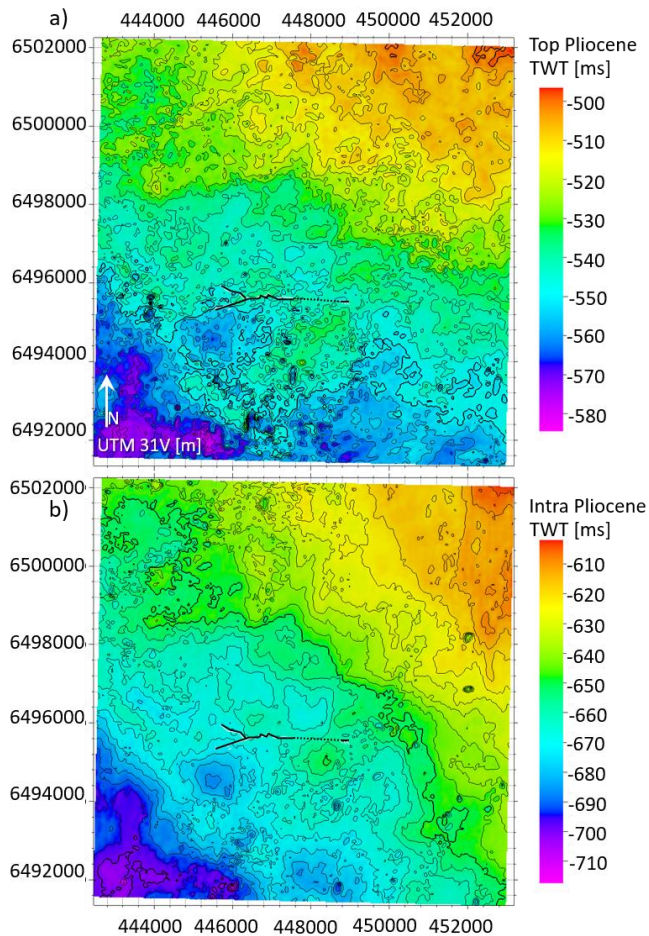


Figure 5.1 - 11: a) Top Pliocene and b) Intra Pliocene surface.

The overall impression is that Quaternary glaciations have left a heterogeneous Pleistocene sediment record throughout the study area with abundant channels or tunnel valleys of varying fill. A simplified impression is given in Figure 5.1 - 13.

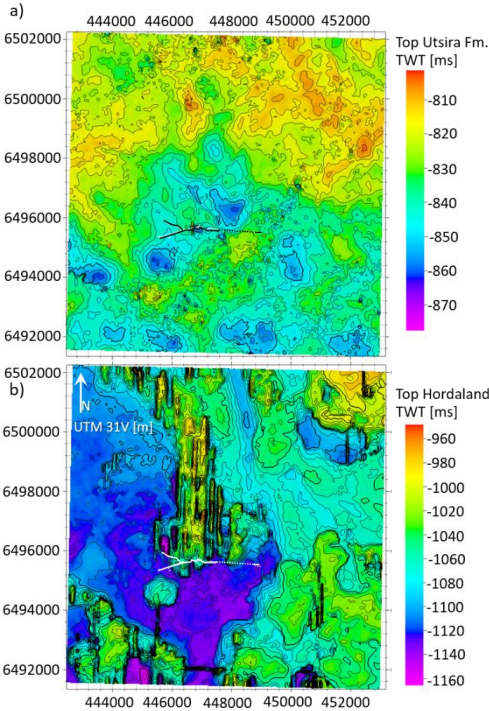


Figure 5.1 - 12: a) Top Utsira Fm. and b) Top Hordaland group surface.

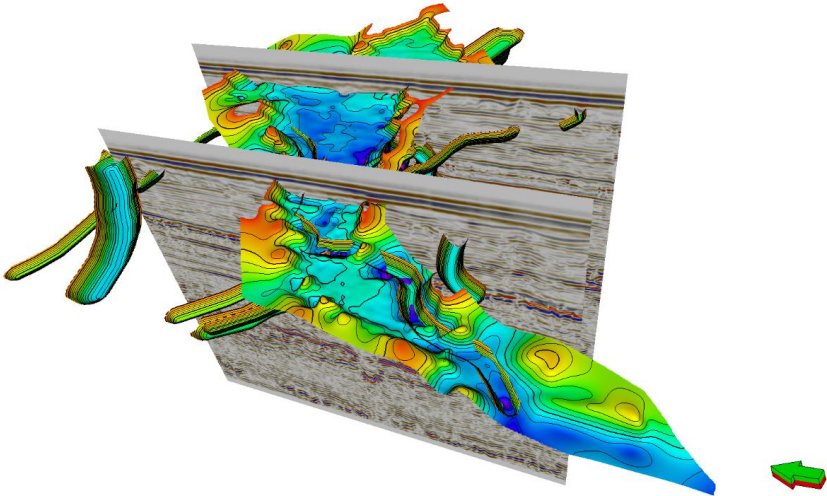


Figure 5.1 - 13: 3D view on the interpreted bottom of the alluvial fan and some Pleistocene buried channels crossing the area. Depth scale covers 110 ms TWT elevation for all channels, except the bottom of the alluvial fan.

## 5.2 Geomechanical model

Real sediments are composed of a variation of grains, both in form and chemical elements, having some porosity and reacting to strain with elastic and plastic deformation. Deposition in water, and hence fully saturated sediments, is expected for the Hugin Fracture area, despite some dry land periods related to Quaternary interglacials (Graham *et al.* 2011). Under normal consolidation clayey sediments start at higher porosity that decreases rapidly with depth while sandy sediments start at lower porosity and are able to retain more of their original porosity; this depends mainly on sorting and grain size but also on mineral content (Bjørlykke and Hoeg 1997, Mondol *et al.* 2007). Cementation may result in significantly lower porosities, that is prevented by chlorite or illite coating of grains (e.g. Storrøvoll *et al.* 2002).

Elastic deformation is a reversible volumetric change due to stress that is important in rocks. Due to the higher compaction ability of unconsolidated sediments elastic deformation is much less important than plastic deformation (Wood 1990). Per definition, plastic deformation is an irreversible deformation due to rearrangement of linear or platy minerals, grain crushing and chemical reactions between grains. Consolidation, or drainage of water from the soil, does not itself present a plastic deformation, although drainage is a prerequisite for plastic deformation to occur. In an undrained case the water is prevented from leaving the pores and takes up the load stress, preventing a rearrangement of grains and increases pore pressure. In cases where rapid sedimentation impedes pore fluid to escape this leads to disequilibrium compaction. Higher pore-pressures in layers below rapidly deposited sediments precludes compaction and leads to less compacted sediments with pore fluid pressure above the hydraulic gradient. Spatially variable rapid sedimentation may have happened in the study area during deglaciation evidenced by the various states of consolidation that are found for sediments of the Nordland Group (Sejrup, Haflidason and Aarseth 1994, Pillitteri *et al.* 2003, Harrington *et al.* 2011, Sejrup *et al.* 2016) Glaciation/deglaciation cycles have also induced spatially variable stress as is confirmed through well measurements and simulations (Grollimund and Zoback 2000, Grollimund *et al.* 2001, Grollimund and Zoback 2003).

Heterogeneities in the sediments below an ice sheet, such as the seismically observed channels or tunnel valleys, can have major impact on the shape of the stress field and associated deformation of the sediments. Contrasting consolidation behaviour of sandy and clayey soils (e.g. Bjørlykke 2015). In the case of the Hugin Fracture, complexity is added by the presence of over-consolidated clay layers (tills) that were eroded by glaci-fluvial channels and sub-glacial tunnel valleys and subsequently buried with younger sediments (Sejrup *et al.* 1987, Boulton and Dobbie 1993). As this heterogeneous (in age and material) sediment unit undergoes glacial loading, the younger sediment is more susceptible to compaction than the older sediment. In the study area, over-consolidated sediment layers have been found at several locations (e.g. Sejrup *et al.* 1987). Over-consolidated clays are stiffer than their burial depth suggests and can withstand higher shear stresses without significant deformation, but they are also prone to react with brittle failure when the stress becomes very large or changes suddenly (Boulton and Dobbie 1993).

### *2D or 3D model*

The Earth is essentially three-dimensional and, hence, models should be three-dimensional as well, to be as close to the real world as possible. On the other hand, two-dimensional (2D) models are easier to start with, both with respect to computational cost and interpretation complexity. We decided to start with a 2D model based on an interpreted 3D seismic section with normal orientation to the Hugin Fracture. If the hypothesis to be tested appears to be reasonable according to the simulation results, an extension of the model to 3D will be the next natural step.

### *Simulation parameters*

Initial simulations were carried out with COMSOL Multiphysics 5.1 using a poroelastic-elastoplastic model, where sand bodies were represented by poroelastic domains and the background clayey sediments by an elastoplastic domain.

	Sand	Sandstone	Clay	Till	Caprock (clay)	Soft sediment
<b>Density</b>					2.05-2.15 g/cm <sup>3</sup>	2.7 g/cm <sup>3</sup>
<b>Young's modulus</b>				0.19-0.29 GPa		
<b>Poisson ratio</b>		0.24-0.35			0.18-0.25	
<b>Cohesion</b>	16-40 kN/m <sup>2</sup> 6-19 kPa	350 kPa		18 kPa		<0.5Mpa
<b>Internal Friction</b>	38-40°	48°		24°	0.6	
	50-66°					
<b>Permeability</b>		5-1000 mDarcy	10 <sup>-11</sup> m <sup>2</sup> – 2 · 10 <sup>-9</sup> m <sup>2</sup>	10 <sup>-7</sup> m <sup>2</sup> – 10 <sup>-5</sup> m <sup>2</sup>	0.001 mDarcy (horizontal) 0.0001 mDarcy (vertical)	2 · 10 <sup>-16</sup> m <sup>2</sup> 6 · 10 <sup>-13</sup> m <sup>2</sup>
<b>Porosity</b>		38%	34-65%		33-36%	52-55%
<b>Shear strength</b>				184 kPa		0 – 0.05 MPa
<b>Source</b>	(Sitar, Clough and Bachus 1980, Hampton 2002)	(Sitar <i>et al.</i> 1980)	(Boulton and Dobbie 1993)	(Boulton and Dobbie 1993)	(Pillitteri <i>et al.</i> 2003, Grollimund and Zoback 2003, Nicoll 2012)	(Daigle and Dugan 2011)
<b>Remarks</b>				Effective porosity is much lower due to low connectivity of voids.	Eff. stresses are <i>in situ</i> (at 910 m depth) and higher than expected from overburden density (6-7 MPa) suggested cause is ice sheet loading. Friction is given in absence of cohesion.	

Table 5.2 - 1: Literature values and references for different sediment parameters.



For the modelling parameters, direct geotechnical measurements from the study area were not available. Published research was reviewed to identify reasonable model parameter ranges (Table 5.2 - 1). The values and sediment/rock are given in respective paper units and terms.

Different Processes that may be of importance for either the model or the interpretation of the simulation results were also acquired from literature review. They are listed in Table 5.2 - 2.

Process	Value	Remark	Reference
<b>Temperature gradient</b>	33°C/km 38°C/km for shales & 26°C/km in sands		(Nooner <i>et al.</i> 2007) (Zweigel <i>et al.</i> 2004) (Nooner <i>et al.</i> 2007)
<b>Glacier Loading</b>	3530-5950 kPa	Saale glaciation Netherlands/North Sea	Boulton and Dobbie (1993)
<b>Ice thickness</b>	392-661 m  200 m  200-1500 m	Saale glaciation Netherlands/North Sea Pleistocene North Sea 20000 years past (Pleistocene)	(Boulton and Dobbie 1993)  (Pillitteri <i>et al.</i> 2003)  (Grollimund and Zoback 2003)
<b>Gravitational pore pressure gradient (water)</b>	10 kPa/m	self-weight of sediments including interstitial water, i.e. sediments with permeabilities smaller than about $10^{-8} \text{ m}^2$ ( $10^4$ darcy) will tend to develop large effective pressure gradients	Boulton and Dobbie (1993)
<b>pressure gradient</b>	10 kPa/m	hydrostatic at Sleipner	Zweigel <i>et al.</i> , 2004a
<b>Pore pressure equilibrium time (low permeability)</b>	$10^3$ years		Boulton and Dobbie (1993)
<b>Pore pressure equilibrium</b>	10 years		Boulton and Dobbie (1993)

<b>time (high permeability)</b>			
<b>Brine density</b>	1013-1040 kg/m <sup>3</sup>		Nicoll (2012)
<b>Capillary entry pressure</b>	1.6-1.9 Mpa	Sleipner Caprock & gaseous CO <sub>2</sub> high uncertainty	Springer & Lingren (2006)
<b>Fluid flow (fracturing)</b>	4-28 mm/yr @10 <sup>-18</sup> m <sup>2</sup> permeability 430 mm/yr @6 · 10 <sup>-13</sup> m <sup>2</sup> / 2 · 10 <sup>-16</sup> m <sup>2</sup>	Fracturing for methane flow through soft, coarse and fine-grained sediment	Daigle & Dugan (2011)

Table 5.2 - 2: Different processes and literature values of their effects.

Based on the literature review, ranges for different important model parameters were chosen. Table 5.2 - 3 gives an overview over them.

	<b>Channel (poroelastic)</b>	<b>Main (linear elastic, soil plasticity)</b>		
		Clay-rich sheared (0.9-2.0MPa)	Clay-rich Unsheared	sand/silt (unconsolidated)
Porosity (Hamilton 1971)	38,6-55 %		71-73.5%	53-67%
Young's Modulus (Hamilton 1971)	1979.82-1323.58 kN/cm <sup>2</sup>		922.63-917.44 kN/cm <sup>2</sup>	966.8-1017.38 kN/cm <sup>2</sup>
Poisson ratio (Hamilton 1971)	0.491-0.457		0.478-0.480	0.461-0.463
Density (Hamilton 1971)	2.71-2.677 g/cm <sup>3</sup>		2.689-2.715 g/cm <sup>3</sup>	2.644-2.661 g/cm <sup>3</sup>
		15-133 kPa	9-70 kPa	6-40 kPa
Angle of internal friction		22° (?)		38°-66°

(Hampton 2002)				
Shear strength (steady state at 4 mm) (Ikari & Kopf 2011)		39-946 kPa		
Permeability (Bolton <i>et al.</i> 2000)		Vertical: $2 \cdot 10^{-18} - 9 \cdot 10^{-18} \text{ m}^2$		
		Horizontal: $1 \cdot 10^{-18} - 100 \cdot 10^{-18} \text{ m}^2$ (larger values for eff. stress below 200 kPa)		
Dynamic Viscosity (Sharqawy <i>et al.</i> 2010)	$1800 \frac{\text{kg}}{\text{m s}}$ $= 1800 \text{ Pa s}$			
Compressibility of fluid (Pierrot & Millero 2000)	$-5.7 \cdot 10^3 - 6.15 \cdot 10^3 \text{ (bar mol)}^{-1}$			

Table 5.2 - 3: Initial model parameters and references.

Some geometry information about the initial poroelastic-elastoplastic model are given in Table 5.2 - 4.

Geometry	Top channel: 50 m; Bottom channel: 125 m; Width: 2 km	
Background stress field horizontal, vertical	horizontal = 0.5 x vertical load	
ice stress rate per year	17.3 Mpa	90000 years build-up & 5000 years melting

Table 5.2 - 4: Geometry information of initial model test.

After a software update to COMSOL Multiphysics 5.2a, the possibility arose to use poroelastoplasticity instead, resulting in a common physics domain for the entire model with locally varying parameters. An advantage of the new poro-elastoplastic model is the integrated treatment of the water flow. In the initial model, special attention had to be given to water flow at the intersection of poroelastic to elastoplastic domain, e.g. between sand-filled channels and elastoplastic host layer. The integrated porosity makes no-flow boundaries between channels and host layers obsolete. Model design and simulations were performed with the software modules: Geomechanics, Structural Mechanics and Subsurface Fluid Flow.

The poroelastoplastic performance of the new version was tested by recreating the simulation from Nikolinakou *et al.* (2012). After confirming similar simulation results, the 2D model for the Hugin Fracture case was designed based on an interpreted 3D seismic section. In addition, gravity and background stress field were not defined in the new model. A stress regime is implicitly included in the model as the boundaries define a top load ( $\sigma_1$ ) and horizontal movement in one direction ( $\sigma_3$ ). The third stress direction is normal to the model section.

### *Ice load*

We want to test ice-load induced differential compaction and to this end, we decide to include a top load following a ramp function. This allows us to control the amplitude, the steepness of the ice sheet and the amount of top load. A ramp function is somewhat simplified compared to real slope at glacier/ ice sheet fronts, that follow a root function (Boulton *et al.* 1999). (Grollmund and Zoback 2000) use a step function to model the stress field that is induced in the Earth's crust by a 2 km-thick Scandinavian ice sheet. A ramp function is somewhat closer to reality than a step function, and it helps to model the lateral increase in top load over the ice sheet front.

The top load was increased linearly over a time period of 10,000 years, a following decrease at the same rate and an eventual relaxation period of 5000 years. The 20,000 year cycle intends to follow the mean time for a glaciation cycle (Graham *et al.* 2013).

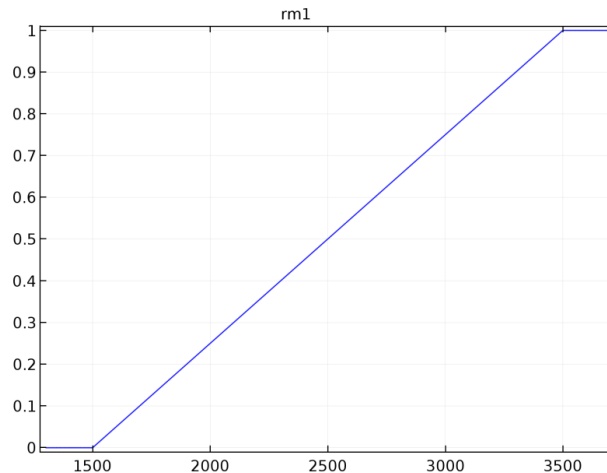


*Figure 5.2 - 1: Ramp function that is used for the ice sheet (top load) geometry and location above the upper boundary of the 2D model. The amount of maximum top load is scaled by the „load“ parameter.*

### *Hardening rule*

For the clay component and the clay rich layers we defined a hardening rule in the software, to account for the change from elastic to the plastic behaviour. Several clays have been studied in detail, e.g. the London clay (Gasparre 2005). We assumed an elastic – perfectly plastic behaviour of the water-filled clays. This may underestimate dilation, if the true behaviour is strain softening (densely packed grains). For a true strain hardening clay (loosely packed grains) this may overestimate dilation, as strain hardening is seen in material that is strengthened under shearing.

### *Depth-dependent cohesion*

Even for the unconsolidated sediments in the Pleistocene, cohesion is assumed to increase with depth due to the weight of the top sediments. To account for this

background increase in cohesion, a linear cohesion function is implemented in the model and applied to the background medium. The cohesion is assumed to increase by 7kPa/m.

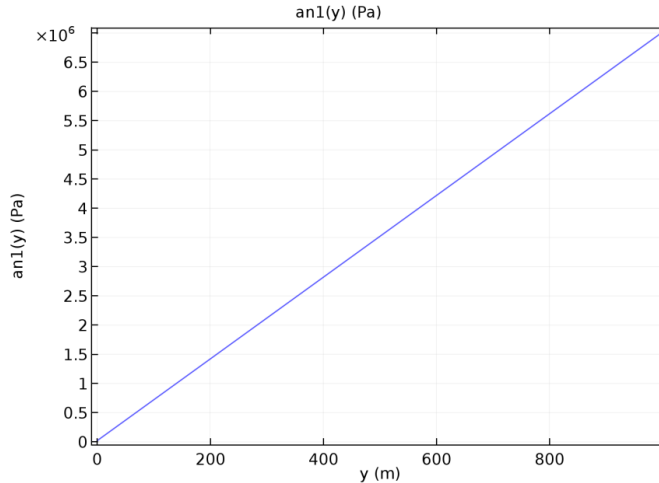


Figure 5.2 - 2: Linear cohesion-depth function.

### *Model boundaries*

The movement of sediment layers in response to a top load is assumed to be predominantly to the side, vertical movement is inhibited by the sediment in the subsurface. The lower boundary is set to rollers to enable lateral movement and inhibit vertical movement. The top of the model is a free boundary, where it is not subjected to the top load ramp function. This enables surface deformations to take place in front of the top load (ice sheet). The stresses induced by an ice sheet dissipate over distance in front and farther away from the ice sheet. In order to allow the same for the stresses in the model, an infinity-layer (free surface) was defined on one side of the model domain. On the opposite side, a symmetry boundary was chosen. This way, the model is virtually “doubled” without increase in computation time.

Fluid flow was permitted inside the model domain, permeabilities and compressibility of water are taken from literature (Table 5.2 - 3)

## Results

The simulations were stable for a maximum top load of 80 MPa, representing an ice sheet with approximately 80 m thickness. However, peak stress was reached at 10,400 years shortly after top load starts decreasing. This may indicate a change in plastic behaviour, indicating fracturing (which is not included or pre-defined in the model setup). Therefore, only results from this time step were used for paper III, as the remainder of the simulations has to be considered unreliable.

It is, however, interesting to look at the effective plastic strain display after the top load was lifted and the relaxation time was over.

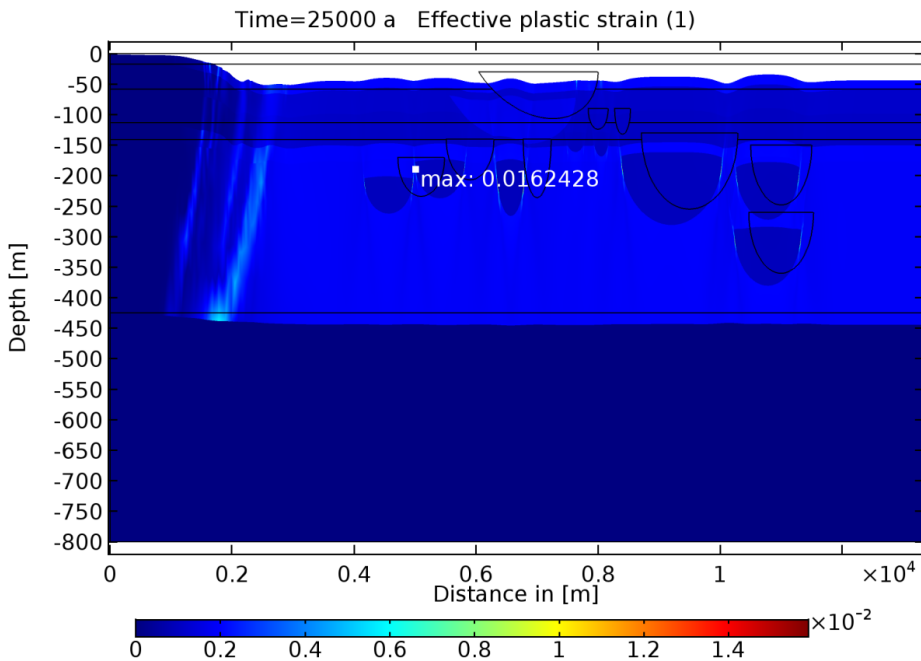


Figure 5.2 - 3: Effective plastic strain at the end of the simulation. Note the interesting topography (50 times exaggerated vertical displacement).

The display in Figure 5.2 - 3 shows an interesting topography (with 50 times exaggeration of the vertical displacement). Differential compaction lead to superimposed compaction ridges above all channels. In the flexure zone below the

ramp front of the ice sheet, surface deformation can be seen that resembles the cross section of a tunnel valley or till deposition (Al Hseinat and Hübscher 2014). Further investigation with a 3D model could illuminate and strengthen this interesting observation.

### References cited in the Appendix

Al Hseinat, M. and Hübscher, C. 2014. Ice-load induced tectonics controlled tunnel valley evolution - instances from the southwestern Baltic Sea. *Quaternary Science Reviews*, 97, 121–135.

Andreassen, K., Nilssen, E.G. and Ødegaard, C.M. 2007. Analysis of shallow gas and fluid migration within the Plio-Pleistocene sedimentary succession of the SW Barents Sea continental margin using 3D seismic data. *Geo-Marine Letters*, 27(2–4), 155–171.

Anell, I., Thybo, H. and Rasmussen, E. 2012. A synthesis of Cenozoic sedimentation in the North Sea. *Basin Research*, 24(2), 154–179.

Bjørlykke, K. 2015. Petroleum geoscience: From sedimentary environments to rock physics, second edition. *Petroleum Geoscience: From Sedimentary Environments to Rock Physics, Second Edition*, 1–662.

Bolton, A.J., Maltman, A.J. and Fisher, Q. 2000. Anisotropic permeability and bimodal pore-size distributions of fine-grained marine sediments. *Marine and Petroleum Geology*, 17(6), 657–672.

Boulton, G.S., Caban, P. and Hulton, N. 1999. *Simulations of the Scandinavian ice sheet and its subsurface conditions*.

Boulton, G.S. and Dobbie, K.E. 1993. Consolidation of sediments by glaciers: relations between sediment geotechnics, soft-bed glacier dynamics and subglacial ground-water flow. *Journal of Glaciology*, 39(131).

Fugro Survey AS 2012. *Site survey at planned well location 16/4-X final, LN11302, PL544*. Lysaker, Norway.

Gasparre, A. 2005. *Advanced Laboratory Characterization of London Clay*. Imperial College London.

Gibbard, P.L., Head, M.J. and Walker, M.J.C. 2010. Formal ratification of the Quaternary System/Period and the Pleistocene Series/Epoch with a base at 2.58 Ma. *Journal of Quaternary Science*, 25(2), 96–102.

Graham, A.G.C., Stoker, M.S., Lonergan, L., Bradwell, T. and Stewart, M.A. 2011. The Pleistocene Glaciations of the North Sea Basin. *IN: J. Ehlers and P. Gibbard (eds.) Quaternary Glaciations - Extent and Chronology*. pp. 261–278.

Graham, A.G.C., Stoker, M.S., Lonergan, L., Bradwell, T. and Stewart, M.A. 2013. The Pleistocene Glaciations of the North Sea basin. *Journal of Chemical Information and Modeling*, 53(9), 1689–1699.

Gregersen, U., Michelsen, O. and Sørensen, J.C.J. 1997. Stratigraphy and facies distribution of the Utsira Formation and the Pliocene sequences in the northern North Sea. *Marine and Petroleum Geology*, 14(7), 893–914.



- Grollimund, B. and Zoback, M.D. 2000. Post glacial lithospheric flexure and induced stresses and pore pressure changes in the northern North Sea. *Tectonophysi*, 327, 61–81.
- Grollimund, B., Zoback, M.D., Wiprut, D.J. and Arnesen, L. 2001. Stress orientation, pore pressure and least principal stress in the Norwegian sector of the North Sea. *Petroleum Geoscience*, 7(2), 173–180.
- Grollimund, B. and Zoback, M.D. 2003. Impact of glacially induced stress changes on fault-seal integrity offshore Norway. *AAPG Bulletin*, 87(3), 493–506.
- Hamilton, E.L. 1971. Elastic Properties of Marine Sediments. *Journal of Geophysical Research*, 76(2), 579–.
- Hampton, M.A. 2002. Gravitational failure of sea cliffs in weakly lithified sediment. *Environmental and Engineering Geoscience*, 8(3), 175–191.
- Harrington, J., Birchall, D., Noy, D., Cuss, R. and Graham, C. 2011. Consolidation and mass transport properties of the Nordland Shale. *IN: Geophysical Research Abstracts*. p. 12688.
- Ikari, M.J. and Kopf, A.J. 2011. Cohesive strength of clay-rich sediment. *Geophysical Research Letters*, 38(16), 1–5.
- Jordt, H., Faleide, J., Bjørlykke, K. and Ibrahim, M. 1995. Cenozoic sequence stratigraphy of the central and northern North Sea Basin: tectonic development, sediment distribution and provenance areas. *Marine and Petroleum Geology*, 12(8), 845–879.
- Kennett, C. 2008. *Evaluation of internal geometries within the Miocene Utsira Formation to establish the geological concept of observed CO<sub>2</sub> responses on 4D seismic in the Sleipner area, North Sea*. Imperial College London.
- Løseth, H., Raulline, B. and Nygard, A. 2013. Late Cenozoic geological evolution of the northern North Sea: development of a Miocene unconformity reshaped by large-scale Pleistocene sand intrusion. *Journal of the Geological Society*, 170(1), 133–145.
- Mondol, N.H., Bjørlykke, K., Jahren, J. and Høeg, K. 2007. Experimental mechanical compaction of clay mineral aggregates—Changes in physical properties of mudstones during burial. *Marine and Petroleum Geology*, 24(5), 289–311.
- Nicoll, G. 2012. *Evaluation of the Nordland Group overburden as an effective seal for the Sleipner CO<sub>2</sub> storage site (offshore Norway) using analytical and stochastic modelling techniques*. University of Edinburgh.
- Nikolinakou, M.A., Luo, G., Hudec, M.R. and Flemings, P.B. 2012. Geomechanical modeling of stresses adjacent to salt bodies: Part 2—Poroelestoplasticity and coupled overpressures. *AAPG Bulletin*, 96(1), 65–85.
- Ottesen, D., Dowdeswell, J.A. and Bugge, T. 2014. Morphology, sedimentary infill and depositional environments of the Early Quaternary North Sea Basin (56° to 62°N). *Marine and Petroleum Geology*, 56, 123–146.
- Pierrot, D. and Millero, F.J. 2000. The Apparent Molal Volume and Compressibility of Seawater Fit to the Pitzer Equations. *Journal of Solution Chemistry*, 29(8), 719–742.
- Pillitteri, A., Cerasi, P., Stavrum, J., Zweigel, P. and Bøe, R. 2003. *Rock mechanical tests of shale samples from the cap rock of the Utsira Sand in well 15/9-A11 - A contribution to the Saline Aquifer CO<sub>2</sub> Storage (SACS) project*. Trondheim, Norway.

Sejrup, H., Aarseth, I., Ellingsen, K.L., Reither, E., Jansen, E., Løvlie, R., Bent, A., Brigham-Grette, J., Larsen, E. and Stoker, M. 1987. Quaternary stratigraphy of the Fladen area, central North Sea: a multidisciplinary study. *Journal of Quaternary Science*, 2(1), 35–58.

Sejrup, H., Hafliðason, H. and Aarseth, I. 1994. Late Weichselian glaciation history of the northern North Sea. *Boreas*, 23(1991), 1–13.

Sejrup, H.P., Clark, C.D. and Hjelstuen, B.O. 2016. Rapid ice sheet retreat triggered by ice stream debuitressing: Evidence from the North Sea. *Geology*, 44(5), 355–358.

Sharqawy, M.H., Lienhard, J.H. and Zubair, S.M. 2010. Thermophysical properties of seawater: a review of existing correlations and data. *Desalination and Water Treatment*, 16(1–3), 354–380.

Storvoll, V., Bjørlykke, K., Karlsen, D. and Saigal, G. 2002. Porosity preservation in reservoir sandstones due to grain-coating illite: A study of the Jurassic Garn Formation from the Kristin and Lavrans fields, offshore Mid-Norway. *Marine and Petroleum Geology*, 19(6), 767–781.

Wood, D.M. 1990. *Soil behaviour and critical states soil mechanics*. Cambridge University Press, United Kingdom and New York.

## Errata


**Errata for  
Geophysical investigation of the Hugin Fracture, a  
soft sediment seefloor fracture on the Utsira High,  
North Sea**

*Implications for subsurface fluid migration*

**Karin Landschulze**



Thesis for the degree philosophiae doctor (PhD)  
at the University of Bergen

15.05.2019   
(date and sign. of candidate)

  
(date and sign. of faculty)



Page numbers are updated according to inserted blank pages before pages ii, iii, 14, 30, 175.

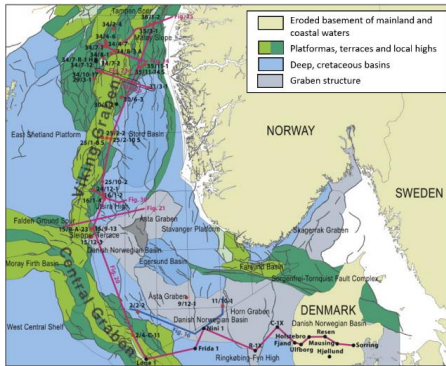
Page iv Missing comma: “Centres of Excellence (CoE) between” – corrected to “Centres of Excellence (CoE), between”

Page viii Misspelling: “highly-industrialized” – corrected to “highly industrialised”, and: “sea-floor” – corrected to “seafloor”

Page ix Misspelling: “stiff-clay” – corrected to “stiff clay”, and: “A fracture and associated surface deformation develops” – corrected to “A fracture and associated surface deformation develop”

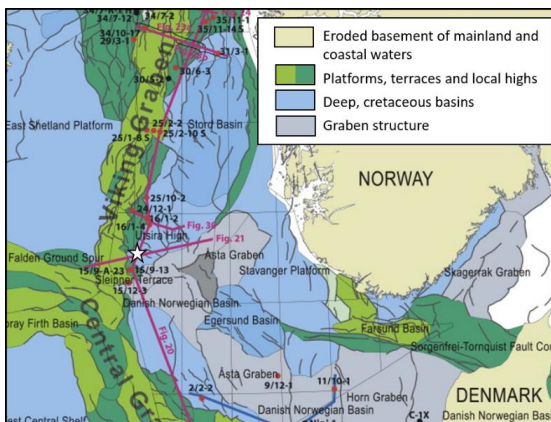
## Introduction

Page 14 Added location of study area in Figure 1 and updated figure caption:



“Structural map of North Sea Basin (figure 15 from Eidvin et al. 2014, figure references refer to figures in their work).”

– corrected to



“Structural map of North Sea Basin (changed from Figure 15 from Eidvin et al. 2014, figure references refer to figures in their work). White star indicates location of the Hugin Fracture study area.”

Page 14 Figure 1 updated for location of the study area, both figure and caption.

Page 19 Misspelling: “waste water” – corrected to “wastewater”

## Paper I

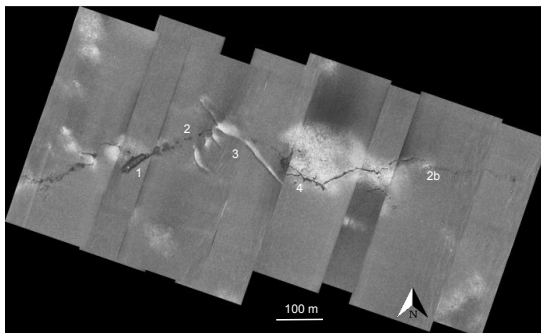
Throughout the manuscript of Paper I Abbreviation: “Fig.” – corrected to “Figure”

Figure numbering: Figures “4” through “11” – corrected to figures “3” through “10”

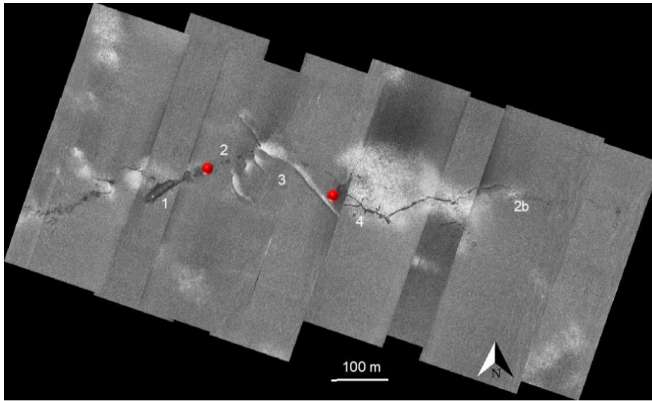
Page 3 Misspelling in figure caption: “...*the location of the study area (red square). [...] Coloured squares [...] Areas shade in yellow*” – corrected to “*the location of the study area (black square). [...] Small white rectangles [...] Areas shaded in yellow*”

Page 7 Missing references: “(xxx)” – corrected to “Gracias *et al.*, 2013; Shihavuddin *et al.*, 2013”

Page 10 Added push core locations on figure 3 and updated figure caption accordingly:



– corrected to



Page 10 Misspelling caption figure 10: “sampled from areas 1 and 4” – corrected to “sampled from areas 2 and 4 (red dots)”

Page 12 Missing figure reference: “structure (Figure 4)” – corrected to “structure (Figures 3, 5A and 5B)”

Page 13 Figure references: “Figure 3A” – corrected to “Figure 3”

Page 17 Updated figure caption to Figure 9: “A) The shape” – corrected to “A) A time slice from the 3D seismic amplitude cube showing the shape”

Page 17 Wording: “are a number of other” – corrected to “numerous”

Page 26 Missing reference: added “Gracias, N., P. Ridao, R. Garcia, J. Escartin, M. L’Hour, F. Cibecchini, R. Campos, M. Carreras, D. Ribas, N. Palomeras, L. Magi, A. Palomer, T. Nicosevici, R. Prados, R. Hegedus, L. Neumann, F. de Filippo and A. Mallios (2013). Mapping the Moon: Using a lightweight AUV to survey the site of the 17th Century ship ‘La Lune’. *Proc. of the Oceans MTS/IEEE OCEANS conference*, Bergen, Norway, June 2013”

Page 28 Missing reference: added “Munz, I., Johansen, H., Huseby, O. Rein, E., Scheire, O. (2010). Water flooding of the Oseberg Øst oil field, Norwegian North Sea: Application of formation water chemistry and isotopic composition for production monitoring. *Marine and Petroleum Geology*, 27, 838-852.”

Page 29 Missing reference: added “Shihavuddin, A., N. Gracias, R. Garcia, J. Escartin and R. Pedersen (2013). Automated classification and thematic mapping of bacterial mats in the North Sea, *Proceedings of the Oceans MTS/IEEE OCEANS conference*, Bergen, Norway, June 2013.”

## Paper II

Page 1 Misspellings: “highly-industrialized” and “sea-floor” – corrected to “highly industrialized” and “seafloor”

Page 12 Comma: “converge and” – corrected to “converge, and”

Page 15 Misspelling: “high resolution” – corrected to “high-resolution”,

Page 15 Wording: “there currently is” – corrected to “there is currently”

Page 43 Misspelling: “low-frequency” – corrected to “low frequency”

### **Synthesis**

Page 176 Misspelling: “of several kilometres length” – corrected to “of several kilometres’ length”

Page 185 Misspelling: “waste water” – corrected to “wastewater”

### **Appendix**

Page III Misspelling: “small scale” – corrected to “small-scale”



Graphic design: Communication Division, UIB / Print: Skjipes Kommunikasjon AS



[uib.no](http://uib.no)

ISBN: 9788230843017 (print)  
9788230850053 (PDF)